How circumstellar discs affect mass accretion in Be X-ray binaries

Itumeleng Matuba Monageng

November 2013

A dissertation submitted in partial fulfilment of the requirements for the degree M.Sc. in the Department of Astronomy, as part of the National Astrophysics and Space Science Programme

UNIVERSITY OF CAPE TOWN

Supervisor: Dr. Vanessa McBride

Abstract

Long-term optical spectroscopic monitoring of Galactic Be X-ray binaries (BeXBs) is performed using the Liverpool Telescope and the Southern African Large Telescope on northern and southern objects, respectively. Be disc size variations are presented to investigate their influence on mass accretion producing X-ray activity. Be disc variability is traced observationally through Balmer emission lines, the strongest and best studied being the H_α line. The peak separations of the double peaked H_α emission line are measured, and along with the mass of the Be star and the inclination of the disc obtained from literature, are used to determine the Be disc radius. For single peaked H_α profiles the peak separation cannot be obtained directly; however, using the empirically determined relationship between the equivalent width and the peak separation of the double peaked profiles, an estimate of the peak separation for the single peaked profiles is obtained. The work is done in the context of the viscous decretion disc model presented by Okazaki & Negueruela (2001), which predicts that the circumstellar discs around Be stars in binary systems are truncated by resonant torques from the neutron star in its orbit. The calculated disc radii are compared to the expected resonance radii from the viscous decretion disc model to determine how different truncation radii affect mass accretion producing X-ray outbursts.

Type I outbursts are seen to occur when the disc is truncated close to/beyond the mean critical Roche lobe radius at periastron passage of the neutron star, in agreement with model predictions. Type II outbursts, however, do not show any correlation (or anti-correlation) with the disc size, as they are seen to occur both at relatively small and large sizes of the disc. Additional information on the H_α emission line profile variations, such as the line-shape variations of high-resolution spectra, is required to investigate the origin of type II outbursts in order to make reliable predictions of them.

Spectroscopic follow-up of the gamma-ray binary system LSI +61 303 was also performed with the Liverpool Telescope and the H_α line profile variations are presented. In

addition to data from the Liverpool Telescope monitoring campaign, published equivalent width measurements are used and timing analysis of the combined measurements is performed. The orbital period and super-orbital period are found, which are similar to those found at other wavelengths. The periodicities in the system can therefore be associated with circumstellar disc variations.

Acknowledgements

Thank you to the South African Square Kilometer Array project for their financial support.
Thank you to the organisers of the NASSP programme for giving me an opportunity to pursue my dream career.
Thank you to South African Astronomical Observatory (SAAO) and the University of Cape Town Astronomy Department for providing me with office space and making it a pleasurable environment to work in. Thank you to the SAAO IT team and Bianca Keane for installing a number of software on my computer that were critical for this research project.
Thank you to the stellar astrophysics group (BANG!) group at SAAO for the support they provided and the group discussions, a number of which were related to the work presented in this thesis.
My friends and former NASSP classmates have encouraged me and provided great memories throughout my academic career. I am thankful to my family for believing in me and the support they have provided.
Finally, I would like to express my sincere gratitude to my supervisor, Dr. Vanessa McBride, for the assistance provided, as well as her patience, encouragement and very quick response to all the questions brought up.

Plagiarism Declaration

I, Itumeleng Monageng, know the meaning of plagiarism and declare that all of the work in the document, save for that which is properly acknowledged, is my own.

Contents

1 Introduction and background **1**

1.1 Optical properties 5

1.1.1 H_α V/R variability 7

1.1.2 Infrared excess 8

1.2 Circumstellar disc formation 11

1.3 X-ray properties 13

1.3.1 Type I outbursts 16

1.3.2 Type II outbursts 16

1.4 Viscous decretion disc model 16

1.4.1 X-ray outbursts in the framework of the viscous decretion disc model 18

2 LS I +61 303 **21**

2.1 Introduction 21

2.2 Microquasar model 22

2.3 Pulsar wind model 25

2.4 Four year superorbital modulation 29

2.4.1 Radio bands 29

2.4.2 Optical spectroscopy (H_α) 31

2.4.3 X-rays 32

3 Instruments and Observations **35**

3.1 The Southern African Large Telescope 35

3.1.1 Observations 38

3.2 The Liverpool Telescope 40

3.2.1 FRODOSpec 42

3.3 Archival Spectra 47

4 Results, Analysis and Discussion I: Galactic BeXBs **49**
4.1 Method of radius calculation 49
4.2 Galactic BeXBs 57
4.2.1 A0535+262 57
4.2.2 4U0115+634 64
4.2.3 V0332+53 69
4.2.4 EXO2030+375 74
4.2.5 A1118-617 77

5 Results, Analysis and Discussion II: LS I +61 303 **79**
5.1 Timing analysis 83

6 Conclusions **85**
6.1 Galactic BeXBs 85
6.1.1 A 0535+262 85
6.1.2 4U 0115 +63 85
6.1.3 V 0332+53 86
6.1.4 EXO 2030+375 86
6.1.5 A 1118-67 86
6.2 LS I +61 303 87
6.3 Future Prospects 88

A Data **91**

B H_α line profiles **107**
B.1 A selection of H_α line profiles obtained with the Liverpool Telescope and SALT. 107
B.1.1 A 0535+262 107
B.1.2 4U 0115+63 108
B.1.3 V 0332+53 109
B.1.4 EXO 2030+375 109
B.1.5 A 1118-617 110

Chapter 1

Introduction and background

X-ray binary stars are multiple stellar systems consisting of a normal star* (the "optical" component) and a compact object (e.g. neutron star, black hole or white dwarf) in orbit around a common centre of mass. The optical companion loses matter to the compact companion resulting in X-ray outbursts, hence the optical companion and the compact object are sometimes termed donor and accretor, respectively. X-ray binaries are divided into high mass X-ray binaries (HMXBs) and low mass X-ray binaries (LMXBs), depending on the spectral type of the donor. Systems which contain a donor of spectral type O or B belong to the HMXB subclass, while LMXBs contain donors of spectral type later than A (Waters & van Kerkwijk 1989, Reig 2011, Paul & Naik 2011). The X-ray emission from HMXBs is harder than that from LMXBs (Reig 2011). Accretion of material onto the compact object occurs via Roche-lobe overflow in the case of LMXBs. In this scenario the donor fills its Roche-lobe and material can overcome the gravitational pull of the donor star, where it flows through the inner Lagrangian point (L_1 point) and is accreted by the compact object giving rise to an enhanced X-ray emission. In HMXBs, in addition to Roche-lobe overflow, accretion can take place via stellar winds from the donor which are captured by the compact object, as well as through circumstellar disc accretion in systems where the accretor passes through the disc at close approach resulting in transient X-ray outbursts (Waters & van Kerkwijk 1989, Hellier 2001).
HMXBs are further divided into two subclasses depending on the luminosity class of the donor: Super-giant X-ray binaries (SGXBs) and Be X-ray binaries (BeXBs). Systems which contain a donor star of luminosity class I or II fall under the subclass SGXBs

*Hydrogen core burning is still taking place.

while those which contain a donor of luminosity class III, IV or V and which are classical Be/Oe stars are classed BeXBs (Waters & van Kerkwijk 1989, Reig 2011). The compact accretors in HMXBs can be black holes or neutron stars. The majority of HMXBs are neutron star accretors and the X-ray emission is pulsed due to the misalignment of the magnetic axis of the neutron star with its spin axis (see section 1.3). The pulse periods of the neutron stars can range from a few seconds (P_{spin} ∼3.6 sec, 4U 0115+63; Tamura et al. 1992) to a few minutes (P_{spin} ∼1404 sec, LS I +61 235; Reig et al. 2000). The different classes and subclasses of X-ray binaries are illustrated in Fig. 1.1.

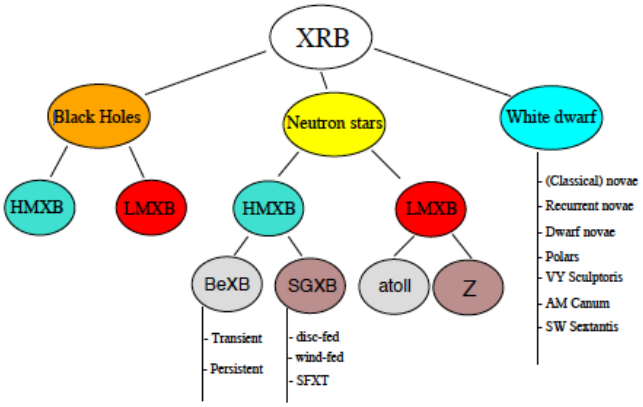

Figure 1.1: Tree structure showing the family of X-ray binaries. Credit: Reig (2011).

Fig. 1.2 shows the distribution of HMXBs in the P_{spin} vs. P_{orb} diagram (Corbet's diagram). As can be seen in the figure the accretion disc-fed SGXBs display an anticorrelation, while the wind-fed SGXBs show no correlation or anticorrelation, as they have a flat distribution. The BeXBs, which are the subject of this thesis, show a positive correlation between P_{spin} and P_{orb}. The correlation of P_{spin} with P_{orb} in BeXBs was first presented by Corbet (1984). The relationship is explained by the interaction of the material from the disc with the neutron star magnetospheric radius (the radius at which the magnetic field pressure and the ram pressure of the material falling in are equal). Accretion onto the NS will occur when the magnetospheric radius is smaller than the corotation radius (the radius at which material corotates with the NS at the Keplerian velocity). When the magnetospheric radius is larger than the corotation radius, matter will be expelled in a propeller effect. During accretion of material the NS is spun-up since angular momentum is added, while the spin-down of the NS occurs when matter is propelled (since angular momentum is lost). The NS in BeXBs spins close to equilibrium period (i.e. it spins with the period at which the magnetospheric radius and the

corotation radius are equal). The equilibrium period is a function of the mass flux (the larger the mass flux the smaller the period) since the extent of the magnetosphere is dependent on the accretion rate, with the relationship $P_{eq} \propto B^{6/7} M_X^{-5/7} \dot{M}^{-3/7}$ (where B, M_X and $\dot{M}$ are the NS magnetic field strength, NS mass and the mass accretion rate, respectively; Waters 1989). The mass flux in turn depends on how wide the orbit is (or the orbital period, P_{orb}): the wider the orbit (the larger the P_{orb}) the smaller the mass flux. It follows that the spin period of the NS is directly proportional to P_{orb}. However, the equilibrium period can change at a specific epoch depending on the size of the magnetospheric radius relative to the corotation radius. During accretion the corotation radius is larger than the magnetospheric radius, resulting in a decrease in the spin period (i.e. the rate of change of the spin period is negative, $\dot{P}_{spin} < 0$). When the corotation radius is smaller than the magnetospheric radius, matter is propelled out, resulting in an increase in the spin period ($\dot{P}_{spin} > 0$) (Corbet 1984; 1986, Stella et al. 1986, Waters & van Kerkwijk 1989).

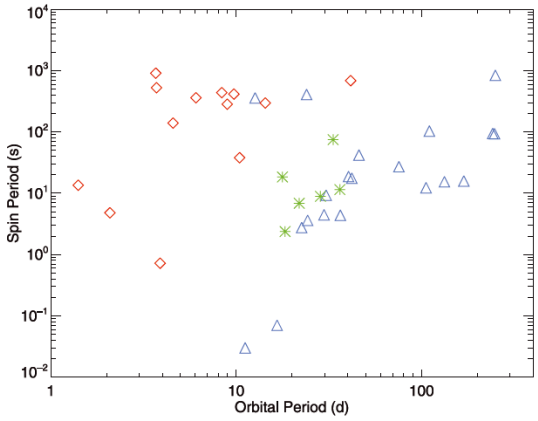

Figure 1.2: P_{spin} - P_{orbit} diagram for massive X-ray binaries. The red diamonds represent supergiant systems (the three points at the bottom left-hand side are disc-fed supergiant systems), green stars represent BeXBs in the Small Megalanic Cloud (SMC) and the triangles represent BeXBs in the galaxy. Credit: Townsend et al. (2011).

BeXBs make up a large majority of the HMXB subclass (about 2/3 of the identified systems, Paul & Naik 2011). All confirmed BeXBs have NS accretors. The lack of black holes (BH) accretors in BeXBs is puzzling since there is no mechanism that forbids such systems from forming. Sadowski et al. (2008), based on population synthesis models, proposed that the lack of Be black hole (BeBH) systems is due to the distribution of

orbital periods. The results reveal that BeBH systems are formed with relatively long orbital periods (peak probability density at $\sim 10^4 - 10^6$ days), much longer than the orbital period range in which BeXBs are found ($\sim 10 - 300$ days). This, combined with low intensity X-ray emission (inefficient accretion at the very wide orbits) would make it difficult to detect BeBH systems. It was noticed, however, that the results from the work were incorrect, as there were errors in the population synthesis result analysis (Belczynski & Ziolkowski 2009). Belczynski & Ziolkowski (2009) used a revised code of the population synthesis model to predict a ratio of NS binaries to BH binaries of $\sim 30 - 50$, consistent with observational data of 42 Galactic NS BeXBs which corresponds to $0 - 2$ BeBH systems. The authors conclude that BeBHs exist but due to the expected small number of them they haven't yet been detected*.

Fig. 1.3 illustrates the geometry of a typical BeXB system with a NS in an eccentric orbit (in general $e \gtrsim 0.3$) around an Oe/Be star with a circumstellar disc around the equator.

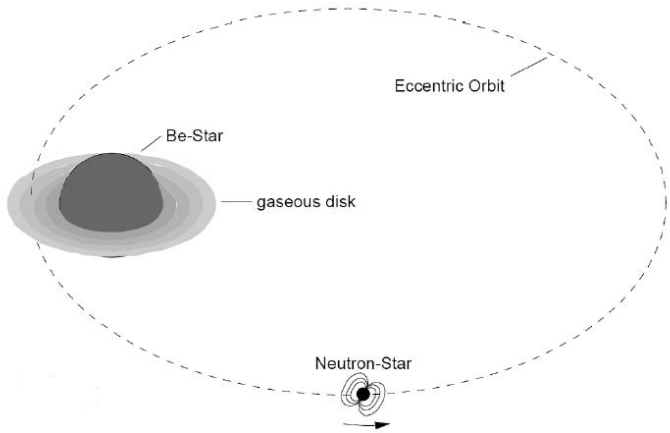

Figure 1.3: Schematic of a typical BeXB system. The neutron star is in an eccentric orbit around the Be star with a circumstellar disc around its equatorial region. Material in the circumstellar disc may be accreted by the neutron star as it undergoes periastron passage. Credit: Kretschmar (1996).

In this thesis I analyse long term optical spectroscopic data of Galactic BeXBs with X-ray lightcurves to investigate the role of the circumstellar disc in the accretion process in the context of the viscous decretion disc model. The data were obtained from op-

*The first BeBH system was confirmed by Casares et al. (2014).

tical spectroscopic monitoring programmes with the Southern African Large Telescope (SALT), for southern objects, and the Liverpool Telescope (LT) for northern objects and are supplemented with archival data (*Programme 1*). I also present optical spectroscopic analysis of the gamma-ray binary system, LS I +61 303, combining published data with data obtained with the LT. In chapter 3 I give an overview of the two telescopes used to obtain the data, as well as the instrument settings and a brief description of the data reduction process. A discussion of the results for the analysis of Galactic BeXBs and LS I +61 303 is given in chapter 4 and 5, respectively. In chapter 6, conclusions of the results are presented and future projects are briefly described. First, the necessary background of BeXBs is given with the main properties of the systems described.

1.1 Optical properties

In BeXBs, the optical light comes primarily from the donor. Long-term optical surveys are important in the study of BeXBs, as they provide information on the matter in the neighbourhood of the Be star, which ultimately is responsible for X-ray activity taking place in these systems. The optical spectra of Be stars are characterised by emission lines, and these stars were given the definition (Collins 1987): non-supergiant B stars whose spectra have, or had at some stage, one or more Balmer lines in emission. The emission lines from Be stars come from the matter which makes up the circumstellar envelopes surrounding the donor. The most common emission lines in the optical spectra of Be stars are those of HI, HeI, FeII, SiII and MgII (Porter & Rivinius 2003). The strength and/or morphology of these emission lines typically varies. The strongest of these lines, the H_α emission line, is the best studied line in Be stars. Dachs et al. (1986) studied the geometry of circumstellar discs in the analysis of relationships between different features of the H_α emission line. It was found from the study that the EW(H_α) is correlated to the circumstellar disc size from estimates obtained using different models (e.g. Gehrz et al. 1974, Kogure 1975, Jones 1979). The Be disc radius has also been measured directly from observations using optical interferometry and spectropolarimetry (Quirrenbach et al. 1997, Tycner et al. 2005, Gies et al. 2007). Thus the H_α emission line can be used as a gauge of the state of the circumstellar disc. H_α emission lines in Be stars are typically double-peaked, as the velocity distribution of the disc is Keplerian (Porter 1998). A typical double-peaked H_α emission line profile has three main features: a central depression and two peaks on either side of the depression. The peak to the

left side of the central depression is termed the "blue/violet" peak (V), and that on the right side of it is called the "red" peak (R). The emission lines, however, can have a variety of shapes: wine-bottle profiles, shell profiles and single-peak profiles (Hummel & Vrancken 1995a;b, Porter & Rivinius 2003, Silaj et al. 2010). The emission line profiles have been observed to have symmetric and asymmetric shapes. Two morphological classes are given to the emission lines (Hanuschik et al. 1988, Hanuschik 1988, Hummel & Vrancken 1995a;b, Silaj et al. 2010):

- class I - symmetric profiles
- class II - asymmetric profiles

The asymmetric profiles are explained to be the result of one-armed density waves in the circumstellar disc (see section 2.1) (Hummel & Hanuschik 1997, Hummel & Vrancken 1997). Applying a three-dimensional radiative transfer code to inhomogeneous Be star circumstellar envelopes, Hummel (1994) demonstrated that the symmetric H_α emission profiles result from simple Keplerian discs. Examples of the different classes of the H_α emission line profiles are illustrated in Figs. 1.4, 1.5 and 1.6.

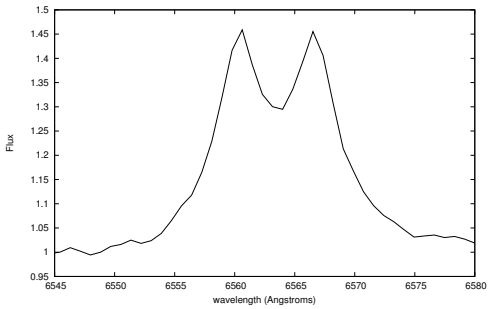

(a) A 0535+262 (Isaac Newton Telescope)

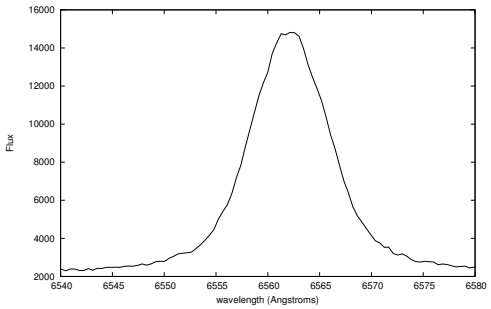

(b) A 1118-67 (South African Astronomical Observatory 1.9-m telescope)

Figure 1.4: Examples of class I profiles of the H_α emission line of Be stars.

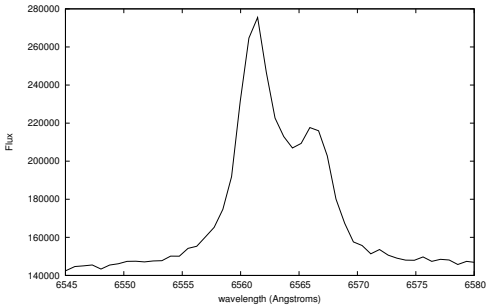

(a) A 0535+262 (Isaac Newton Telescope)

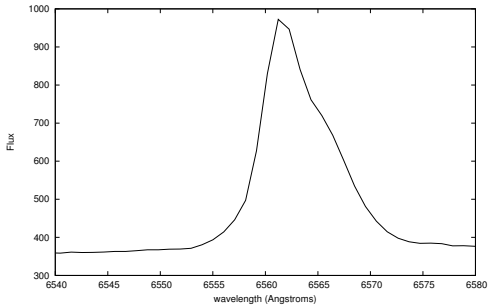

(b) A 0535+262 (Jacobus Kapteyn Telescope)

Figure 1.5: Examples of class II profiles of the H_α emission line of Be stars.

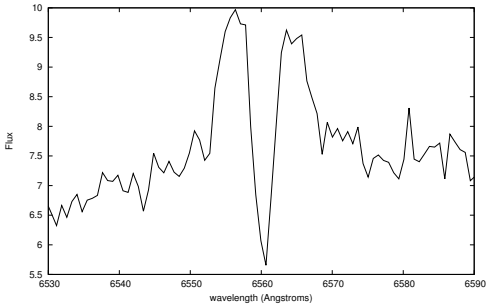

(a) 4U 0115+63 (Isaac Newton Telescope)

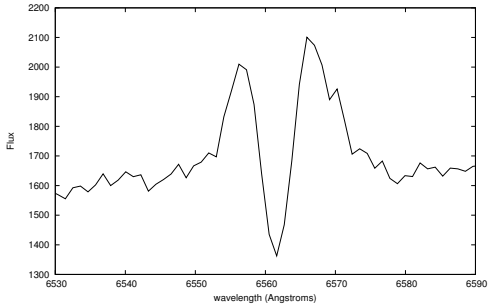

(b) 4U 2206+53 (Isaac Newton Telescope)

Figure 1.6: Examples of shell profiles of the H_α emission line of Be stars.

1.1.1 H_α V/R variability

A majority of Be stars have class II emission lines and are variable on a timescale of years (Hummel & Hanuschik 1997). The intensity of the red peak has been seen to vary relative to the intensity of the blue peak, and this process of variability in the peak intensity is termed the V/R variability. The values of 'V' and 'R' are the flux values of the violet and red peaks, respectively, relative to the continuum. The ratio is often taken as a logarithm (i.e $\log(V/R)$), thus if $\log(V/R) > 0$ then the emission line profile is dominated by the blue peak and if $\log(V/R) < 0$ then the emission line is dominated by the red peak. Okazaki (1991) proposed that the V/R variation is the result of the precession of one-armed density waves in the opposite direction to the Keplerian rotation of the disc. This means that there is an enhanced density region (which causes an enhancement in the emission line intensity) which precesses. The model was extended by Papaloizou et al. (1992), who included the quadrupole contribution to the external

potential of a rotationally distorted Be star. The modification of the model was able to naturally explain the long-term cyclic behaviour of the V/R ratio. Hydrodynamical numerical calculations were performed by Savonije & Heemskerk (1993) to further support the model presented by Papaloizou et al. (1992). These models predict that the direction of precession of the density enhancement is prograde and not retrograde as suggested by earlier models. Telting et al. (1994) analysed spectra of the Be star β Mon and demonstrated from an observational viewpoint that the density enhancement precession is indeed prograde. The sequence for the V/R variation, as explained by Telting et al. (1994), is (Fig. 1.7):

I. $V > R$, when the enhanced density region moves towards our line of sight.

II. $V = R$, when the enhanced density region is in front of the star (shell profile).

III. $V < R$, when the enhanced density region moves away from our line of sight.

IV. $V = R$, when the enhanced density region is behind the star.

Photometric variability of Be stars has also been studied (e.g. Bird et al. 2012). Long-term optical light curves from databases obtained with projects such as the Optical Gravitational Lensing Experiment (OGLE II and OGLE III) and the MAssive Compact Halo Objects (MACHO) project have been used to derive orbital and superorbital periods for SMC BeXB systems (Mennickent et al. 2002, Rajoelimanana et al. 2011, Bird et al. 2012). Due to their similar periods, it has been suggested that the V/R variability and long-term variations (superorbital) in the optical light curves are related (Rajoelimanana et al. 2011). Photometric variability (particularly I-band variability, as the circumstellar disc emission is expected to emit a large fraction of the flux in this band; Bird et al. 2012) is a useful additional tool to X-ray variability (see section 1.3) which can be utilised to derive orbital periods of BeXBs.

1.1.2 Infrared excess

Another observational signature of Be stars is the infrared (IR) excess from the circumstellar envelope. Electron-proton scattering in the circumstellar disc produces free-free radiation from ionised gas, which results in the IR excess observed (Woolf et al. 1970, Gehrz et al. 1974). Using data from a sample of Be stars, it has been demonstrated that there exist correlations between IR colors and the $EW(H_\alpha)$. Neto & de Freitas-Pacheco

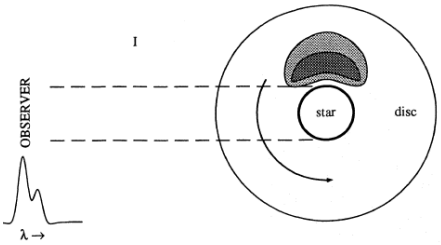

(a) the enhanced density region moves towards our line of sight, $V > R$

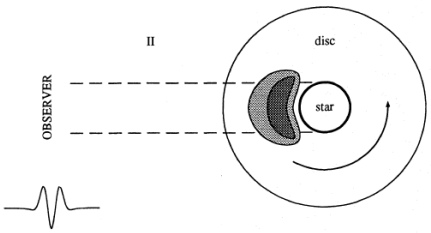

(b) the enhanced density region is in front of the star resulting in a shell profile, $V = R$

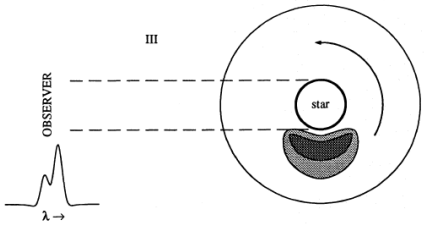

(c) the enhanced density region moves away from our line of sight, $V < R$

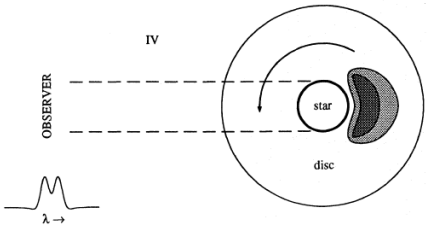

(d) the enhanced density region is behind the star, $V = R$

Figure 1.7: Schematic model of the H_α V/R variation of the Be star β Mon illustrating the prograde revolution of the enhanced density region around the circumstellar disc. Credit: Telting et al. (1994)

(1982) demonstrated this relationship in a plot of the continuum flux at 3.4 μm as a function of the $EW(H_\alpha)$. Similar studies, using the (J - M) colour index as a measure of the IR excess, have been done to demonstrate correlations with the $EW(H_\alpha)$ (Dachs & Wamsteker 1982, Dachs et al. 1988). The implication of the relationship between the two quantities is that they originate from the same region (i.e the circumstellar disc) and are due to the same processes: free-free and free-bound radiation from the circumstellar disc. Coe et al. (2005) demonstrated that the correlation exists for BeXBs in their analysis of a sample of sources in the SMC. This was done using the intrinsic IR colour $(J - K)_0$ plotted as a function of the $EW(H_\alpha)$ (Fig. 1.8, combined with data from isolated Be stars). The relationship can be used to estimate the excess reddening from the circumstellar disc, as one needs only the $EW(H_\alpha)$, a parameter easily obtained from spectroscopy, to obtain a corresponding value of $(J - K)_0$. The index $(J - K)_0$ of the star (based on the spectral type) can then be compared to this value from the $EW(H_\alpha)$ - $(J - K)_0$ correlation, and the extra contribution from the disc can then be estimated (Coe

et al. 2005).

Using *CHARA* interferometer array observations of a sample of Be star discs in the $K^{'}$ band, it was demonstrated by Gies et al. (2007) that the angular diameters of the Be discs in the $K^{'}$ band are consistently smaller than the angular diameters of the H_{α} emission from long baseline interferometric observations. It was proposed that this difference in the extent of the IR and the H_{α} emission in the disc is due to the larger H_{α} opacity, as well as a large fraction of neutral hydrogen as one moves further out in disc radius. It was also demonstrated that the H_{α} optical depth has a slower exponential decline with radius than that of the IR emission, which would result in the H_{α} emission having a larger spatial extension.

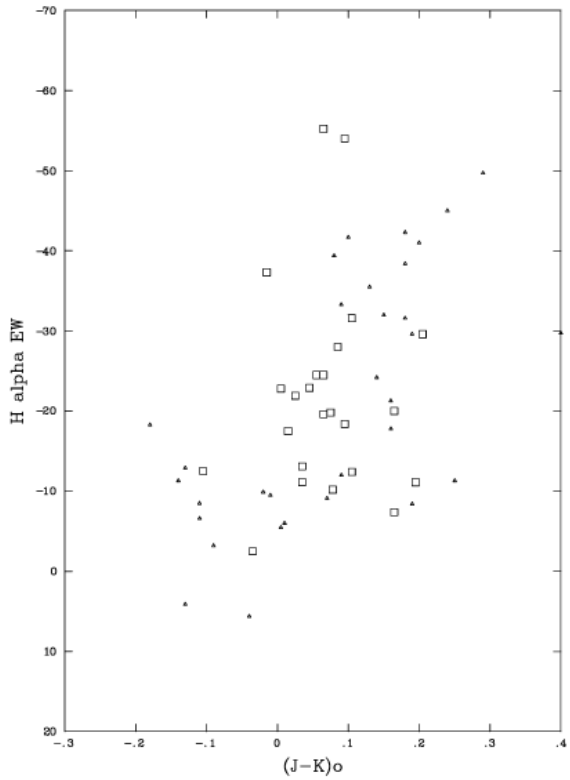

Figure 1.8: An illustration of the correlation between the Hα equivalent width and the IR colour (J - K)$_0$. The square symbols represent X-ray binaries in the SMC and the triangles represent isolated Be stars in the Milky Way. Credit: Coe et al. (2005).

1.2 Circumstellar disc formation

There have been a number of models proposed as to how the circumstellar disc surrounding the Be star forms. The fast rotation speed of Be stars is a very important factor in the disc-formation process. Townsend et al. (2004) demonstrated that Be stars rotate at near critical speeds (the rotation speed of the star at which the centrifugal force balances the gravitational force at the equator; once the star exceeds this speed material is lost at the equatorial regions), at $v_e \approx 0.95 v_c$. This result was obtained by taking the effect of equatorial gravity darkening*, into consideration, producing a higher value of the equatorial rotation speed than that previously reported at $v_e \approx 0.5 v_c - 0.8 v_c$ (Slettebak 1982, Porter 1996, Chauville et al. 2001, Yudin 2001). In a statistical study of rotation rates of Be stars, Cranmer (2005) used Monte Carlo modeling, taking into account gravity darkening to demonstrate that early-type Be stars (O7e - B2e) rotate at lower speeds with a range $0.4 v_{crit}$ - $0.6 v_{crit}$ while late-type (B3e - A0e) Be stars rotate closer to critical speeds.

An early model proposed to explain the disc formation process is the wind-compressed disc model (WCD, Bjorkman & Cassinelli (1993)). The model explains that a supersonic wind from the fast-rotating Be star travels along streamlines, and the complimentary streamlines from each hemisphere meet at the equator to form shocks. The process depends largely on the rotation speed of the star: for B2 stars disc formation occurs for $v_{rot} \geq 0.5 v_{crit}$, while for early O stars disc formation occurs for $v_{rot} \geq 0.9 v_{crit}$. The dense equatorial disc is then formed when the equatorial material is compressed by the wind ram-pressure (Fig. 1.9).

A challenge to the WCD model was presented by Owocki et al. (1996) when they took into consideration the nonradial line forces in the formation of the WCD. It was shown, using radiation-hydrodynamical simulations, that the nonradial forces suppress the equatorward flow required to form a WCD and slow down the wind rotation (the specific angular momentum of the equatorial wind outflow is decreased by about 20%), therefore decreasing the chances of a disc forming. Porter (1997) explored the viability of the WCD model further, by studying the IR emission produced from Be star discs. In his work, Porter (1997) calculated the IR emission of the discs formed by the WCD model and compared it to the IR emission from observations of the Be stars, and demonstrated

*The effect, in rotating stars, which causes the poles to appear brighter than the equatorial regions as a result of stellar surface energy flux variations caused by local effective gravity variations (Espinosa Lara & Rieutord 2012).

that the WCD model fails to produce the IR emission obtained from observations.

Cassinelli et al. (2002) developed the magnetically torqued disc (MTD) model to ex-

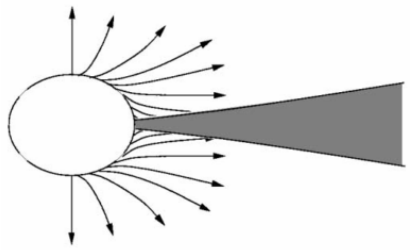

Figure 1.9: An illustration of the WCD model. The arrows represent wind streamlines ejected from the stellar photosphere from opposite hemispheres to meet at the equatorial plane, resulting in a shock. Credit: Porter & Rivinius (2003).

plain the formation of the circumstellar disc. The MTD model is a modification of the WCD model, where now the effects of magnetic torquing are taken into consideration. In the MTD model, the magnetic fields transfer angular momentum to the matter from the Be star, which is then channeled to the equatorial plane, leading to a shock-compressed disc (Fig. 1.10). In their work, Cassinelli et al. (2002) also investigated the magnetic field strengths required for MTDs to form. The field strengths required to produce MTD discs for early-type O stars were found to be unreasonably large ($> 10^3$ Gauss), whereas for early-type B stars the model provides more acceptable results, with magnetic field strengths of about 300 Gauss.

The viability of the MTD model was tested when Owocki & Ud-Doula (2003) performed MHD simulations to study the role of a dipole magnetic field in the formation of the disk. In their work, Owocki & Ud-Doula (2003) performed the simulations by investigating the effects of stellar rotation and the magnetic field strength characterised by the magnetospheric radius (Alfven radius, R_A) and the Keplerian radius (corotation radius), R_K, respectively. The results of the simulations show that in the case of weak fields, where $R_A < R_K$, the material from the star which is channeled by the magnetic field eventually falls back in onto the star. For intermediate strengths of the magnetic field, where $R_K < R_A < R_E$ (with R_E representing the escape radius* of the star), there is combination of effects, with material falling back in onto the star and some of it flowing out. In the case of strong fields ($R_A > R_E$) the material breaks out episodically. These results thus put question marks over the possibility of forming a stable equatorial disc

*the radius at which the local escape speed from the star's gravitational field is achieved.

as explained by the MTD model.

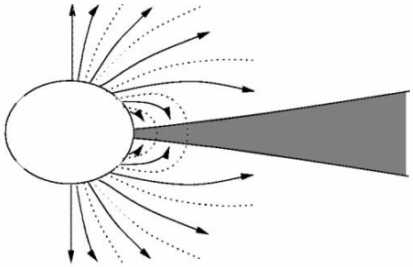

Figure 1.10: An illustration of the MTD model. The arrows represent wind streamlines channeled by the magnetic field lines (dotted lines). Magnetic field lines from opposite sides of the stellar hemisphere form closed loops at the equatorial regions, where material meets to form shocks resulting in the formation of a disc. Credit: Porter & Rivinius (2003).

Another model proposed to explain the disc-formation process is that which considers nonradial pulsations (NRPs) of Be stars (Cranmer 2009). The main idea of this model is that a Keplerian disc may be spun-up by the NRPs adding enough angular momentum into the upper atmosphere via resonant waves. It is not clear, however, as to how the NRPs are converted to resonant waves. This is due to the NRPs corresponding to low-frequency evanescent waves in the stellar photosheres of hot stars. Higher frequency resonant waves, however, can grow in amplitude as they move higher into the stellar atmosphere, propagate outwards and steepen into shocks. Angular momentum is then transported to higher regions above the star as the wave pressure resulting from shocks increases. The model was tested with a B2V star rotating at $0.7v_{crit}$ and it was demonstrated that even at this relatively slow rotation speed the inner boundary conditions needed for a dense Keplerian disc were able to be created by the NRPs.

1.3 X-ray properties

The X-ray emission from BeXB systems is important in the discovery of the objects. BeXBs generally exhibit transient X-ray behaviour, however persistent sources displaying weak X-ray emission have been reported (e.g. Reig & Roche 1999). Transient BeXBs undergo periods of outburst, when the X-ray luminosity can suddenly increase by a factor of $\gtrsim 10$ relative to the quiescent state (Stella et al. 1986, Okazaki & Negueruela 2001). The X-ray emission in these systems is usually pulsed at the NS spin period as a result of the misalignment of the spin axis of the NS with its magnetic axis. The

material from the circumstellar disc is channeled by the magnetic field lines of the NS, with part of the material transported to the north magnetic pole and the other to the south magnetic pole. The large gravitational well of the NS causes the material to be accelerated to high velocities resulting in free-fall motion. Once the material makes contact with the surface of the NS the kinetic energy is converted to thermal energy and is radiated away as X-rays. The luminosity of the X-ray emission is proportional to the mass accretion rate: $L \propto \frac{\dot{M}}{R_X}$ (Stella et al. 1986). The X-ray pulses detected from the NS are the result of the regions where the X-ray radiation is produced moving in and out of our line of sight (Hellier 2001, Carroll & Ostlie 2006). The compact objects in BeXBs are relatively young pulsars with strong magnetic fields ($B \gtrsim 10^{12}$ G, Stella et al. 1986). The transient nature of BeXBs is characterised by two types of X-ray outburst events: type I and type II (Fig. 1.11, 1.12, 1.13).

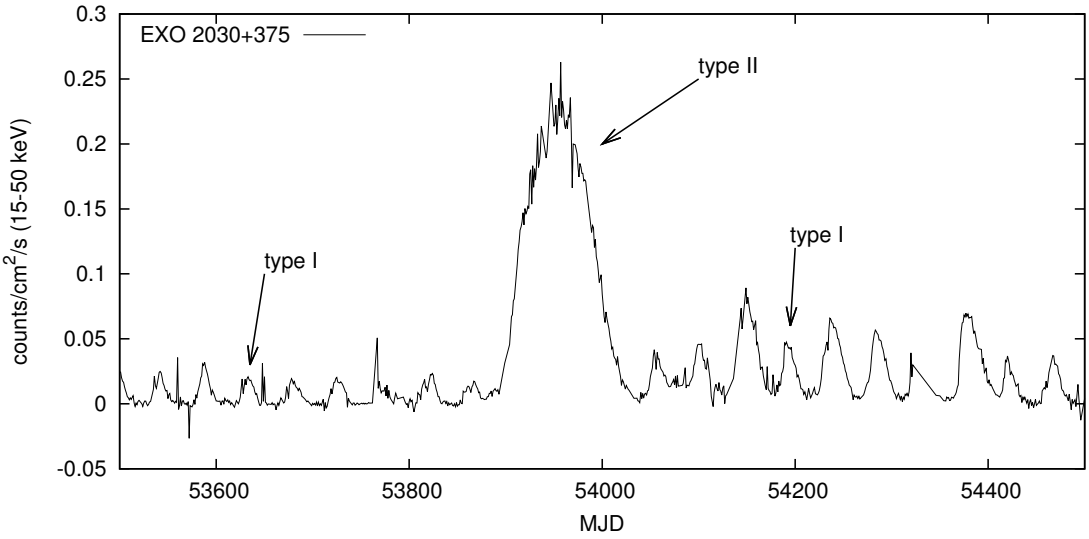

Figure 1.11: Swift/BAT X-ray lightcurve of EXO 2030+375 characterised by rare type II outbursts and long series of type I outbursts separated by the orbital period of the NS.

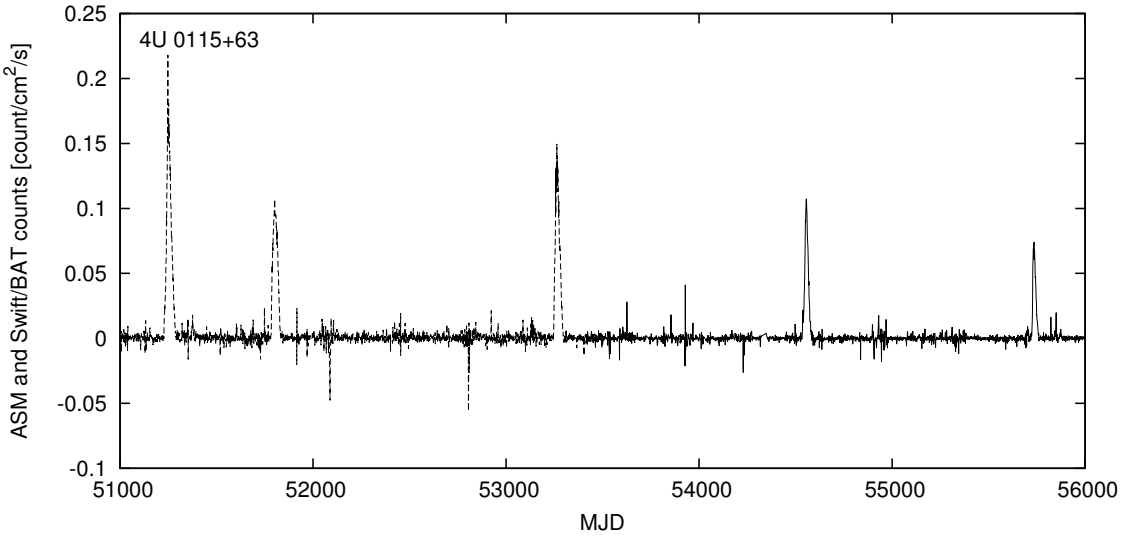

Figure 1.12: ASM (dashed line) and Swift/BAT (solid line) X-ray lightcurve of 4U 0115+63 characterised by type II outbursts.

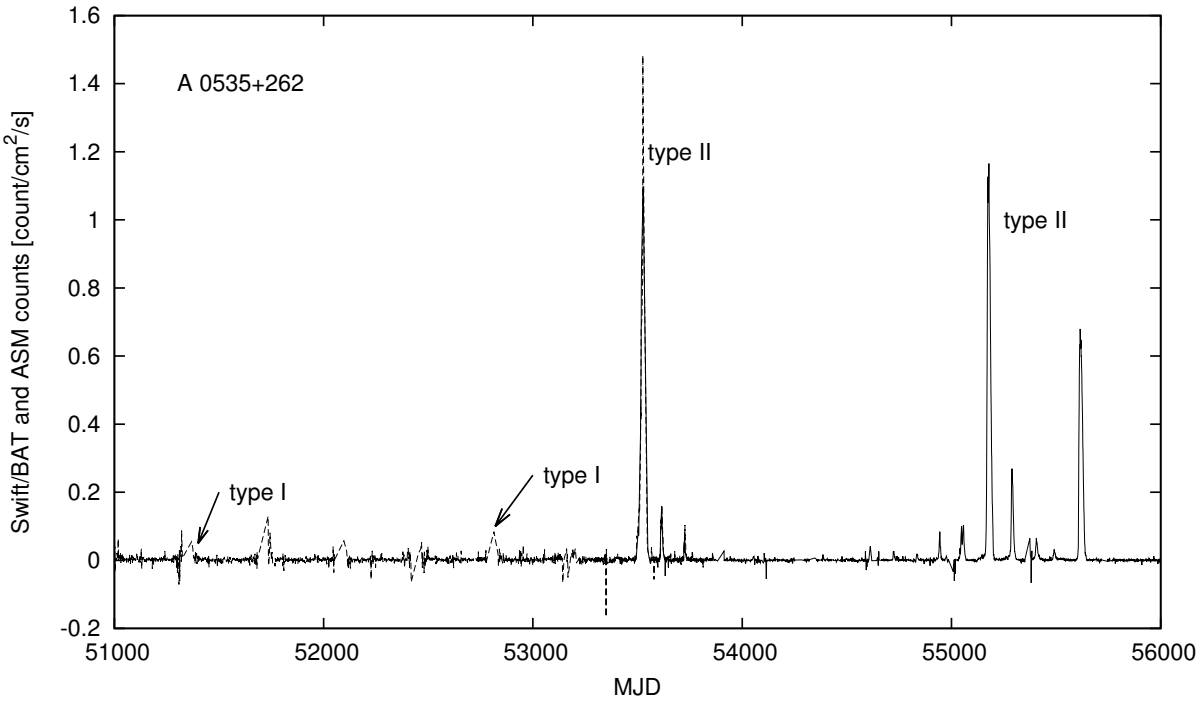

Figure 1.13: ASM (dashed line) and Swift/BAT (solid line) X-ray lightcurve of A 0535+262 displaying both type I and type II outbursts.

1.3.1 Type I outbursts

Type I outbursts (also termed "normal" outbursts) are X-ray events that are regular in occurrence and are observed to peak at/near periastron passage of the NS. The luminosity of type I outbursts can reach values up to 10^{37} erg.s^{-1} (Stella et al. 1986). Type I outbursts are generally separated by the orbital period of the NS and last for a relatively short duration ($\sim$0.2 - 0.3 P_{orb}, Reig 2007).

1.3.2 Type II outbursts

Type II outbursts (also termed "giant" outbursts) are X-ray events with much larger intensities than type I outbursts, as they can reach the Eddington limit* ($L \gtrsim 10^{37}$ erg.s^{-1}) and last longer (several weeks to months) (Stella et al. 1986, Negueruela et al. 1998). Type II outbursts occur less frequently than type I outbursts and do not show any modulation with the orbital period, as they can occur at any orbital phase.

1.4 Viscous decretion disc model

Reig et al. (1997) did a study of H_α emission line properties of Be stars and how they relate with orbital period using a sample of BeXBs. It was found that there exists a correlation between the orbital period and the strength of the H_α emission line (i.e EW(H_α), Fig. 1.14). Since the EW(H_α) is used as a trace of the disc size, the implication of the results is that systems with short periods have smaller circumstellar discs and thus the NS in these systems acts as an impediment, limiting the disc size. The systems with longer periods (wider orbits) appear to have larger discs, as the NS in its eccentric orbit allows material that forms the disc to drift outwards. This was the the first observational evidence of disc truncation in BeXBs. Theoretical models (combined with observational data) have since been developed to demonstrate how circumstellar discs in BeXBs interact with the NS, leading to disc truncation (Okazaki & Negueruela 2001, Negueruela et al. 2001, Okazaki & Negueruela 2001). The modeling of Be discs in the context of viscous transportation of material outwards was first presented by Lee et al. (1991). The viscous decretion disc model explains that angular momentum is added to the inner regions of the disc by the Be star and this increases the angular velocity to Keplerian. Thus the disc is rotationally dominated (the radial velocity is negligible).

*The luminosity at which the radiation pressure outward becomes greater than the gravitational attraction (ram pressure from the gas; Frank et al. 2002).

The modeling of the discs is done with the assumption that the disc is isothermal and the Shakura-Sunyaev α-prescription for viscous stress is applied. Thus the decretion discs surrounding Be stars function in a way to similar to accretion discs with the exception of mass flow rate, $\dot{M}$, which operates in the opposite direction (i.e material in decretion discs flows from the inner regions to the outer parts).

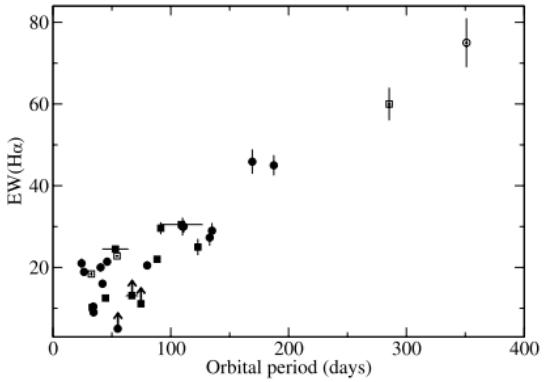

Figure 1.14: An updated version of P_{orb} vs. EW(H_α). The circle symbols represent Milky Way objects and square symbols represent Small Magellanic Clouds objects. Credit: Reig et al. (2007).

The material in the disc drifts outwards until the resonant torque applied by the NS in its orbit becomes dominant. This only occurs at particular radii where the ratio between the angular frequency of the disc rotation and angular frequency of the orbit is an integer (the ratio is represented by n:1). With T_{vis} representing the viscous torque and T_{res} the resonant torque, truncation occurs when the following condition is met (Okazaki & Negueruela (2001)):

$$T_{vis} + T_{res} \leq 0$$

How effectively the disc is truncated is dependent on the gap size, Δr, between the truncation radius and the the mean critical lobe radius at periastron passage (the wider the gap size the more efficient the truncation), as well as α, the viscosity parameter. Okazaki & Negueruela (2001) applied the model to a sample of BeXBs with different orbital parameters. For systems with large eccentricity ($e \geq 0.6$) it was found that disc truncation is not efficient (Δr is relatively small for these systems), since the truncation radius is close to or larger than the critical lobe radius at periastron passage. Thus

in these systems regular type I outbursts are expected at periastron passage since the NS will be able to accrete sufficient matter. Systems with low eccentricity have their discs efficiently truncated (Δr is larger in these systems). Thus no type I outbursts are expected to be seen in these systems and only type II outbursts are expected to occur. Temporary type I outbursts, however, can sometimes be seen to occur if the disc is strongly disturbed. The model is limited with regards to moderately eccentric systems, as it is unable to make precise predictions since the disc behaviour in these systems is influenced by small differences in system parameters.

1.4.1 X-ray outbursts in the framework of the viscous decretion disc model

Type I outbursts

Type I outbursts are further divided into two subclasses (Fig. 1.15, Okazaki & Negueruela 2001): regular type I and temporary type I. Regular type I outbursts occur when an axisymmetric viscous decretion disc grows large enough for material to overflow through the first Lagrangian point (L_1) at periastron passage of the NS. Temporary type I outbursts occur when the axis of a strongly disturbed, elongated disc is in the direction of periastron passage of the NS, allowing material to overflow through the L_1 point.
In a recent extension of the viscous disc model, Okazaki et al. (2013) proposed that type I outbursts are the product of radiatively inefficient accretion flows (RIAFs), based on 3D smoothed-particle hydrodynamics (SPH) simulations results. In this scenario, the material is carried-over to the NS from the outermost part of the circumstellar disc through a tidal stream. Okazaki et al. demonstrated that with the RIAF scenario the accretion rates and accretion timescales are in agreement with X-ray luminosities and duration of type I outbursts, respectively, compared to the standard radiative-cooling disc model (Shakura & Sunyaev 1973) in which the timescale of viscous accretion is longer than the orbital period of the NS, suggesting that the accretion disc (if formed) is not transient - contradicting observational analysis.

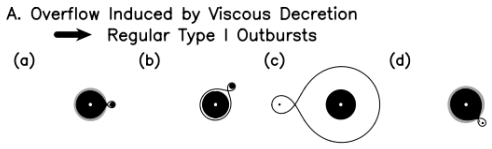

(a) The NS accretes matter from the axysymmetric disc at periastron passage, resulting in a series of type I outbursts. As the NS orbits far from the Be star the overflow of mass onto the NS ceases. The disc grows in size via viscous decretion until the NS reaches periastron passage again leading to type I outburst.

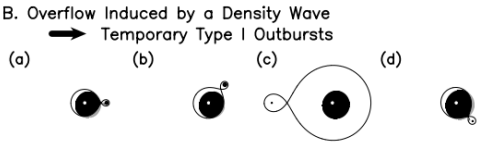

(b) The NS accretes matter from an elongated disc at periastron passage, resulting in a series of temporary type I outbursts. While the NS orbits far from periastron passage the disc grows in size until the NS accretes matter again at periastron passage (if the axis of elongation is still in the direction of periastron passage.)

Figure 1.15: The two subclasses of type I outbursts. Credit: Okazaki & Negueruela (2001).

Type II outbursts

The exact mechanism responsible for type II outbursts has been investigated (e.g. Martin et al. 2011, Moritani et al. 2011; 2013) and remains poorly understood. Martin et al. (2011) made numerical models of viscous decretion discs to suggest that type II outbursts are the result of the interaction of fast stellar winds with warped discs which are caused by tidal interactions with a NS in a misaligned orbit. Observational evidence of a precessing warped disc resulting in type II outbursts has been suggested, as dramatic changes in the H_α emission line have been reported around the period of giant outbursts (Negueruela et al. 2001, Reig et al. 2007, Moritani et al. 2011; 2013). Since the shape of the H_α emission line profile is a result of an inclination effect of the circumstellar disc to our line of sight (single-peaked profiles result from a face-on view of the disc and double-peaked/shell profiles are from high disc inclination), the line profile variations between single-peak and double-peak/shell profiles on such relatively short timescales (e.g. less than a year in Negueruela et al. 2001) is indicative of a precessing warped disc, as such timescales are too short for a precessing spin axis of the Be star, which are on the order of 1000 days (e.g. Lipunov & Nazin 1994).

Okazaki et al. (2013), based on 3D SPH simulation results, proposed that the mechanism responsible for type II outbursts is the Bondi-Hoyle-Lyttleton (BHL) accretion of matter from the outermost warped region of the disc when the NS is at/near periastron passage. This occurs in systems where the circumstellar disc is misaligned with orbital plane and precesses. The process was shown numerically to produce X-ray luminosities in agreement to those reported from observations.

Chapter 2

LS I +61 303

2.1 Introduction

Five known X-ray binaries exhibit very high energy emission in the MeV - TeV range, namely LS I +61 303, PSR B1259-63, LS 5039, HESS J0632+057 and 1FGL J1018.6-5856. We will focus on LS I +61 303 (LSI henceforth) in this thesis, a HMXB falling under the subclass of BeXBs. The system was discovered during a survey of the Galactic plane for a class of highly variable radio sources, when it was found to coincide in position with the COS B gamma-ray source CG 135+1 (Gregory & Taylor 1978). It has since been studied with different facilities at different wavelengths - in the radio (e.g. Gregory & Taylor 1978), X-rays (e.g. Chernyakova et al. 2012), gamma-rays (e.g. Albert et al. 2008) and in the optical (e.g. Paredes et al. 1994). A study of the column density toward LSI by Frail & Hjellming (1991) revealed that the system is at a distance of 2.0 $\pm$ 0.2 kpc. The system consists of a rapidly rotating B0Ve star with a circumstellar disc (Hutchings & Crampton 1981) and a compact object in an eccentric orbit with $e = 0.537 \pm 0.034$ (Aragona et al. 2009). Radio data analysis done by Gregory (2002) reveals an orbital period of $P = 26.4960 \pm 0.0028$ days, which is in agreement with that derived from infrared (Paredes et al. 1994), optical (Zamanov et al. 1999), gamma-ray (Massi 2004) and X-ray observations (Paredes et al. 1997). The zero orbital phase, by convention, has been set to JD = 2 443 366.775, which is the date of the first radio observation of the system (Gregory & Taylor 1982). Despite the effort that has been put into gaining an understanding of the system with the wealth of data available, the nature of the compact companion is still not fully understood.

A number of studies suggest that the compact object is a neutron star (e.g Dubus

(2006)), while others suggest that a black hole could be the source of energy (e.g Massi 2004). The two main competing models that try to explain the physics of the system as well as give an indication of the nature of the compact object are the microquasar model and the pulsar wind model.

2.2 Microquasar model

Microquasars are stellar binary systems which host non-thermal jets. These systems are composed of a main sequence star and a compact object. The compact object could either be a neutron star ($1.4M_{\odot} \leq M \leq 2.5M_{\odot}$) or a stellar black hole ($M \geq 2.5M_{\odot}$). Microquasars are classed high-mass or low-mass, depending on the mass of the main sequence star. If the system hosts an early-type O or B star then it is called a high-mass microquasar, whereas if it is a star with a later spectral type (A, F or G) it is called a low-mass microquasar. Microquasars are scaled-down versions of Active Galactic Nuclei (AGN), since they have several of their main features in common, such as a compact object accreting matter, accretion disc around the compact object and relativistic jets emerging from the compact object (Massi 2005).

Mass accretion occurs when the compact object accretes matter from the massive companion. An accretion disc around the compact companion will be created as material is transferred. The orbital motion of the two objects prevents matter from falling directly onto the compact companion, as the material has some angular momentum. This means that the material will orbit the compact object, and as more matter is accreted and interacts with material on the outer layers, angular momentum is transferred via the Shakura-Sunyaev viscosity mechanism. Thus some of the material will spiral inwards, with some of the angular momentum being moved outward (King 1996).

The formation of jets in astrophysical systems is still not fully understood. Many of the theoretical models proposed to explain the jet-formation process involve variations of the magnetohydrodynamic (MHD) jet theory (Blandford & Znajek 1977, Punsly & Coroniti 1990, Takahashi et al. 1990, Meier & Koide 2000, Meier et al. 2001, Klein-Wolt et al. 2002, Fender 2003). The main idea of the MHD jet theory (Fig. 2.1) is that for weak magnetic fields near the inner radius (R_{in}), the plasma pressure from the accretion disc will have enough dominance over the magnetic field pressure to bend the magnetic field lines and twist them as the disc rotates differentially. The magnetic field strength increases as the field lines are compressed, thereby increasing the magnetic field pressure.

Gas at the surface of the disc will start to follow the magnetic field lines, as the magnetic field pressure becomes larger than the gas pressure. Radial accretion in the disc also increases, since angular momentum is also extracted from the disc surface. The first

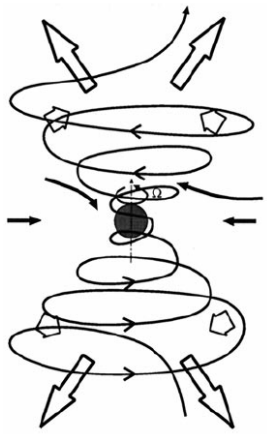

Figure 2.1: A schematic diagram illustrating the MHD model for jet formation. The solid arrows represent incoming, rotating material which winds the magnetic field lines. the open arrows represent the material expelled out as jet outflow by the magnetic pressure. Credit: Meier et al. 2001.

suggestion that LSI could be a microquasar comes from Taylor & Gregory (1982) when they explained that the non-thermal emission arises from an accretion process. The analysis of the *European VLBI Network* (EVN) data by Massi et al. (2001) revealed a jet-like elongation extending to hundreds of AU. The elongated radio morphology observed was interpreted as a Doppler boosted jet of a symmetric pair. When combined with data from other epochs, there is a suggestion that the jet is precessing. A lower limit for the jet speed of $0.4c$ was derived, which falls in the range of $0.1c$ - $0.92c$ for other microquasars in the galaxy (Mirabel & Rodríguez 1999). It is possible that the compact object is a stellar black hole from the range of values of the mass function of $0.0028 < f < 0.027$ (Casares et al. 2005), where the mass function is calculated (Charles & Wagner 1996):

$$f(M_{\rm X}, M) = \frac{P_{\rm orb} K_{\rm c}^3}{2\pi G} = \frac{M_{\rm X}^3 sin^3 i}{(M_{\rm X} + M)^2}$$

with:

$M_{\rm X}$ - mass of the compact object
M - mass of Be star
i - the inclination of the orbit
$P_{\rm orb}$ - the orbital period
$K_{\rm c}$ - the amplitude of the radial velocity variations
G - the gravitational constant

For LSI, this gives a range of the mass of the compact companion of $1.4M_{\odot} \leq M_{\rm X} \leq 3.8M_{\odot}$ (Punsly 1999, Massi 2004).
The high energy gamma rays result from inverse Compton (IC) interactions (leptonic model) between relativistic electrons from the jets and the outflowing photons from the more massive Be star or those produced locally by synchrotron processes (Bosch-Ramon et al. 2006). Another mechanism for producing gamma-rays is the inelastic *pp* interactions (hadronic model), where the relativistic protons in the jet interact with protons in the wind of the Be star equatorial disc through the reaction (Romero et al. 2005):

$$p + p \rightarrow p + p + \xi_{\pi^0}\pi^0 + \xi_{\pi^{\pm}}(\pi^+ + \pi^-),$$

where ξ_{π} is the corresponding multiplicity. The pion decay will then lead to the gamma-ray emission observed at $E > 1$ GeV (Romero et al. 2005, Orellana & Romero 2007). Thus, at/near periastron passage (orbital phase ~ 0.23, based on the ephemeris from Gregory & Taylor 1982), gamma-rays and X-rays are expected and not radio outbursts. When the compact object is at a greater distance from the more massive companion, radio outbursts will then be observed since IC losses are less severe and the electrons are able to propagate out of the orbital plane. This is consistent with observations, as gamma-rays are seen to peak at orbital phase range 0.2 - 0.5 (Massi 2004), while X-rays peak at range 0.43 - 0.47 (Gregory 2002). Radio outbursts are seen to occur at a larger range of the orbital phase, 0.45 - 0.95 (Gregory 2002), but the bright radio flux is observed at orbital phase ∼0.6 (Paredes et al. 1990).

Matter is expected to be accreted twice in the 26.5 day eccentric orbit. With $\rho_{\rm wind}$ representing the density of the Be star wind and $v_{\rm rel}$ representing the relative speed between the accreting object and the wind, it has been shown by Taylor et al. (1992) and Marti & Paredes (1995) that the mass accretion rate has the form $\dot{M} \propto \frac{\rho_{\rm wind}}{v_{\rm rel}^3}$ for an eccentric orbit. Thus for LSI, an accretion peak will occur at periastron passage (orbital

phase ∼0.23) when the wind density from the Be star is at its highest. The second peak occurs farther from periastron passage (orbital phase ∼0.5) when the orbital velocity of the compact object has the same direction as the wind outflow and the relative velocity is at a minimum (Marti & Paredes 1995). Variations in the wind velocity of the Be star causes the second peak to occur at different phases (Massi 2004). It has been shown that the accretion rate at both the maxima are above the Eddington limit (Marti & Paredes 1995; Romero et al. 2007). Fig. 2.2 shows the result of simulations performed with a three dimensional, smoothed particle hydrodynamics (SPH) code of the accretion rate as a function of orbital phase (Romero et al. 2007). The primary, narrow peak occurs at periastron passage and the secondary, broader peak occurs at orbital phase ∼ 0.52.

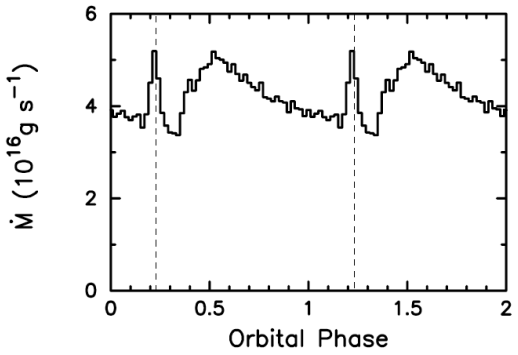

Figure 2.2: Accretion rate as a function of phase from SPH simulations. The dashed line lines show the phase of the periastron passage (∼0.23). From Romero et al. 2007.

2.3 Pulsar wind model

Pulsars are compact stellar systems with very strong magnetic strengths at 10^{11-12}G (Wright 2005) and are rapid rotators. The axis of rotation is misaligned with the magnetic axis, giving rise to the lighthouse effect observed (Fig. 2.3). The magnetic field causes charged particles to be accelerated out along the field lines as the star spins on its axis, with pulsed signals passing along our line of sight once (or twice if both the magnetic poles cross our line of sight) per rotational period.

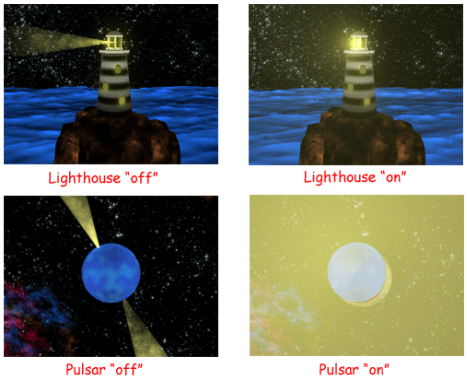

Figure 2.3: Illustration of the misalignment of the magnetic axis and the rotation axis of a pulsar, which leads to the lighthouse effect. Credit: http//www.airynothing.com/high_energy_tutorial/sources/pulsars.html

In BeXBs the neutron star orbits around the optical companion with a variable circumstellar disc. The pulsar can be embedded in the disc material as it orbits closer to the Be star. The relativistic wind from the pulsar forms an $e^{\pm}$ plasma in the magnetosphere. As this wind expands, it will eventually interact with the slow-moving wind from the Be star, creating a shock region at a distance r_s from the pulsar. The distance of the shock from the pulsar can be found by equating the pulsar radiation pressure to the ram pressure of the Be star (Tavani et al. 1994):

$$\frac{r_{\rm s}/d(\theta)}{1-[r_{\rm s}/d(\theta)]^{2-n/2}} = (\frac{\dot{E}_{\rm R} f}{c\dot{M}v_0})^{1/2}[\frac{R_*}{d(\theta)}]^{n/2-1},$$

where d is the pulsar-Be star separation (periastron passage at $\theta = 180°$); $\dot{M}$ is the mass outflow rate from the Be star; v_0 is the outflow velocity at the surface of the Be star; R_* is the radius of the Be star; f is the fraction of $4\pi sr$ into which mass loss occurs; $\dot{E}_{\rm R}$ is the spin-down luminosity of the pulsar; n is the outflow exponent ($2 < n < 4$).

A bow-shaped shock region will form from the interaction of the fast-moving pulsar wind with the homogenous wind from the Be star. The $e^{\pm}$ pairs will be accelerated nonthermally at the pulsar wind termination shock (Tavani & Arons 1997).
The pulsar wind model (PWM) for LSI was first proposed by Maraschi & Treves (1981), suggesting that the compact companion is a moderately young pulsar of age 10^{4-5} years.

Dubus (2006) suggested that matter is not accreted by the compact companion, as supported by the lack of strong X-ray variability on timescales of a few seconds detected. Thus the pressure from the relativistic pulsar wind will then stop the matter from the Be star, and only small variability will be observed due to the very low accretion and stellar wind fluctuations. Dubus (2006) suggests that due to the lack of highly relativistic bulk motion directed towards the line of sight, the system may possibly be a binary pulsar instead of a microquasar. VLBA images presented by Dhawan et al. (2006), covering a full orbit with spacing of 3 days (Fig. 2.4) reveal an extended, comet-like structure pointing away from the Be star. In their work, Dhawan et al. (2006) found no relativistic measurements of the velocity of the cometary tail, with outflow velocites ranging from $v \sim 7500$ km/s at periastron to $v \sim 1000$ km/s at apastron. The authors conclude that the elongated structure is a pulsar wind nebular shaped by the anisotropic environment, instead of a jet.

Neronov & Chernyakova (2007) presented a variation of the PWM for LSI, where they

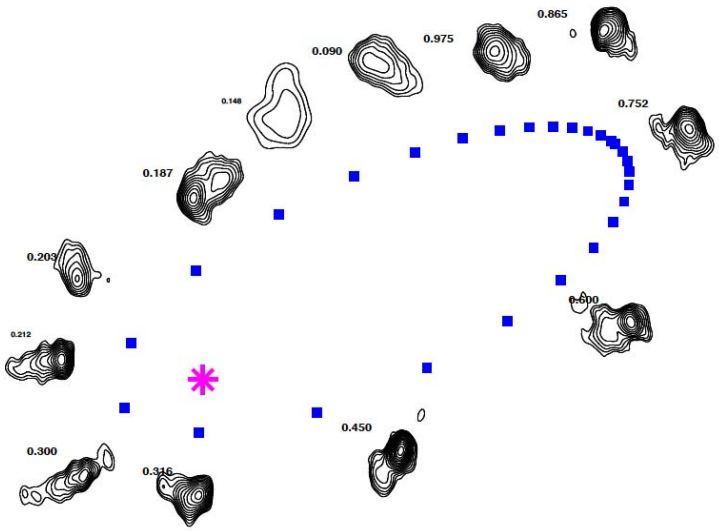

Figure 2.4: VLBA images at 3.6 cm plotted with orbital phase showing the variability of the structure around the compact object. The asterisk shows the position of the Be star. Credit: Dhawan et al. 2006.

suggested that the wind from the pulsar interacts with an inhomogeneous wind from the Be star (Fig. 2.5). An irregularly shaped region will form from the interaction, instead of a smooth bow-shaped structure. In this model, the authors explain the origin of the multiwavelength emission, as well as other characteristics of the emission ob-

served throughout the orbital cycle. An "onion-like" structure of the pulsar wind nebula (PWN) is assumed, where different layers represent the different dominant processes taking place: in the innermost region, Coulomb losses are dominant; the layer surrounding that is dominated by IC losses and synchrotron loss dominates the outermost region (Fig. 2.6). In their model, Neronov & Chernyakova demonstrated that when the pulsar is passing through the innermost region of the nebula, close to periastron passage, the high energy electrons (100 GeV-TeV) cause pair cascades. Radio emission will peak farther from periastron, from the supply of lower energy electrons (10 MeV) by the fast polar wind from the Be star. The energy from these electrons will be lost closer to periastron passage since they heat up the stellar wind, hence no radio emission is detected at periastron passage. IC scattering of photons from the Be star will cause the X-ray luminosity to peak, as the pulsar orbits in the region of the nebula where IC losses dominate.

Figure 2.5: Illustrated representation of the interaction of the fast-moving pulsar wind with the inhomogeneous wind from the Be star. The brown-shaded clumps represent the irregularly-shaped interaction region, instead of a bow-shaped region occurring as expected with a homogeneous Be wind (dashed, red line). The ellipse represents the orbit of the pulsar around the Be star. Credit: Neronov & Chernyakova 2007.

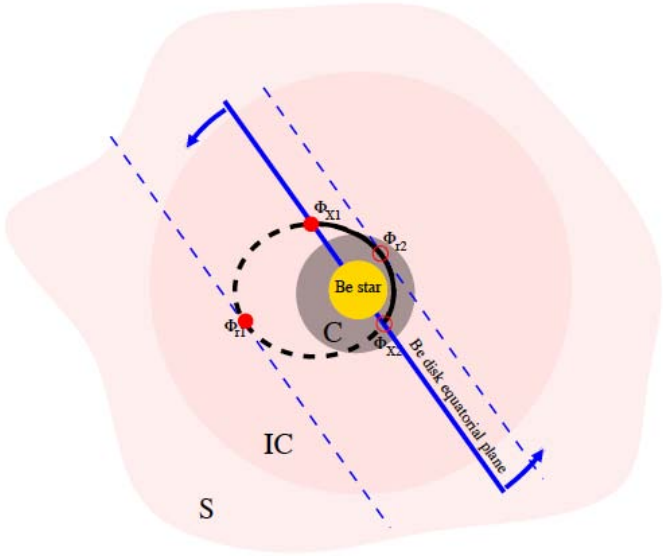

Figure 2.6: The onion-like structure of the PWM. Regions marked 'C', 'IC' and 'S' are where Coulomb losses, inverse Compton losses and synchrotron losses dominate respectively. $\Phi_{\rm r}, \Phi_{\rm X}$ are phases of radio and X-ray maxima respectively. Credit: Neronov & Chernyakova 2007.

The electrons accelerated in the shock region from the interaction of the pulsar wind and Be wind will undergo IC interactions with the stellar photons to produce the gamma-ray emission, as well as the *pp* interactions of the fast-moving protons from the pulsar with the protons in the stellar wind material producing neutral pions which will subsequently decay. The interaction of the electrons with any surrounding magnetic fields will produce synchrotron radiation detected at radio wavelengths, possibly in an elongated structure (e.g. Mirabel 2006, Dhawan et al. 2006).

2.4 Four year superorbital modulation

2.4.1 Radio bands

The peak flux of the radio outburst in LSI displays a four-year modulation. This was first presented by Gregory et al. (1989) when radio data accumulated over ten years at 6 cm was analysed. Fig. 2.7(a) is a plot from the work, displaying variations of the peak radio outburst, with a fitted model curve. Two possible explanations were suggested for the modulation of the radio peaks: variable beaming from a precessing relativistic

jet and variable accretion due to quasi-cyclic Be star envelope variations. Paredes et al. (1990) presented analysis of radio data spanning over 11.4 years. The authors support the long term modulation in the radio outburst peak flux density, where they obtained an improved value of the super orbital period of 1476 ± 7 days by fitting a cosine function to the radio outburst peak flux density light curve (Fig. 2.7(b)) of the form:

$$M(t) = A\cos[\frac{2\pi}{P}(t - t_0)] + B$$

with the following values obtained from the fit:

$A = 144 \pm 5$ mJy

$B = 187 \pm 4$ mJy

$t_0 = 2443599 \pm 28$ (Julian day epoch)

$P = 1476 \pm 7$ days

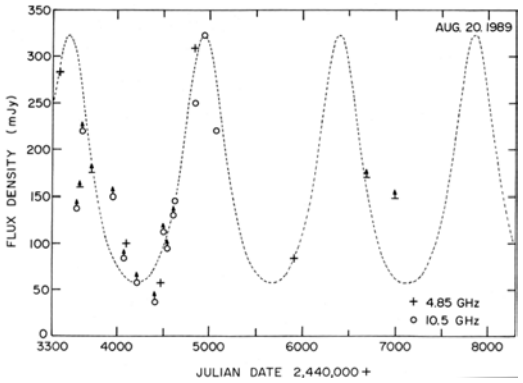

(a) Radio peak flux as a function of time, with a fitted model curve. Data points with arrows show the lower limits. From Gregory et al (1989)

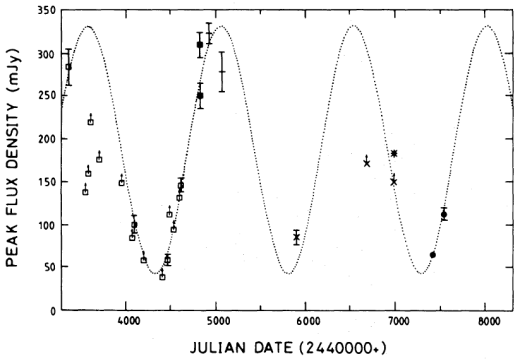

(b) Radio peak flux versus Julian date, with the best fit cosine curve. Data points with arrows show the lower limits. From Paredes et al. (1990).

Figure 2.7

In the analysis of 20 years of radio measurements, Gregory (1999) used Bayesian analysis* to demonstrate the existence of a periodic or quasi-periodic radio outburst peak flux with a mean period of 1632^{+28}_{-33} days. In a follow-up paper to this, Gregory et al. (1999) again used Bayesian analysis* of the same 20 year radio data to demonstrate that the phase of the radio outbursts varies periodically with the same period as the outburst peak flux modulation, and also derive a flux modulation period of 1584^{+14}_{-11} days.
The long term modulation was again derived by Gregory (2002) in the Bayesian analysis of radio data from the National Radio Astronomy Observatory Green Bank Interferometer (GBI) at 1667 ± 8 days, which is the most widely accepted estimate used. An improvement of the orbital period was also achieved, $P = 26.4960 \pm 0.0028$ days.

2.4.2 Optical spectroscopy (H_α)

Zamanov et al. (1999) analysed different properties of the H_α emission line from the system. Using the peak separation, ΔV, and the H_α equivalent width measurements, $EW(H_\alpha)$, the authors demonstrated that the circumstellar disc of the Be star of LSI is among the densest in Be stars. The 26-day orbital period in the H_α emission line was also derived from the ratio of the equivalent widths of the two peaks, $EW(B)/EW(R)$ (Fig. 2.8(a)). $EW(H_\alpha)$ measurements from Paredes et al. (1994) and Zamanov et al. (1996) were also used to study the long term variations of the Be disc, and suggestion of the four year modulation in the H_α emission line was observed. In a plot of the $EW(H_\alpha)$ as a function of time, two peaks are visible which are separated in time by $\sim$1500 days, similar to the $\sim$1600 day superorbital period detected at radio wavelengths. With the possible detection of the orbital period modulation in the H_α emission line, it was suggested that the origin of this periodicity is from the variability of the mass loss rate of the Be star. This explanation would be possible in both the microquasar model and the PWM: in the microquasar model, mass accretion onto the compact companion would vary due to the variable mass loss from the Be star; and in the PWM, the variable mass loss will change the position of the shock front.

Lipunov & Nazin (1994) developed a model for LSI, where they suggested that the Be star is precessing with a period represented by:

*Gregory-Loredo Bayesian algorithm (Gregory & Loredo 1992)

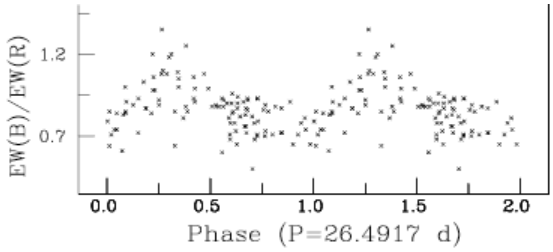

(a) $EW(B)/EW(R)$ versus orbital phase, folded on the 26.4917 day period. From Zamanov et al. (1999)

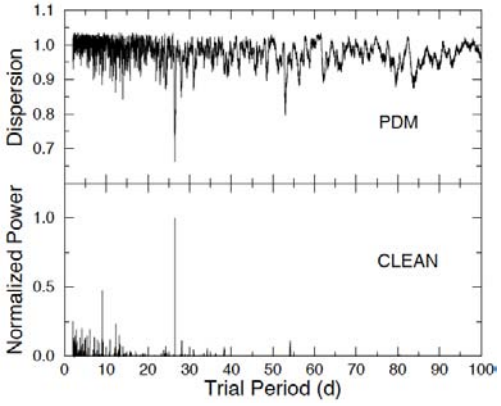

(b) Phase Dispersion Minimization (PDM) periodogram, top, and CLEAN periodogram, bottom, showing the detection of the 26.5 day period

Figure 2.8

$$P_{\rm pr} \simeq \frac{2\pi a^3}{M_{\rm X} R_0} \sqrt{\frac{M_0}{G R_0}}, \tag{2.-4}$$

where a is the semimajor axis of the binary system, $M_{\rm X}$ is the mass of the neutron star, R_0 is the radius of the Be star and M_0 is the mass of the Be star. It is proposed that the precession of the Be star could be responsible for the four-year modulation observed.

2.4.3 X-rays

Using data obtained with the *Rossi X-ray Timing Explorer* (RXTE) Proportional Counter Array (PCA) covering a period between 2007 and 2011, Li et al. (2012) studied the long term X-ray behaviour of LSI at energy range 3-30 keV. Evidence of the four-year super-orbital period was presented. The peak X-ray flux and the modulated flux fraction are plotted as functions of time for a six-month time bin with sine functions fitted with the same period as that obtained from radio analysis by Gregory (2002), $P_{\rm s-o} = 1667$ days (Fig. 2.9)*. The modulated flux fraction is computed by $(c_{\rm max} - c_{\rm min})/(c_{\rm max} + c_{\rm min})$,

*The peak X-ray flux is the peak flux over the six month period.

with $c_{\max}$ as the maximum count rate and $c_{\min}$ the minimum count rate. As can be seen in Fig. 2.9, the sinusoidal fits are more compatible with the modulated flux fraction, with a shift of 281.8 ± 44 days (superorbital phase of ∼0.2) relative to the radio sinusoidal curve. The sinusoidal function was also fit to the peak flux and modulated flux fraction at other time bins (4, 8 and 12 months), and it was noted that the smaller time bin (4 month bin) shows a greater scatter around the sine function. The evolution of the modulated flux was suggested to be due to the changing behaviour of the compact companion (from being rotationally powered at apastron to displaying the propeller effect at periastron), as well as the change in the mass loss rate from the Be star.

Chernyakova et al. (2012) used monitoring data from *RXTE* to study the long term

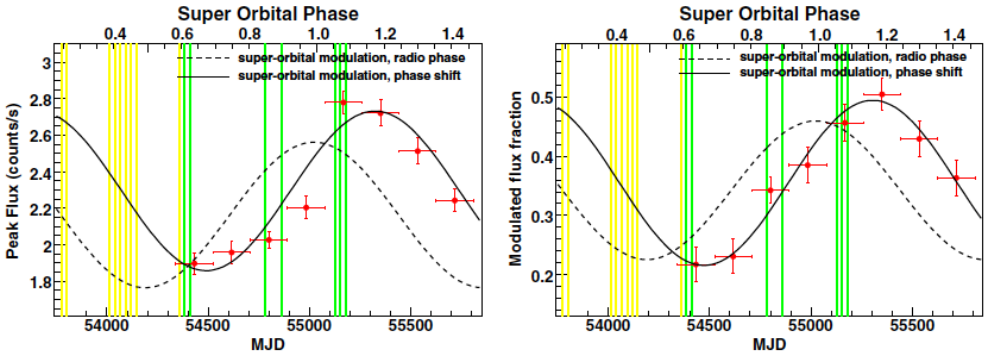

Figure 2.9: Left: peak flux vs MJD. Right: modulated flux fraction vs MJD. Sinusoidal curves are fitted with a period of 1667 days for both plots; the dotted sine curve is the fit obtained without a phase shift and the solid sine curve is the fit with a phase shift. Credit: Li et al. 2012.

properties of the X-ray activity. Fig. 2.10(a) shows the X-ray flux (3-20 keV) as a function of orbital and superorbital phase, where it is seen that the X-ray activity drifts in the orbital phase range $\phi_X \simeq 0.35 - 0.75$ within one superorbital cycle (similar to the drift at radio wavelengths from $\phi_R \simeq 0.5$ to ~ 1.0; Gregory 2002). It is also noted that the radio activity is delayed with respect to the X-ray activity by an orbital phase of $\Delta\phi \simeq 0.2$ (~ 5.3 days). To explain the regularly occurring delay between the radio activity and X-ray activity, it was proposed that the high energy particles produced from the interaction of the winds from the two stellar objects produce X-ray emission via synchrotron processes close to the binary. The radio emission then occurs at larger distances from the binary.

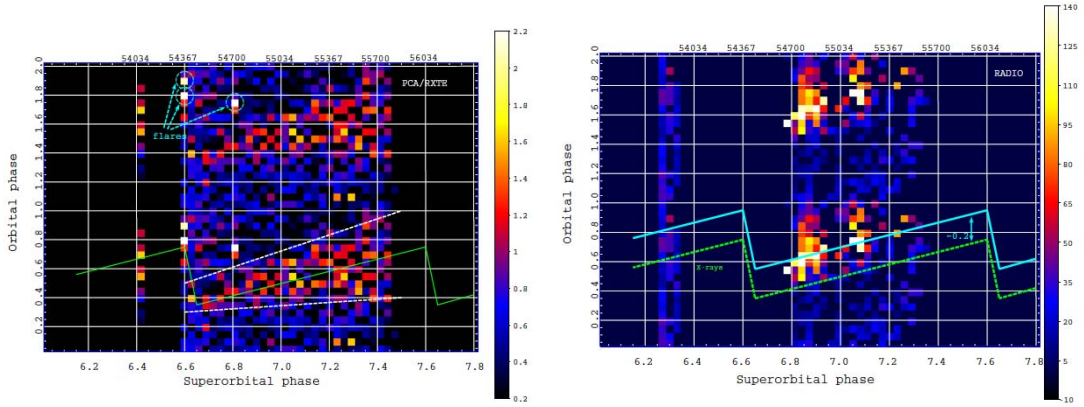

(a) X-ray flux (3-20keV) intensity variation with orbital vs superorbital phase; units presented on colour bar are in mCrab. Credit: Chernyakova et al. 2012.

(b) Radio flux variation with orbital vs superorbital phase; units presented on colour bar are in mJy. Credit: Chernyakova et al. 2012.

Figure 2.10

Chapter 3

Instruments and Observations

3.1 The Southern African Large Telescope

Figure 3.1: The Southern African Large Telescope situated in Sutherland, South Africa. Credit: http://www.salt.ac.za/public-info/picture-gallery/salt-images/outside-view-images/

The **S**outhern **A**frican **L**arge **T**elescope (SALT) is a 10-m class optical telescope situated in Sutherland, Northern Cape (South Africa) at the South African Astronomical Observatory (SAAO) field station. The design of SALT is based on that of the Hobby Eberly Telescope (HET) at McDonald observatory in Texas (Stobie et al. 2000, Buckley 2001). The construction of the telescope was completed in 2005, with first scientific observations taking place later that year (Romero-Colmenero et al. 2007). The spherical primary mirror of SALT has dimensions 10m $\times$11m and is composed of 91

identical hexagonal segments with spherical surfaces. The primary mirror is tilted 37° to the zenith (Buckley et al. 2006). SALT is the optical analogue of the Arecibo radio telescope, in that the primary mirror is fixed in altitude and azimuth while the photons are directed from the primary mirror to a 4-mirror spherical aberration corrector (SAC) at the prime focus with a moving off-centre tracker that follows the object under study (Buckley 2001, Buckley et al. 2006). The telescope is restricted in declination to a range $+10° \geq \delta \geq -75°$ (Fig. 3.2), allowing observation times of 1-2 hours which can be extended up to 5 hours for extreme declinations by azimuth re-pointing of the telescope (Buckley 2001, Buckley et al. 2006, Buckley 2013).

SALT is an international project, with operation funding and construction costs hav-

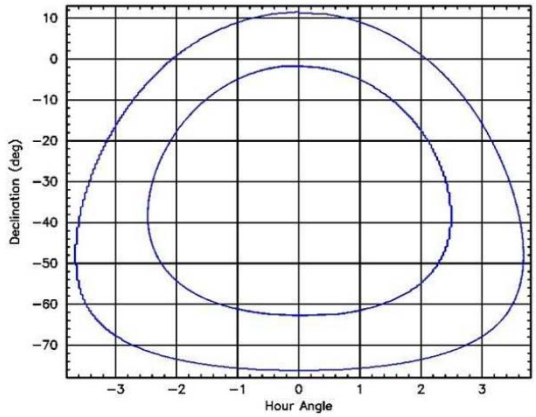

Figure 3.2: The annulus of visibility for SALT which represents ∼12 % of the instantaneously visible sky. The time of observation available for a particular object is determined by the length of time it takes the object to cross the annulus. Credit: Buckley (2013)

.

ing been supplied by different institutions (Buckley et al. 2006): The South African National Research Foundation (NRF) with 34 % of the observing shares, University of Wisconsin-Madison (15 %), Rutgers University (10 %), Dartmouth College (9 %), Nicolus Copernicus Astronomical Centre of Polish Academy of Sciences (9 %) and others (< 6%; American Museum of National History, Carnegie Mellon University, the Indian Inter-University Centre for Astronomy and Astrophysics, University Canterbury, University of North Carolina, Göttingen University and UK SALT Consortium).

Observations performed with SALT are executed by the SALT astronomy operations staff and not directly by the proposer(s) of the observing programme(s). For observa-

tions to be undertaken with SALT, users carry out various phases of planning using web-based tools available (Buckley 2013). In phase I of the proposal, the principal investigator (PI) provides information about the proposed programme, which includes scientific justification to assure the viability of the programme. Once the proposal has been approved and time has been allocated for the observations, the PI can proceed with phase II of the proposal. In phase II the user provides a more detailed description of how the observations should be carried out (e.g exposure times, information on signal-to-noise ratio and other instrument configurations). Once the phase II proposal has been submitted the observations can then be executed by the SALT astronomer on duty and when the data is available the PI will then be notified to download the files (Buckley 2013).
SALT has a suite of instruments which enable the telescope to have a wide range of capabilities. The three first generation instruments operating on the telescope are (Buckley 2005, Buckley et al. 2006):

- SALTICAM - an imaging and acquisition camera which operates in the UV - visible range (320 - 900 nm). SALTICAM was installed mid-2005 and the first science results with SALT were obtained using the instrument in the high-speed unfiltered photometric observations of polars (O'Donoghue et al. 2006).

- Robert Stobie Spectrograph (RSS) - An imaging spectrograph, formerly known as the Prime Focus Imaging Spectrograph (PFIS) and renamed in honour of a previous SAAO director. RSS is versatile, in that it is able to operate in various modes to satisfy a range of scientific goals: longslit spectroscopy, polarimetry, multi-object spectroscopy, high time-resolution spectroscopy and Fabry-Perot imaging spectroscopy (Buckley 2005, Buckley et al. 2007).

- High resolution spectrograph (HRS) - A fibre-fed cross dispersed échelon spectrograph currently undergoing science verification phase. The HRS is a dual-beam instrument with the blue arm covering a wavelength range 3700 - 5500 Å and the red arm covering range 5500 - 8900 Å. High resolution spectra are able to be obtained with HRS at different resolution modes (Barnes et al. 2008): $R \sim 16000, R \sim 37000, R \sim 67000$.

SALT is shown in Fig. 3.1.

3.1.1 Observations

The spectroscopic data in our monitoring programme was taken with the RSS in longslit mode with the PG2300 grating (lines ruled at 2300 l/mm) at a grating angle of ∼50° (wavelength coverage 6200 - 7000 Å). A slit width of 2 arcsecs was used for the observations. A summary of the observations of A1118-617 is provided in Table 3.1.

Table 3.1: Observation summary of A1118-617 with SALT.

Observation dates (DD/MM/YY)	Grating	Wavelength range(Å)	Exp. time(s)	Slit Width (arcsec)	Resolution (Å)	Dispersion (Å/pix)
24/01/2013	PG2300	6200 - 7000	180	1.5	∼1.6	0.27
26/02/2013	PG2300	6200 - 7000	180	1.5	∼1.6	0.27

The data obtained with SALT is downloaded by the user in different packages, one contains raw unreduced data and the other contains semi-reduced data which has been processed with the SALT data reduction pipeline. The pipeline performs the following tasks (Crawford et al. 2012): overscan correction, bias subtraction, gain correction and corrections for amplifier cross-talk. Thus the data reduction steps remaining for our purposes were those required to calibrate the wavelength of the spectra. The one-dimensional spectra were extracted from the Multi-Extension FITS (MEF) files, in preparation for the wavelength calibration process. The cosmic rays in the image were first removed using LACOSMIC (van Dokkum 2001), with the settings (i.e. the sigma limit - the detection limit for cosmic rays) configured to allow for the removal of cosmic rays without affecting the science data (such as the object emission lines) and the sky pixels (Fig. 3.3). This process was done repeatedly, starting with small values of the sigma limit (removal of the weakest cosmic rays), and adjusting these according to the number of cosmic rays removed in the preceding step(s) after inspecting the spectra by eye. The wavelength calibration process was performed using version 2.15.1 of IRAF*.

The emission lines in the observed arc were fit with those of reference SALT spectra using a Neon lamp. A minimum of 10 lines were identified across the whole wavelength range for good accuracy, while weak and saturated lines were avoided (Fig. 3.4). The identified arc row was used as a reference to reidentify the lines in the rows of the 2D arc frame. The background level was then defined, as well as the object spectrum region

*Image Reduction and Analysis Facility: iraf.noao.edu

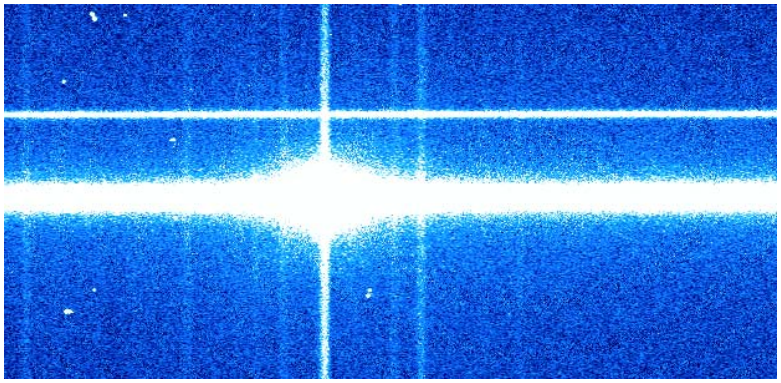

(a) The semi-reduced spectrum of A1118-617 with cosmic rays.

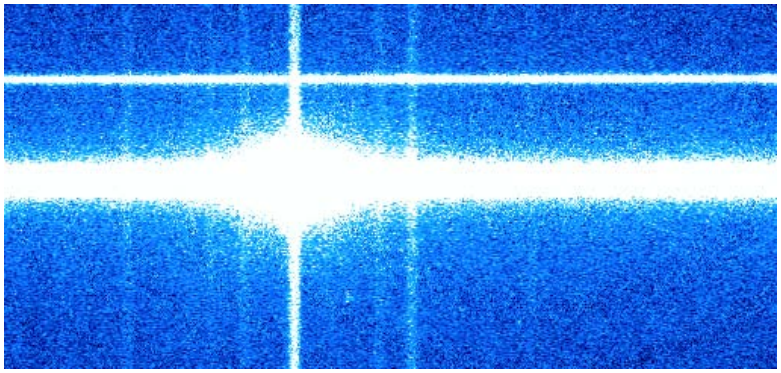

(b) A1118-617 spectrum after cosmic ray removal was applied.

Figure 3.3

and the 1D spectra were extracted. At this point the spectra are wavelength calibrated (Fig. 3.5).

Flux calibration was not applied to the spectra, since the aim of obtaining the spectra was to measure equivalent widths of emission lines as well as to locate the wavelength position of double-peaked H_α emission lines (to calculate the peak separation of the line).

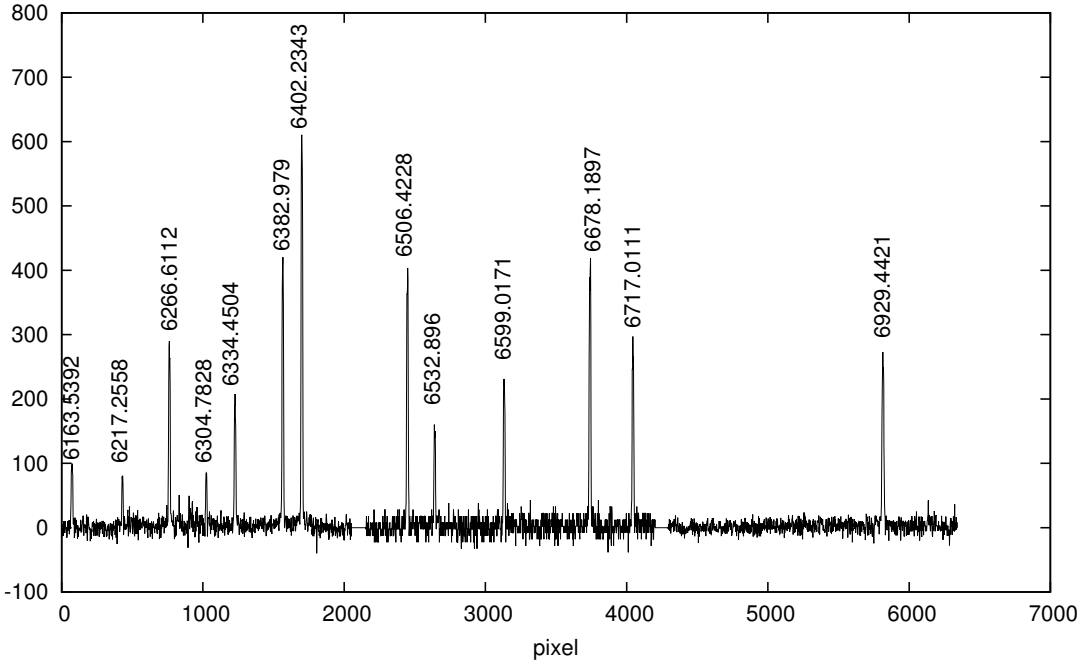

Figure 3.4: Identification of the arc features. The wavelengths are displayed in units of Angstroms.

3.2 The Liverpool Telescope

The Liverpool Telescope (LT) is a 2.0 metre altitude-azimuth design robotic telescope situated in Roque de Los Muchachos Observatory, La Palma. The telescope is owned by Liverpool John Moores University (JMU), and was built by Telescope Technologies Ltd (TTL) (Steele 2001; 2004). As it is an unmanned instrument, LT possesses a Robotic Control System to perform tasks required to make observations efficient (e.g telescope run-up, focusing and observing), as well as to ensure that the conditions are favourable for observations to take place. Located at an altitude of 2363 m, Roque de Los Muchachos provides some of the best locations to perform astronomical observations, being in an isolated region above clouds for a majority of the year with exceptional seeing conditions (Steele 2001). The Canary Islands government has strict laws on the artificial lighting used for outdoor lighting (e.g. brightness of lamp and type of lamp used) to prevent urban light pollution, thus good night sky quality is maintained for astronomical observations to be performed (McNally 1994, Pedani 2004). The primary

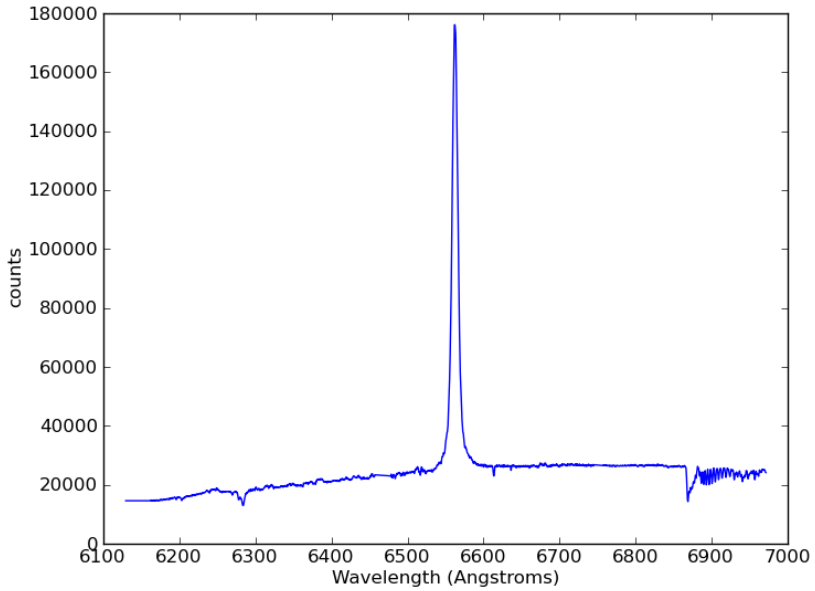

Figure 3.5: An example of a wavelength calibrated SALT spectrum of A 1118-617.

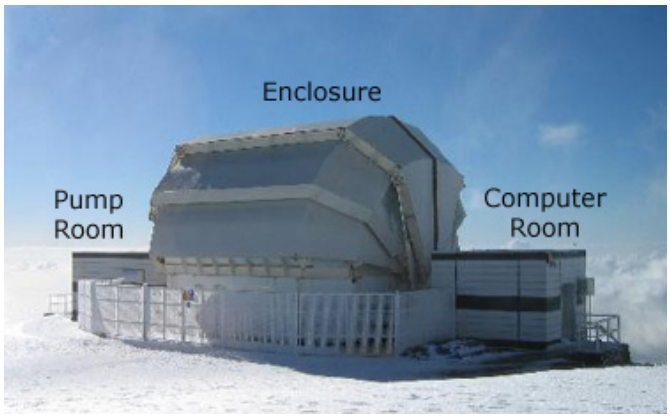

Figure 3.6: The Liverpool telescope situated in Roque de Los Muchachos Observatory, La Palma, with its three main components. Credit: http://telescope.livjm.ac.uk/Info/TelInst/Spec/index.php

scientific goals of LT include small scale surveys, follow-up observations of Targets of Opportunity, monitoring of variable objects, supernovae studies and observing/monitoring targets simultaneously with other telescopes (Steele 2001, Gomboc et al. 2003, Steele 2004). The observing time with the telescope is allocated according to the contribution

of operation costs by the UK Science and Technologies Facilities Council (STFC), Spanish CAT (Time Allocation Committee) and International Scientific Committee (CCI). LT achieved first light in July 2003 and started with science operations in January 2004 (Steele 2004). The telescope consists of three main buildings as shown in Fig. 3.6 : the telescope enclosure, pump room which is responsible for hydraulic operations for the telescope and the computer room.

LT has a list of instruments currently in operation (Steele 2001, Gomboc et al. 2003):

- Infrared-Optical instruments (IO:O and IO:THOR)
- RATCam: an optical CCD camera to be decommissioned at the end of 2013 and replaced by IO:O.
- RISE: fast-readout camera for precision measurement of transiting exoplanet timing.
- RINGO 3: fast-readout imaging polarimeter.
- SkyCam project - to provide simultaneous wide field observations
  - SkyCamA - all sky camera to detect objects up to 6th magnitude.
  - SkyCamT - medium field camera to detect objects up to 12th magnitude.
  - SkyCamZ - zoomed field camera to detect objects up to 18th magnitude.
- FRODOSpec: an integral field unit (IFU) spectrograph.

Instruments already decommissioned on the telescope are the Meaburn spectrograph, RINGO, RINGO 2 and the near infrared camera SupIRCam. The spectra in our monitoring programme were obtained using FRODOSpec.

3.2.1 FRODOSpec

The **F**ibre-fed **RO**botic **D**ual-beam **O**ptical **Spec**trograph (FRODOSpec) is an integral field unit (IFU) spectrograph developed by Liverpool JMU in collaboration with the University of Southampton (Steele 2001). FRODOSpec replaced the Meaburn spectrograph, which was decommissioned in March 2009. Fig. 3.7 shows a schematic diagram of FRODOSpec. As seen from the diagram, the IFU input head is made up of optical

fibres/lenslets (144 fibres) arranged in a two dimensional matrix (12 by 12); these fibres are then rearranged to form a pseudo-slit where light can pass through. Each of the lenslets have a size 0.82 arcsec by 0.82 arcsec on sky field of view, thus the IFU covers a total field of view of $\sim$10 arcsec $\times$ 10 arcsec at the telescope focal plane (Barnsley et al. 2012). A dichroic beam-splitter allows light to be divided into red and blue regions of the spectrum. Light in each of the arms will then pass through collimator, then dispersed before being focused onto CCDs. The red and blue arms each contain two dispersive elements, giving options for high resolution and low resolution spectroscopy: transmissive diffraction and Volume Phase Holographic (VPH) gratings, respectively. With the different resolutions of the dispersive elements, different wavelength ranges are covered by each. The red VPH has a resolving power of 5300 (dispersion of 0.8 Å/px) and covers a wavelength range of 5900 - 8000 Å, while the blue VPH has a resolving power of 5500 (dispersion 0.35 Å/px) and covers a wavelength of 3900 - 5100 Å. The red grating has a resolving power of 2200 (dispersion 1.6 Å/px) and covers a wavelength range 5800 - 9400 Åand the blue grating has resolving power 2600 (0.8 Å/px) and covers wavelength range 3900 - 5700 Å (Morales-Rueda et al. 2004, Barnsley et al. 2012). When configured to low resolution on both the optical arms (i.e to the diffraction grating), coverage of the whole spectrum can be achieved ($\lambda\lambda$3900 - 9400 Å) in a single observation. The central wavelengths of the high resolution settings (VPH) are fixed, focused on the objects in study (the wavelength region of interest).

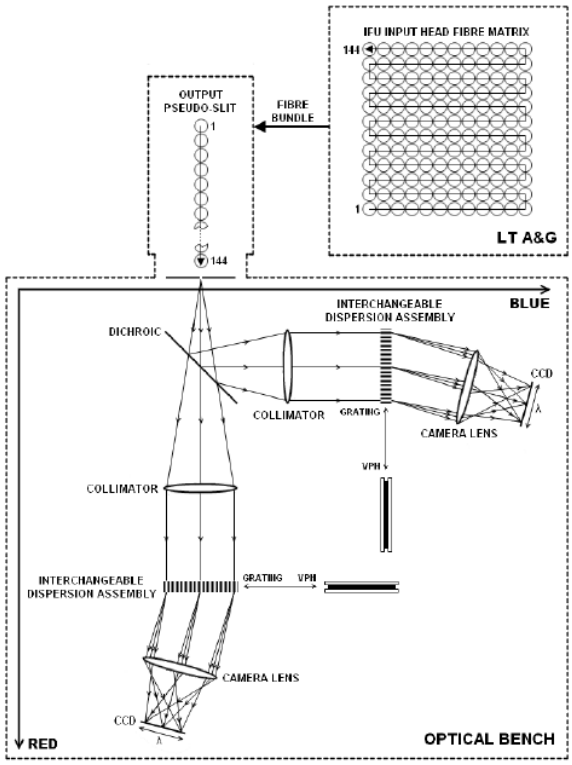

Figure 3.7: Schematic diagram of FRODOSpec. Credit: Barnsley et al. (2012).

A fully autonomous pipeline to reduce raw data obtained with FRODOSpec has been developed and the output data contains multiple extensions, with each extension containing information based on the stage of the reduction process. The data in our monitoring programme was taken with the blue and red VPH. Table 3.2 gives a summary of observations performed with the FRODOSpec onboard LT. The EW(H_α) and peak separation (ΔV) of the data are tabulated in Appendix A.

Table 3.2: Observation summary with the LT.

Target	Observation dates (DD/MM/YY)	Exp. time(s)	Wavelength range(Å)	Central Resolution(Å)	Dispersion(Å/ px)
A 0535+262	01/12/2009 - 25/02/2013	200 - 300	5900 - 8000	1.3	∼0.6
4U 0115+63	24/01/2010 - 20/09/2013	600	5900 - 8000	1.3	∼0.6
V 0332+53	26/12/2009 - 23/02/2013	600	5900 - 8000	1.3	∼0.6
EXO 2030+375	25/03/2011 - 21/07/2013	600	5900 - 8000	1.3	∼0.6

FRODOSpec data undergoes two pipelines: L1 and L2. Bias subtraction, overscan trimming and CCD flat fielding are performed in L1 reduction*. The data reduction process of FRODOSpec data performed with the L2 pipeline is explained in Barnsley, Smith & Steele (2012), but an overview is given below:

The first task of the pipeline is to create a tramline map†, which is done to match-up the CCD pixel coordinates with the position of the fibre profiles along the dispersion axis (see Fig. 3.8 for the coordinate system). A tramline map is a path created to define the propagation of flux from each fibre along the axes of the CCD. The spatial profile of the fibres are modelled with Gaussians. The full width at half maximum (FWHM) of the Gaussian is used to quantify the spatial profile (Fig. 3.9). Another quantity used is the distance between adjacent fibres, δ.

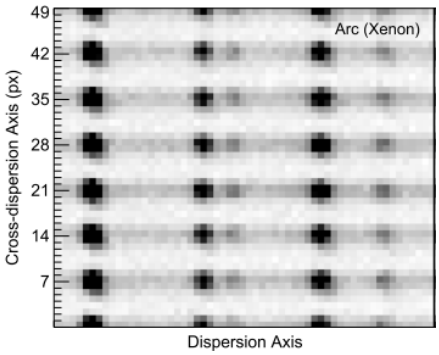

Figure 3.8: Fibre profiles of a Xenon arc frame of an exposure taken with FRODOSpec. Credit: Barnsley, Smith & Steele (2012).

The next task of the pipeline is to extract flux. The aperture extraction technique used by the pipeline reduces the effects of fibre cross-talk (which occurs when fibres overlap spatially) and maximises flux recovered from the fibre profile. Extraction of flux is performed for each fibre using the tramline map created.
Arc fitting is then performed by identifying lines in the arc spectrum of the data in use against a reference arc list for which the pixel position relative to wavelength is known. This is done after zero point shifts are corrected for by cross-correlation of spectra in the arc Row Stacked Spectra (RSS). The shifts are a result of optical distortion, as well as slight erroneous positioning of the fibres in the slit (Fig. 3.10). A throughput correction

*http://telescope.livjm.ac.uk/Info/TelInst/Inst/FRODOspec/#pipeline
†A path that describes the propagation of flux from each fibre along the axes of the CCD.

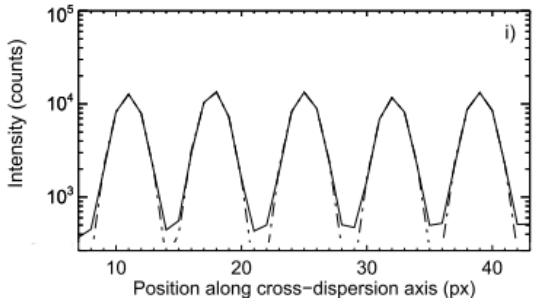

Figure 3.9: Gaussian models used to represent the spatial fibre profiles. The solid line represents the data and the dashed line is the Gaussian model. Credit: Barnsley, Smith & Steele (2012).

is then done to account for the throughput variations within the fibres as a result of fibre defects and misalignments, as well as fibre-to-fibre attenuation variations.

Sky subtraction is then applied to the spectra. The sky flux is taken separately to

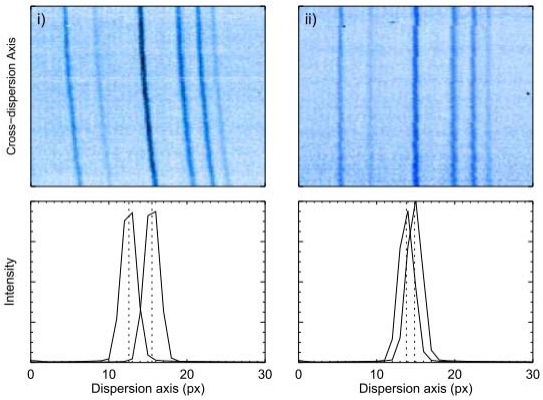

Figure 3.10: Demonstration of gross spectral curvature of spectra in the arc RSS frame (top panel) as a result of zero point shifts (column (i)) The difference in the peaks in the arc RSS frame along the dispersion axis is shown in the bottom panel. Column (ii) shows the effect of cross-correlation to reduce the maximum difference in the peaks. Credit: Barnsley, Smith & Steele (2012).

account for the small field of the view of the FRODOSpec IFU. The median sky flux at each wavelength is then subtracted from the object spectra. Fig. 3.11 shows an example of a flux and wavelength calibrated spectrum obtained with FRODOSpec.

The full details of the computation of the L2 FRODOSpec pipeline are explained in Barnsley, Smith & Steele (2012).

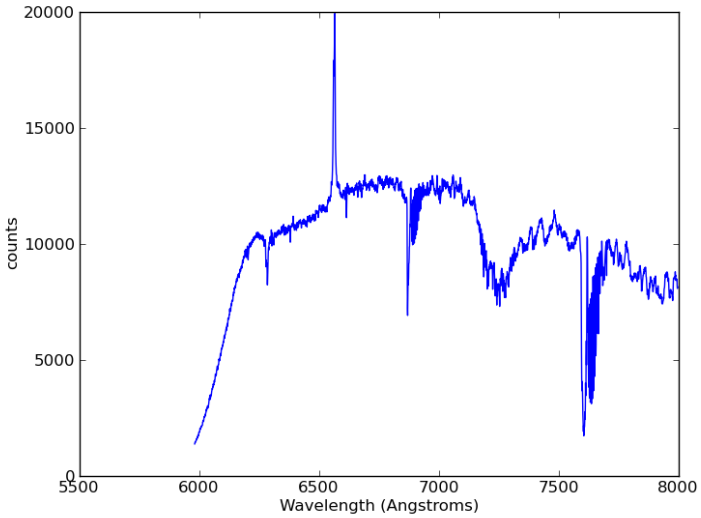

Figure 3.11: An example of the result of the L2 pipeline showing a wavelength calibrated spectrum of A 0535+262 obtained with FRODOSpec.

The mean signal-to-noise (S/N) achieved with SALT is in general better than that obtained with LT. An example S/N for A 1118-616 of ∼120 is higher than that of the sources observed with LT: ∼90 for A 0535+262, ∼20 for V 0332+53, ∼80 for EXO 2030+375 and ∼20 for 4U0115+63.

3.3 Archival Spectra

The archival spectra come from published data which were obtained with telescopes: 1.0-m Jacobus Kapteyn Telescope (La Palma), 2.5-m Isaac Newton Telescope (La Palma), 1.3-m Skinakas Telescope (Crete), 4.2-m William Herschell Telescope (La Palma), South African Astronomical Observatory 1.9m telescope (South Africa) - this will be referred to as *Programme 1* hereafter. The data are listed in Appendix A with the EW(H_α) and ΔV measurements.

Chapter 4

Results, Analysis and Discussion I: Galactic BeXBs

This chapter is divided into two sections. The first gives an overview of the method of disc radius calculations, and in the second section the method is applied to the individual Galactic BeXBs and a discussion of the results is given.

4.1 Method of radius calculation

Huang (1972) demonstrated that the size of the H_α emitting region of the circumstellar disc can be estimated by using the peak separation, ΔV, of the double peaked H_α emission lines if Keplerian velocity distribution of matter in the disc is assumed (Fig. 4.1). Assuming H_α emission extends to the outermost regions of the disc, the Doppler shifted peaks of the double peaked line represent the line of sight region of the outer part of the disc, as illustrated in Fig. 4.1. The peak separation of the double peaked Hα emission line is given by $\Delta V = 2v_{pv}$, where v_{pv} is the projected velocity at the outer edge of the H_α emitting part of the disc. Taking into consideration the geometry of the disc with respect to our line of sight, the true velocity of the disc is then given by $v_{tr} = v_{pv}/\sin i$, where i is the inclination of the disc. The true velocity of the disc can therefore be expressed by $v_{tr} = \Delta V/2 \sin i$. An emitting particle in a circular orbit around the disc at a distance R from the center will have a period:

$$P = \frac{2\pi R}{v_{tr}} \tag{4.1}$$

Assuming Keplerian rotation of the disc:

$$P^2 = \frac{4\pi^2 R^3}{GM} \tag{4.2}$$

Squaring equation (4.1) and equating it to equation (4.2):

$$\frac{4\pi^2 R^3}{GM} = \frac{4\pi^2 R^2}{v_{tr}^2} \tag{4.3}$$

rearranging and solving for R:

$$R = \frac{GM}{v_{tr}^2} \tag{4.4}$$

Substituting $v_{tr} = \Delta V/2 \sin i$ into this:

$$R = \frac{GM \sin^2 i}{(0.5\Delta V)^2}, \tag{4.5}$$

where:

G - gravitational constant

M - mass of the optical companion to the neutron star.

Equation (4.5) was used in this work to obtain estimates of the disc size, with values of the mass, M, of the Be star and the inclination of the disc, i, obtained from literature (see Table 4.1) for the different systems. The peak separation, ΔV, was obtained from fitting Gaussian profiles to the H_α emission lines (see equations 4.6 and 4.7, and Fig. 4.2).

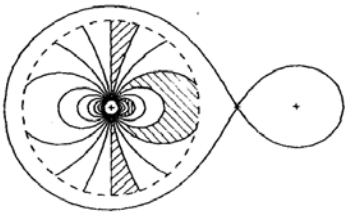

(a) Illustration of a Keplerian disc with shaded regions representing different velocities projected onto the line of sight (with the observer viewing the disc from the bottom of the diagram).

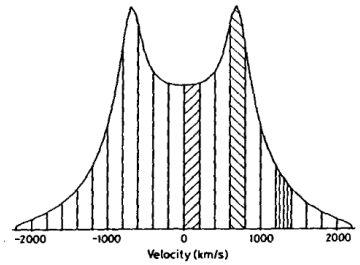

(b) The resulting double-peaked H_α emission line plotted in the stellar rest frame velocity scale. The different shaded regions correspond to the matching regions in the disc in (a).

Figure 4.1: Credit: Horne & Marsh (1986)

The task *splot* in the IRAF package *onedspec* was used to display and analyse the one dimensional reduced spectra. *Splot* offers a number of interactive tools used for the analysis of different properties of absorption and emission lines. To obtain the line centre and equivalent width, the H_α emission lines were fitted with Gaussian profiles (Fig. 4.2).

The peak separation (in km/s) can then be calculated using the expression:

$$\Delta V = c\frac{\lambda_r - \lambda_b}{\lambda_0}, \tag{4.6}$$

where:
λ_b - blueshifted wavelength
λ_r - redshifted wavelength
λ_0 - rest wavelength of the H_α line
c - speed of light

For H_α emission lines which display single peak profiles, ΔV can't be measured directly. However, using a sample of measurements of the brightest Be stars, Hanuschik (1989) demonstrated empirically that there exists a linear relationship between the peak separation and the equivalent width of the H_α emission line ($EW(H_\alpha)$), where he derived the law:

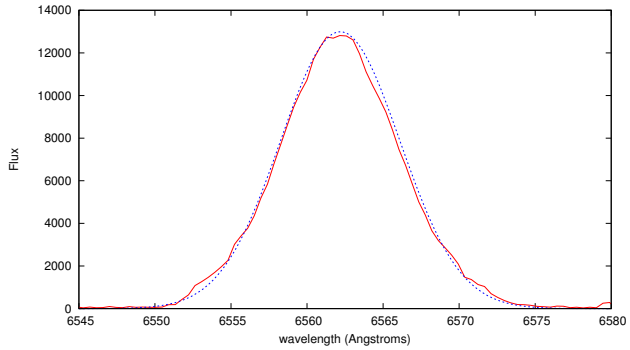

(a) Single peak H_α emission line of A1118-617. The red solid line is the emission line and the blue dashed line is the Gaussian fit.

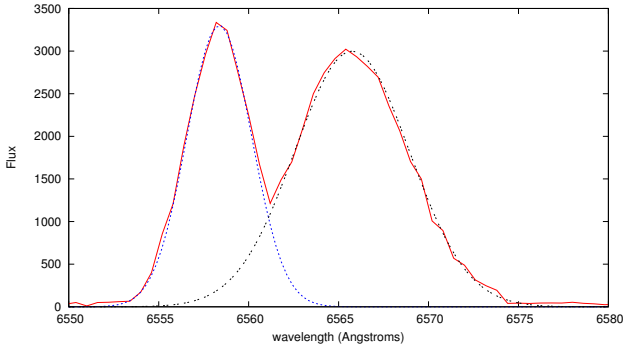

(b) Double peak H_α emission line of A 0535+262. The red solid line is the emission line; the blue and black dashed lines are the Gaussian fits to the blue and red shifted peaks, respectively.

Figure 4.2: Gaussian fits to the H_α emission lines

$$\log(\frac{\Delta V}{2v\sin i}) = -a\log(\frac{-EW}{\text{Å}}) + b, \tag{4.7}$$

where:

ΔV - peak separation in km.s^{-1}

$v\sin i$ - projected rotational velocity of the Be star in km.s^{-1}

EW - H_α equivalent width in Å

The equivalent width (EW) of an emission (or absorption) line measures the strength of the line and is defined as the width of a rectangle at the continuum level that is equal

in area to the spectral line (Carroll & Ostlie 2006; Fig. 4.3):

$$EW = \int \frac{F_c - F_\lambda}{F_c} d\lambda, \tag{4.8}$$

where F_c and F_λ are the continuum flux and flux across the line profile at wavelength λ, respectively.

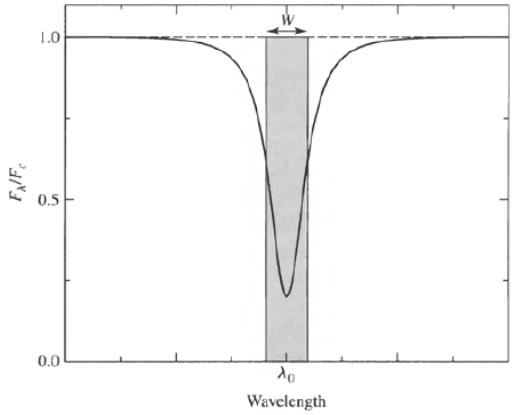

Figure 4.3: Illustration of the equivalent width (W) measurement of an absorption line. Credit: Carroll & Ostlie 2006.

In our sample of BeXBs, the systems with a significant number of double peaked profiles of the H_α emission lines are A 0535+262, 4U 0115+634 and V 0332+53 (a selection of H_α line profiles are presented in Appendix B). The peak separations, ΔV, and $EW(H_\alpha)$ of these were used to derive the parameters a and b. Fig. 4.4 shows the plot of $\log(\frac{\Delta V}{2v \sin i})$ vs. $\log(\frac{-EW}{\text{Å}})$ with a least squares linear fit applied to the data. The least squares method was used instead of a chi-square fit since the size of the errors in $\log(\frac{\Delta V}{2v \sin i})$ are determined by the errors in ΔV (which in turn depends on the errors in λ_r and λ_b). These errors are roughly constant, as the errors in λ_r and λ_b are approximately equal from the Gaussian fits of the H_α emission line. Similarly, the errors in $\log(\frac{-EW}{\text{Å}})$ are also roughly constant (errors in individual EW(H_α) measurements differ by no more than $\sim$10 %). Thus the fit to the data will not be heavily influenced by the weighting of the individual points, but rather largely by the distribution of the points. The a and b parameters were also derived using data of the individual systems (Fig. 4.5). In deriving the parameters, the shell profiles were not used since the deep central depressions in these profiles increase the numerical value of the $EW(H_\alpha)$, and in some cases give a positive

$EW(\mathrm{H}_\alpha)$ (in cases when the circumstellar disc is highly inclined in our line of sight) which may not necessarily reflect on the size of the disc.

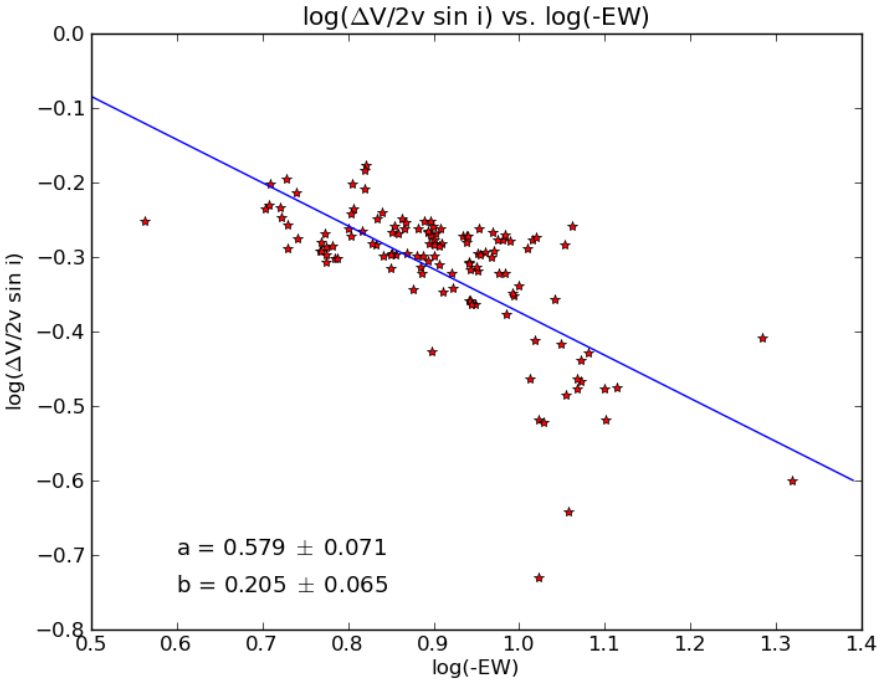

Figure 4.4: $\log(\frac{\Delta V}{2v \sin i})$ vs. $log(\frac{-EW}{\text{Å}})$ from averaging the data of A 0535+262, 4U 0115+634 and V 0332+53 with the best fit linear function overplotted. The best fit parameters, a and b, are displayed.

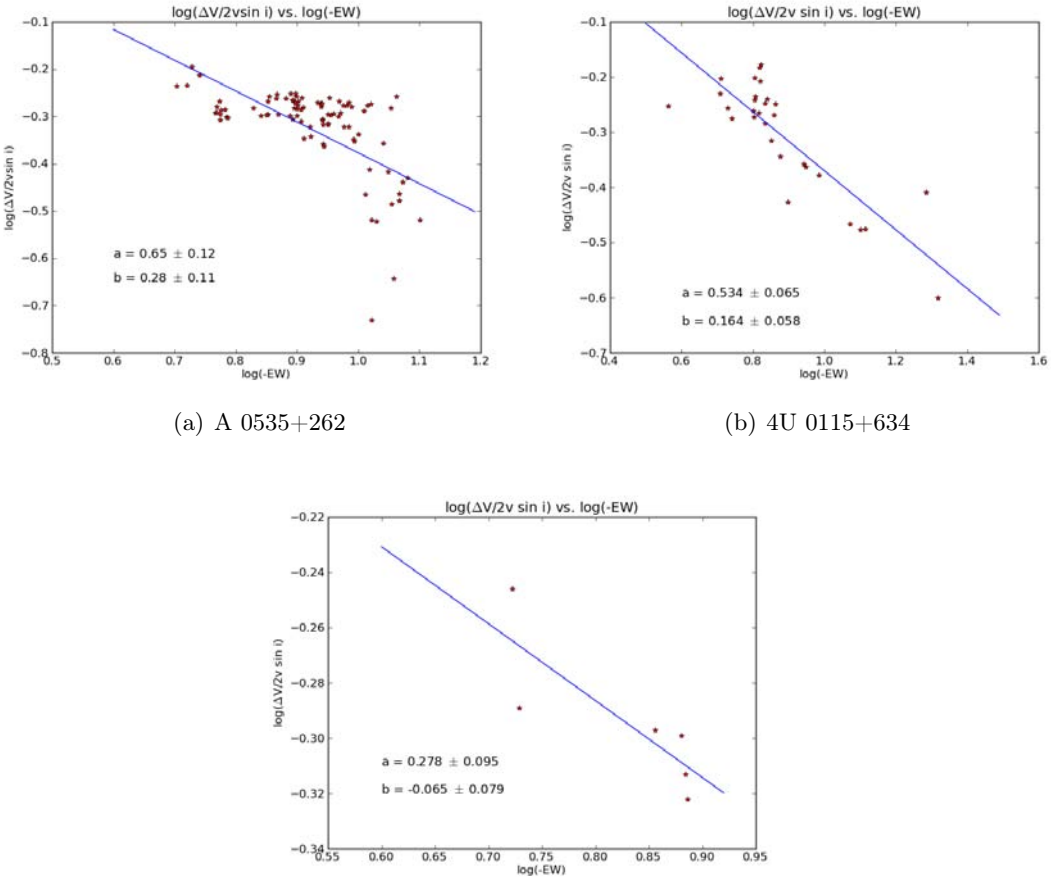

(a) A 0535+262

(b) 4U 0115+634

(c) V 0332+53

Figure 4.5: $\log(\frac{\Delta V}{2v \sin i})$ vs. $\log(\frac{-EW}{\text{Å}})$ from the individual systems with the best fit linear functions overplotted. The best fit parameters, a and b, are displayed.

The a and b parameters obtained from the average data agree within errors with those obtained from the A0535+262 and 4U0115+634 data. The parameters from the fit to the V0332+53 data are smaller which is due to the significantly fewer data points used in this system. The x and y-range covered by the system is narrower, resulting in a large error in the y-intercept of the linear fit.

The uncertainties in the radius estimates were propagated from the uncertainties in ΔV and $EW(H_\alpha)$. The uncertainty in ΔV obtained from direct measurements (i.e. double peaked H_α lines) was propagated from uncertainties in the red and blue wavelengths (λ_r and λ_b, respectively) obtained from Gaussian fitting. An example of a radius calcu-

lation for A 0535+262 of $r = 5.6 \times 10^{10}$m for an observation performed on 08/01/2013 (MJD56301) with LT with peak separation $\Delta V = 1.98 \times 10^5$ m/s gives an uncertainty in the radius of $u(r) = 7.3 \times 10^9$m. This is an uncertainty of $\sim 13\%$, which is typical of the radius estimates obtained from double peaked H_α lines. For single peaked profiles the uncertainty in ΔV was propagated from uncertainties in $v \sin i$, $EW(H_\alpha)$, a and b from the relationship $\log(\frac{\Delta V}{2v \sin i}) = -a \log(\frac{-EW}{\text{Å}}) + b$. Using the parameters obtained for A 0535+262 from the fit of $\log(-EW)$ vs. $\log(\frac{\Delta}{2v \sin i})$ with $EW(H_\alpha) = -7.42$ Å for the observation performed on 23/11/2012 (MJD56255) with LT gives a disc radius $r = 3.3 \times 10^{10}$m, resulting in an uncertainty $u(r) = 2.3 \times 10^{10}$m. This is a larger uncertainty of $\sim$70%, typical of radius estimates obtained from single peaked profiles (see Fig. 4.8(b) for example error bars). The indirect estimates of ΔV (from inference using the relationship between ΔV and EW(H_α)) were checked with the double-peaked H_α profiles and the two methods give radius estimates that agree errors (Fig. 4.6). The measurements of the quantities are tabulated in Appendix A.

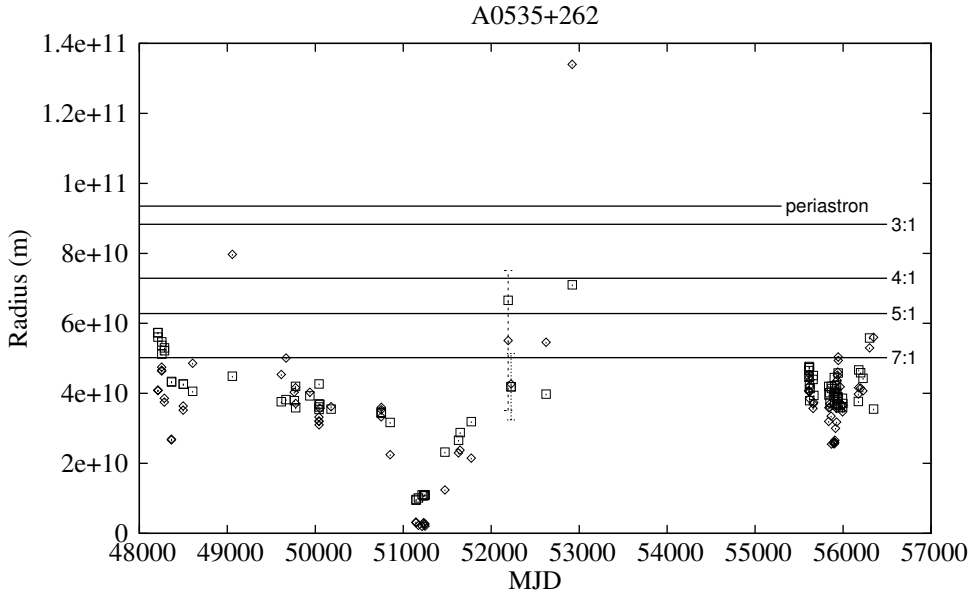

Figure 4.6: A comparison of radius calculations of A 0535+262 obtained from double peaked H_α profiles using direct measurements of ΔV (square symbols) and the indirect method of obtaining ΔV using the relationship between $\log(-EW)$ and $\log(\frac{\Delta}{2v \sin i})$ (diamond symbols). Example errors bars typical of single and double peaked H_α profiles are displayed in the plot. The 3:1 r_{res}, 4:1 r_{res}, 5:1 r_{res}, 7:1 r_{res} and the periastron passage of the NS star are indicated in the plots

4.2 Galactic BeXBs

BeXBs in our programme

EW(H_α)) and peak separation measurements from *Programme 1*, LT and SALT are tabulated in Appendix A. Selected H_α profiles from data obtained with LT and SALT are presented in Appendix B. The systems under study are A 0535+262, 4U 0115+63, V 0332+53, EXO 2030+375 and A 1118-617. Table 3.1 lists the objects in study with the relevant parameters used in this study. The long-term X-ray lightcurves were obtained with the *All-Sky Monitor* (ASM) onboard the *Rossi X-ray Timing Explorer* (RXTE) and *Swift/Burst Alert Telescope* (BAT).

Galactic BeXBs and their parameters.
Legend:*Okazaki & Negueruela 2001, ⋆Negueruela et al. (1999), ◇Negueruela & Okazaki (2001), †Coe et al. (2006), □Janot-Pacheco et al. (1981), ■Hutchings & Crampton (1981), ‡Clark et al. (1998), •Janot-Pacheco et al. (1988), §Motch et al. (1988), ×Reig et al. (1998), ⊞Coe et al. (1987).

Object	$v \sin i$ (km.s^{-1})	M_* ($M_\odot$)	i	$T_{\rm eff}$ (K)
A 0535+262	254‡	20*	27°†	26 000‡
4U 0115+63	365■	18◇	43°◇	26 000◇
V 0332+53	145◇	20*	10.3°◇	25 000⊞
EXO 2030+375	295•	23*	56°*	25 000×
A 1118-617	300□	18§	25°§	34000*

4.2.1 A0535+262

Overview

A0535+26 is one of the best studied X-ray binary transients, discovered by *Ariel* V during a type II outburst (Rosenberg et al. 1975). The system consists of an O9.7IIIe primary star (Steele et al. 1998) and an X-ray pulsar in orbit around the primary. A0535+26 is at a distance $\sim$ 2 kpc (Steele et al. 1998). Orbital measurements of the binary system reveal an orbital period of $\sim$ 111.1 days (Finger et al. 1994; 2006), an eccentricity of $\sim$ 0.47 (Finger et al. 1994) and pulse period of $\sim$ 103.39 s (Caballero et al. 2007).

According to Okazaki & Negueruela (2001)'s viscous decretion disc model, the circumstellar disc is expected to be truncated at the 4:1 resonance radius for $0.11 \leq \alpha \leq$

0.40, and at the 5:1 resonance radius for $0.038 \leq \alpha \leq 0.11$. The 4:1 resonance radius is slightly larger than the mean critical lobe radius at periastron (Fig. 4.7). From the X-ray activity history, it is suggested that $\alpha \geq 0.1$, $T_d \sim \frac{1}{2}T_{\rm eff}$* and that the circumstellar disc is truncated at the 4:1 resonance radius, allowing accretion to occur at periastron passages resulting in regular type I outbursts. Any slight decrease in α (caused by a decrease in the disc temperature) lowers the disc radius to the 5:1 resonance radius (which is less than the mean critical lobe radius at periastron), thus system will be in dormant phase (Okazaki & Negueruela 2001). A0535+262 has, in its long term X-ray lightcurve, shown the three main X-ray states typical of Be/X-ray binaries: quiescence, with $L_{\rm X} \leq 10^{36}$ erg.s^{-1}(Rothschild et al. 2013); type I outbursts with $L_{\rm X} \sim 10^{36-37}$ erg.s^{-1} (Finger et al. 1996); type II outbursts, with $L_{\rm X} > 10^{37}$ erg.s^{-1} (Finger et al. 1996).

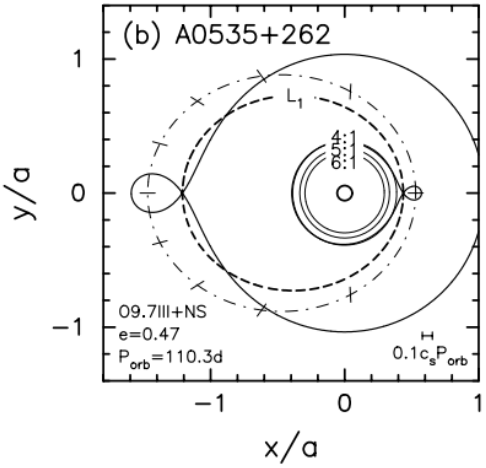

Figure 4.7: Illustration of the orbital model for A0535+262. The Be star is placed at the origin, represented by the small circle. Surrounding the Be star are the 6:1, 5:1 and 4:1 resonance radii. The dash-dotted line represents the orbit of the neutron star (NS) and thick, dashed line represents the position of the first Lagrangian point (L1 point) as the neutron star orbits the Be star. Credit: Okazaki & Negueruela (2001).

Results

For the earliest measurements (Fig. 4.8(b)), at ∼MJD47100, the disc radius sizes have values below the 4:1 resonance radius (r_{res}) ranging from $r \sim 3.8\times10^{10}$m to $r \sim 7\times10^{10}$m

*where $T_{\rm eff}$ is the effective temperature of the Be star.

accompanied with no X-ray outbursts (Fig. 4.9) in this period (Giovannelli & Graziati (1992), Camero-Arranz et al. (2012) archival X-ray lightcurve), the system then goes through a type II outburst at ∼MJD47600 (March 1989), a period when there was no optical coverage of the system. The radius calculations from ∼MJD48200 show disc sizes starting at $r \sim 5.7 \times 10^{10}$m (just below the 7:1 r_{res}) and then show a decreasing trend until ∼MJD48600 ($r \sim 2.3 \times 10^{10}$m). Between MJD48600 and MJD49500 the coverage of A0535+262 is sporadic, with disc radius size ranging from $r \sim 2.5 \times 10^{10}$m to $r \sim 5.9 \times 10^{10}$m. In this period the system underwent a type II outburst which peaked at ∼MJD49400 and lasted for ∼50 days with a peak flux of ∼8 Crab in the energy band 20-50 keV (Bildsten et al. 1997). The disc had reached stability during the outburst (from ∼MJD49440 to ∼MJD50750) with radius size $r \sim 4 \times 10^{10}$m, indicating truncation probably at the 7:1 r_{res}. The disc size calculations then decline, as A0535+262 went through a disc-loss phase with a minimum at ∼MJD51200 ($r \sim 1.2 \times 10^{10}$m). The disc recovered gradually as the radius measurements increased, reaching values between $r \sim 4 - 6 \times 10^{10}$m and the 4:1 r_{res} (between dates MJD52300 and MJD53500). The X-ray activity covering this period (MJD51000 - MJD54000) exhibited type I outbursts at ∼MJD51400, ∼MJD51700, ∼MJD52100, ∼MJD52400 and ∼MJD52700 (separated by ∼300 days, not P_{orb}). A0535+262 underwent a giant Type II outburst at ∼MJD53500 (May/June 2005), reaching fluxes of ∼4.5 Crab at 30 keV observed with the Reuven Ramaty High Energy Solar Spectroscopic Imager (RHESSI) (Smith et al. 2005). This epoch was studied by Coe et al. (2006) where they show three sizes of the circumstellar disc at different times: before the 2005 May/June outburst ($r = 6.8 \times 10^{10}$m, disc *b*), after the outburst ($r = 10.7 \times 10^{10}$m, disc *c*) and a while before the outburst event, between 2001 December (∼MJD52240) and 2003 December (∼MJD52980; $r = 4.8 \times 10^{10}$m, disc *a*) (see Fig. 4.10). The processes leading to the May/June 2005 outburst were compared to those which were responsible for the 1994 outburst which was investigated by Haigh et al. (2004). Haigh et al. (2004) demonstrated that the NS accreted matter in the disc leading to the 1994 giant outburst, resulting in the disc decreasing in size from the 5:1 r_{res} to the 6:1 r_{res}. This series of events was not seen to take place in the resulting type II outburst of May/June 2005, as demonstrated by Coe et al. (2006). Haigh et al. also demonstrated that there exists a cyclical trend by the circumstellar disc on a timescale of ∼1500 days in their plot of m_K vs. EW(H_α). The disc in this cycle goes from one state (low disc state) and remains there for a certain period to another (high disc state) - which shows evidence of disc truncation at these two states (Fig. 4.11).

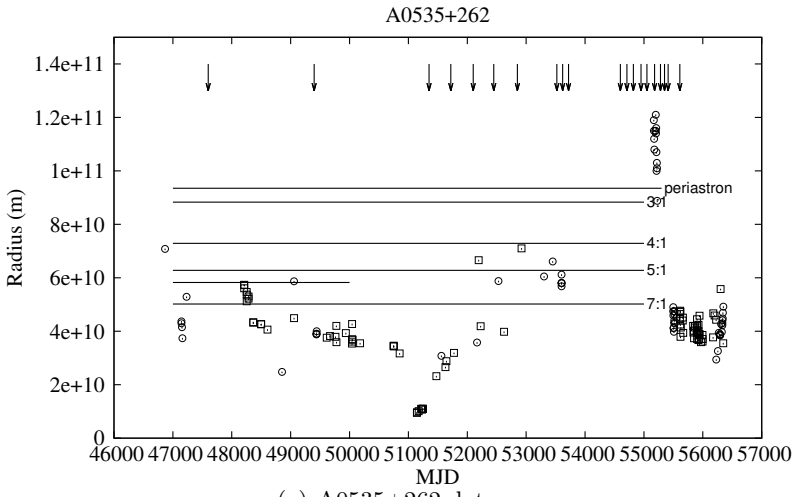

(a) A0535+262 data.

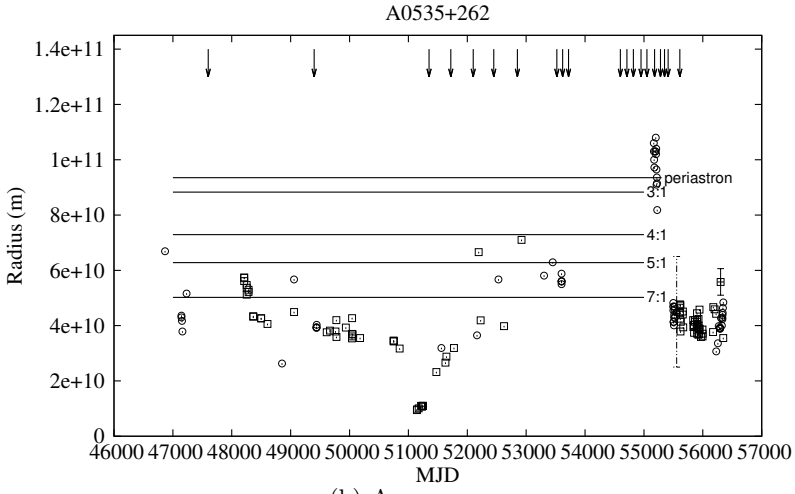

(b) Average.

Figure 4.8: H_α radius versus MJD; (a) includes the radius calculations from a and b parameters obtained using A 0535+262 data alone for the single peak H_α emission profiles, while (b) includes those from a and b parameters obtained using the averaging of the combined data (A 0535+262, 4U 0115+634 and V 0332+53). The 3:1 r_{res}, 4:1 r_{res}, 5:1 r_{res}, 7:1 r_{res} and the periastron passage of the NS star are indicated in the plots. The square symbols indicate the radius calculations from double-peaked profiles of H_α and circles represent single-peaked profiles. Example errors bars are shown typical for single peaked (broken line) and double peaked (solid line) profile radius calculations. The arrows represent peak times of X-ray outbursts.

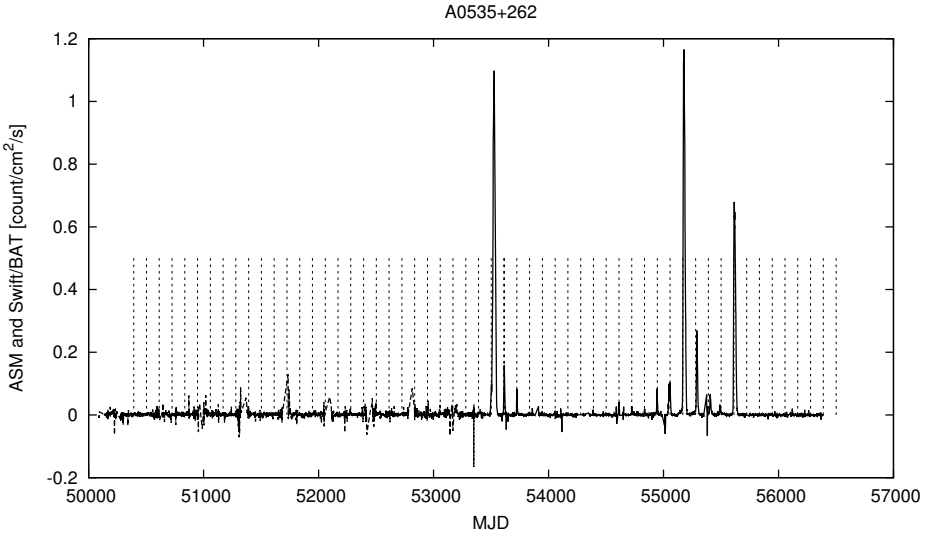

Figure 4.9: Long-term ASM (dashed lined) and Swift/BAT (solid line) X-ray light curve of A0535+262. The ASM count rates have been scaled down by a factor of 80 to account for the different energy bands of the two instruments, just so that the combined light curve look good by eye. The vertical lines indicate the times of periastron passage of the NS according to the ephemeris from Finger et al. (1996).

Grundstrom et al. (2007) did a joint H_α and X-ray study of A0535+262. They calculated the disc radius based on the numerical model presented by Grundstrom & Gies (2006) where it is demonstrated that there exist monotonic relationships between the EW(H_α) and the ratio of the angular half-width at half-maximum (HWHM) of the projected disc major axis to the stellar radius. The two quantities are represented by the relationship:

$$\frac{R_d}{R_s} = \sqrt{\frac{I_\lambda^s}{I_\lambda^d} \frac{W_\lambda(1+\epsilon)}{<\Delta\lambda>\cos i}}$$

where:

$\frac{I_\lambda^s}{I_\lambda^d}$ is the ratio of the stellar to disc specific intensity (which is temperature dependent).

$<\Delta\lambda>$ is the wavelength interval over which the line is optically thick (averaged over the visible disc).

ϵ is the ratio of the disc continuum flux to stellar flux in the H_α region.

W_λ is the H_α equivalent width.

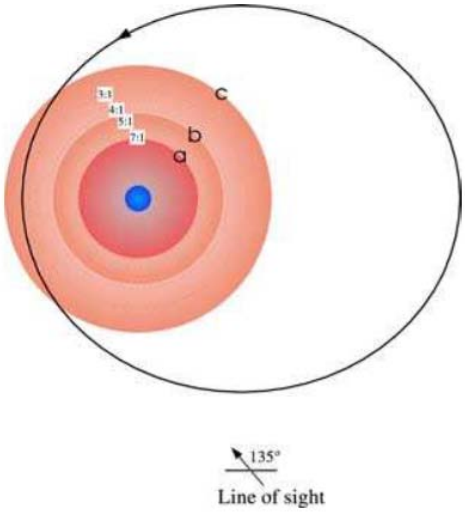

Figure 4.10: Illustration of the circumstellar disc size of A0535+262 in comparison with the orbit of the NS (black line). The 3:1, 4:1, 5:1 and 7:1 resonance radii are shown along with the disc sizes labelled a ($r = 4.8 \times 10^{10}$m), b ($r = 6.8 \times 10^{10}$m) and c ($r = 10.7 \times 10^{10}$m). Credit: Coe et al. (2006).

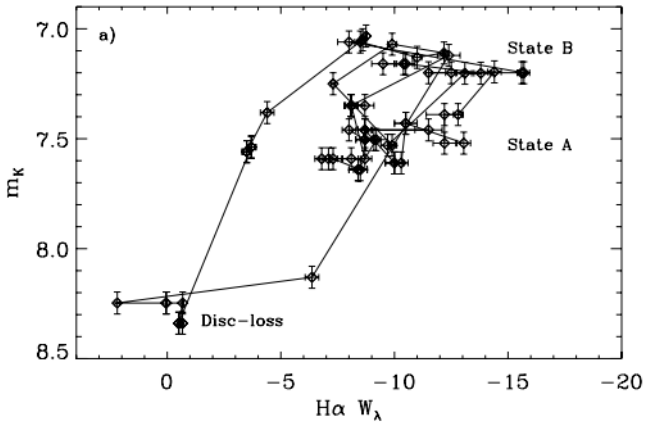

Figure 4.11: m_K vs. EW(H_α) plot demonstrating the ∼1500 day cyclical behaviour of A 0535+262. The direction of the loop as the disc changes states is clockwise. Credit: Haigh et al. (2004).

Fig. 4.12 shows a plot of Hα radius as a function of time with radius values from Grundstrom et al. (2007) and Coe et al. (2006) included for comparison. The results from the method used by Grundstrom et al. (2007) are in agreement with our results for the period MJD50000 - MJD51000, although the minimum at ∼MJD51100 (during

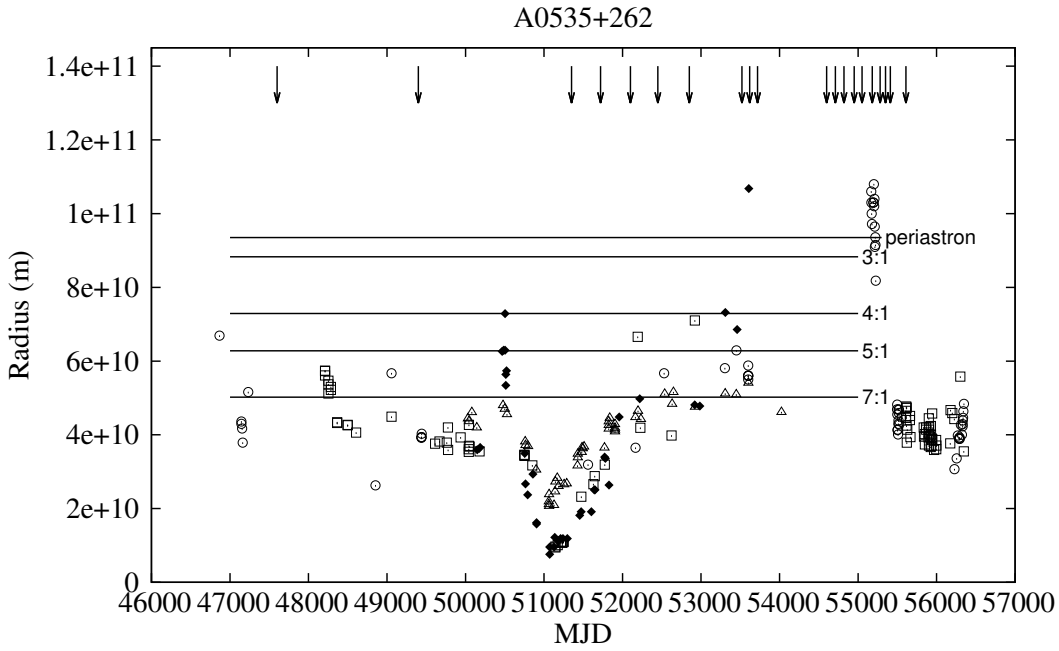

Figure 4.12: H_α radius as a function of time with values from Grundstrom et al. (2007) and Coe et al. (2006) included (triangle and diamond symbols, respectively) for comparison.

the disc-loss phase) from our results show disc sizes that are approximately half of those presented by Grundstrom et al. (2007). The other discrepancy in the two data sets is seen in the period MJD52000-MJD54000 (after the disc recovery phase): our radius calculations show disc growth up to the 4:1 r_{res} (at MJD52921), with the disc declining back to the 5:1 r_{res} whereas radius calculations from Grundstrom et al. show disc stability at $R_d/R_s \sim 5$, suggesting truncation at probably the 6:1 r_{res}. The method of our radius calculations is the same as that used by Coe et al. (2006).

Approximately one orbital period after the May/June 2005 type II outburst the system underwent two type I outbursts close to periastron passage of the NS at ∼MJD53600 and ∼MJD53800 which were observed with the *INTErnational Gamma-Ray Astrophysics Laboratory* (INTEGRAL) and RXTE. The two normal outbursts were at luminosity levels $L \sim 0.9 \times 10^{37}$erg.s^{-1} during the peak at the energy range 3-50 keV (Caballero et al. 2007). A closer look at the first of the two type I outbursts reveals a flare at the outburst rise.

The Be disc of A0535+262 was most likely still undergoing growth following the end

of *Programme 1* in 2005, as the system began to undergo X-ray activity starting from ∼MJD54610 with a series of type I outbursts. The fourth of these is unusual in that it is double-peaked, with the first peak occurring a few days (∼14 days) before the periastron passage of the NS and the second peak occurs around periastron passage, at ∼MJD55058 (Fig. 4.13 (a)). The flux at the peak of both outbursts reached 440 mCrab at energy band 15-50 keV (Caballero et al. 2010, 2013). The monitoring of A0535+262 with LT commenced shortly after the double-peaked outburst, at the end of August 2009 (∼MJD55072). The H_α radius calculations from observations taken at the beginning of the LT monitoring campaign display sizes larger than the periastron passage of the NS, ranging from $r \sim 1.1 \times 10^{11}$m at MJD55168, which decline to below the 7:1 r_{res} on a timescale of ∼330 days. A0535+262 was active in the X-ray wavelengths around the time when the LT monitoring programme started. The system underwent a giant type II outburst which peaked at ∼MJD55180 with a peak flux of ∼5.14 Crab in the 15-50 keV energy range (Caballero et al. 2010). Approximately an orbital period later A0535+262 underwent another outburst which reached a flux of ∼1 Crab at energy range 15-50 keV (Caballero et al. 2010). Following that, in the next periastron passage of the NS (∼MJD55390), the system displayed more peculiar X-ray behaviour, as it underwent another double-peaked type I outburst (Fig. 4.13 (b)). The difference, however, between this (∼MJD55390) and the August 2009 (∼MJD55050) double-peaked outburst is that the first peak of the ∼MJD55390 outburst is smaller in intensity than the main peak and the peaks are almost completely separated. A0535+262 displayed two further outbursts associated with the periastron passage of the NS: a type I outburst at ∼MJD55480 and a giant outburst peaking at ∼MJD55620. The system has been in quiescence since. The disc radius sizes have since been displaying relatively low values, ranging from $r \sim 3 \times 10^{10}$m to just below the 7:1 r_{res}, indicating truncation at the 7:1 r_{res}.

4.2.2 4U0115+634

Overview

4U0115+63 is another well studied BeXB transient. The system was initially reported as a discovery by the *Uhuru* satellite during its 1971 type II outburst (Giacconi et al. 1972, Forman et al. 1978), however, it was later noticed, after going through the $VELA$ 5B archival data that it had already been detected in 1969 (Whitlock et al. 1989). The opti-

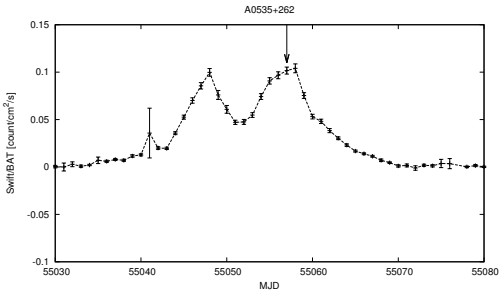

(a) The double-peaked type I outburst of August 2009. The arrow represents the periastron passage of the NS.

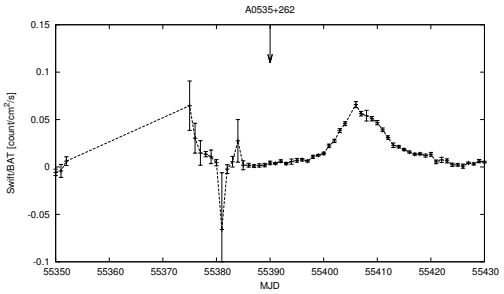

(b) The double-peaked type I outburst of July 2010. The arrow represents the periastron passage of the NS.

Figure 4.13

cal companion in the binary system is a B0.2Ve star at a distance of 7.8 kpc (Negueruela & Okazaki 2001). Using the *Burst and Transient Source Experiment (BATSE)* monitoring data of a sample of accreting pulsars, Bildsten et al. (1997) derived the orbital parameters: P_{orb} = 24.317037(62) days, $a_X sini$ = 140.13(8)lt-s, e = 0.3402(2), T_{peri} = MJD49279.2677(34). The pulse period of the pulsar is 3.614690(2) s (Tamura et al. 1992).

Negueruela & Okazaki (2001), in their viscous decretion disc model, demonstrated that with $\alpha \leq 0.1$ for the disc in 4U0115+634, the isothermal circumstellar disc, with $T_d \sim 0.8\, T_{eff}$ (where $T_{\rm eff}$ is the effective temperature of the star), is most probably truncated at the 4:1 r_{res} and truncation at the 3:1 r_{res} occurs when the viscosity increases (increase in disc temperature), with $\alpha \sim 1$. It is also noted that the 3:1 r_{res} is smaller than the critical lobe radius at periastron passage (Fig. 4.14). As a result of this, the system rarely undergoes type I outbursts since the NS does not accrete enough material at/close to periastron passage (i.e no Roche lobe overflow). 4U0115+634 does, however, exhibit type II outbursts.

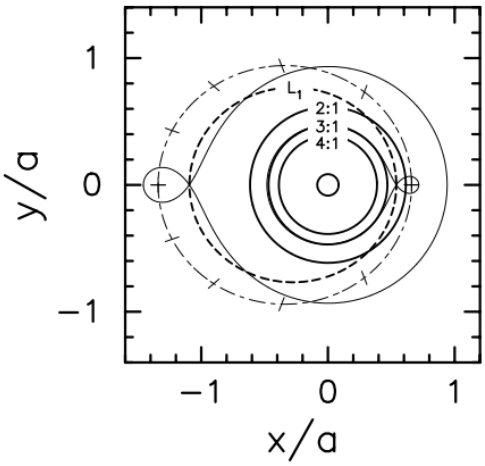

Figure 4.14: Illustration of the orbital model for 4U0115+634. The Be star is placed at the origin, represented by the small circle. Surrounding the Be star are the 6:1, 5:1 and 4:1 resonance radii. The dash-dotted line represents the orbit of the neutron star and thick, dashed line represents the position of the first Lagrangian point (L1 point) as the neutron star orbits the Be star. Credit: Okazaki & Negueruela (2001).

Results

The radius calculations from early observations (∼MJD47900 – ∼MJD50000; Fig. 4.16(b)) have a range of values from $r \sim 1.9\times10^{10}$m to $r \sim 3.8\times10^{10}$m. A large majority of these values are in between the 5:1 and 3:1 r_{res}. During this period, 4U0115+634 underwent an outburst in February 1990 (∼MJD47900) observed with the ASM (Fig. 4.15), reaching a peak flux of 400 mCrab at energy range 1-20 keV (Nagase et al. 1991, Tamura et al. 1992), followed by another type II outburst in March 1991 (∼MJD48320). A large type II outburst was again observed in May/June 1994 (peaking at ∼MJD49500) with a peak flux of ∼55 mCrab at energy range 20-50 keV (Negueruela et al. 1997), followed by another giant outburst in November/December 1995 (peaking at ∼MJD50040) reaching flux levels of ∼0.7 Crab at 3-300 keV (Sazonov & Sunyaev 1995, Boldin et al. 2013). The disc radius size began to rise shortly after that, reaching values larger than periastron passage (up to $r \sim 7.5 \times 10^{10}$m at MJD50096) and declined to $r \sim 2.12 \times 10^{10}$m at MJD50480 (close to the 5:1 r_{res}) on a timescale of ∼385 days.
During the decline of the disc the system underwent a short series of type I outbursts separated by the orbital period (but peaking just after periastron passage of the NS) between MJD50300 and MJD50400 (Fig. 4.17) which were seen to decrease in inten-

sity gradually. Between MJD51050 and MJD52000, 4U0115+634 displayed two type II outbursts at ∼MJD51250 (March 1999) and ∼MJD51800 (August 2000). The optical observations during this period are scattered, with size ranges from the 3:1 r_{res} to $r \sim 6 \times 10^{10}$m leading up to the March 1999 outburst. Approximately one orbit after the August 2000 outburst the disc radius was still relatively large (larger than periastron passage) at $r \sim 5.7 \times 10^{10}$m (MJD51835, just after the outburst ended at ∼MJD51830). Since the end of *Programme 1* and before the commencement of the LT monitoring programme, 4U0115+634 underwent two further type II outbursts at ∼MJD53260 and ∼MJD54560 for which there are no optical spectroscopic coverage.

At the beginning of the LT monitoring of 4U0115+634 in January 2010 (MJD55220), the disc radius sizes were relatively small, with sizes below the 5:1 r_{res} at $r \sim 1.5 \times 10^{10}$m. The disc then grew in size, reaching values larger than periastron passage, peaking at $r \sim 6.5 \times 10^{10}$m (at ∼MJD55800). The system underwent a type II outburst just before the peak of the radius size which peaked at ∼MJD55260 (May/June 2011) reaching a flux of ∼0.8 Crab at energy bands 3-300 keV (Boldin et al. 2013). The disc returned to a low state after that, reaching sizes below the 5:1 r_{res} ($r \sim 2 \times 10^{10}$m) on a timescale of ∼650 days. 4U0115+634 has been in a quiescent state since the end of the May/June 2011 outburst.

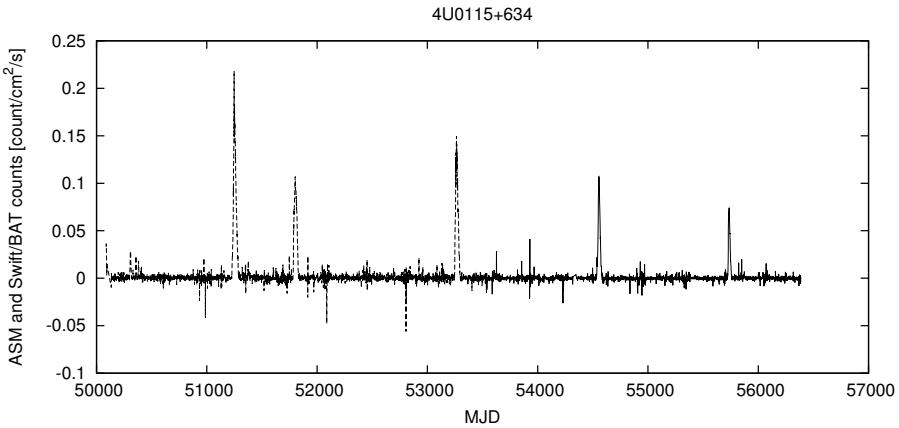

Figure 4.15: Long-term ASM (dashed lined) and Swift/BAT (solid line) X-ray lightcurve of 4U0115+634. The ASM count rates have been scaled by a factor of 140 to account for the different energy bands of the two instruments.

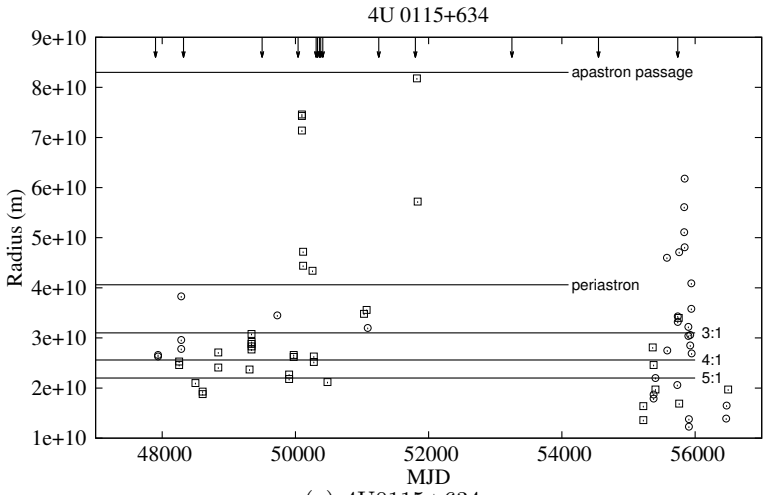

(a) 4U0115+634.

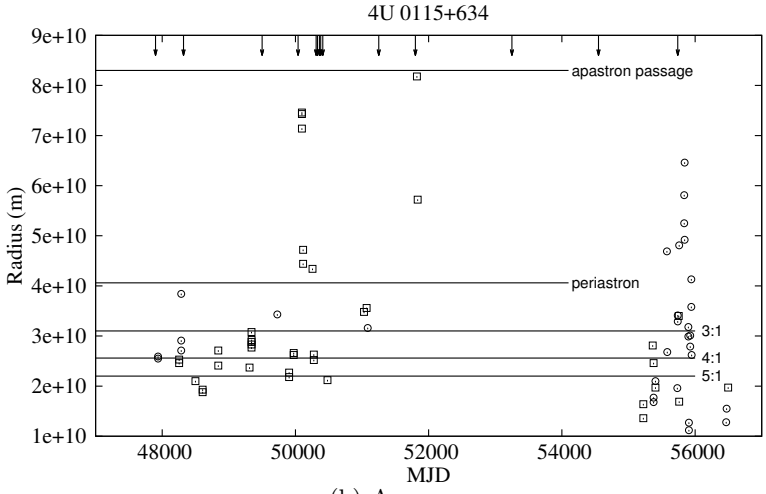

(b) Average.

Figure 4.16: H_α radius versus MJD; (a) includes the radius calculations from a and b parameters obtained using 4U 0115+634 data alone for the single peak H_α emission profiles, while (b) includes those from a and b parameters obtained using the averaging of the combined data (A 0535+262, 4U 0115+634 and V 0332+53). The 3:1 r_{res}, 4:1 r_{res}, 5:1 r_{res}, apastron and periastron passages of the NS star are indicated in the plots. The square symbols indicate the radius calculations from double-peaked profiles of H_α and circles represent single-peaked profiles. The arrows indicate the times of X-ray outbursts.

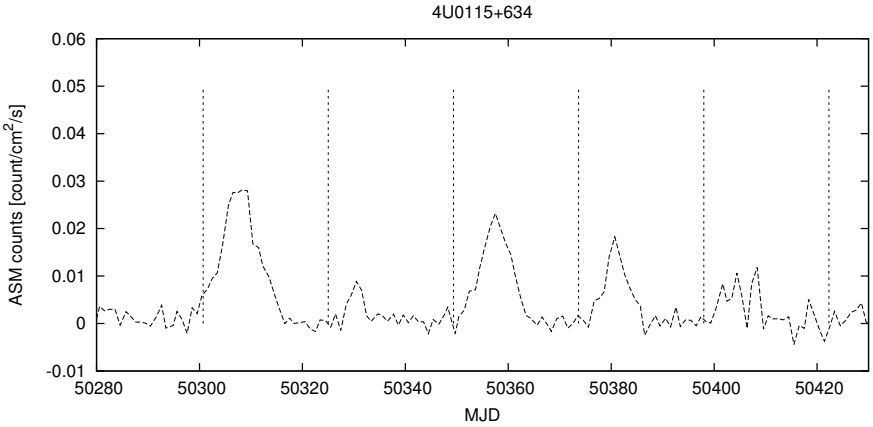

Figure 4.17: ASM X-ray lightcurve of 4U0115+634 in the period when the system underwent a short series of type I outbursts. The vertical lines indicate the times of periastron passage of the NS calculated according to the ephemeris from Bildsten et al. (1997).

4.2.3 V0332+53

Overview

V0332+53 is a transient X-ray pulsar which was discovered by *VELA* 5B during an outburst in 1973 (Terrell & Priedhorsky 1984). The optical companion of the system is an O8-9Ve star, BQ Cam (Negueruela et al. 1999), located at a distance ∼7 kpc. Using data from *RXTE* and *INTEGRAL* observations, Zhang et al. (2005) derived the following orbital parameters: $P_{pulse} \approx 4.375$ s, $P_{orb} = 34.67$ days, $e = 0.37$, $a_X sini \approx 86$ lt-s.

Okazaki & Negueruela (2001) predict truncation at the 3:1 r_{res} for moderate viscosity ($0.099 \leq \alpha \leq 0.60$), adopting $T_d \sim 0.5\, T_{eff}$. At lower values of the viscosity parameter, truncation is expected to occur at the 4:1 r_{res}. As seen in Fig. 4.18, the 3:1 r_{res} is close enough to the critical lobe radius at periastron passage that any slight disturbance of the disc will result in material from the disc being transferred onto the NS.

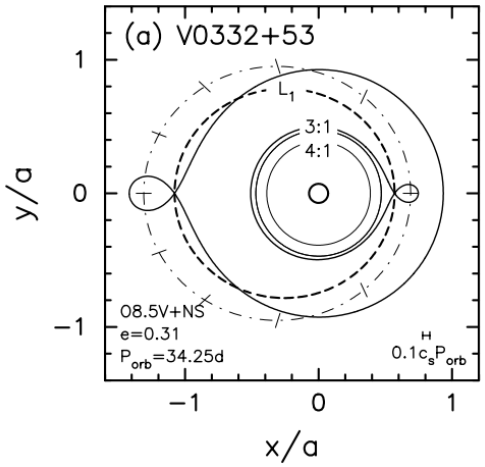

Figure 4.18: Illustration of the orbital model for V0332+53. The Be star is placed at the origin, represented by the small circle. Surrounding the Be star are the 3:1 and 4:1 resonance radii. The dash-dotted line represents the orbit of the neutron star and thick, dashed line represents the position of the first Lagrangian point (L1 point) as the neutron star orbits the Be star. Credit: Okazaki & Negueruela (2001).

Results

In the early observations (beginning of *Programme 1*, Fig. 4.20(b)), starting at ∼MJD48000, the disc size was at a radius just below the 5:1 r_{res} (at $r \sim 2.6 \times 10^{10}$m) and gradually grew in size, reaching a maximum just below the periastron passage of the NS ($r \sim 6 \times 10^{10}$m) on a timescale of ∼330 days. The disc then decreased from $r \sim 6 \times 10^{10}$m to below the 5:1 r_{res} ($r \sim 1.8 \times 10^{10}$m) in ∼690 days. The system underwent a type II outburst prior to the optical coverage in 1989, which reached a peak flux of ∼0.3 Crab at energy range 2-20 keV observed with the ASM in September/October of that year (∼MJD47790 - ∼MJD47800, Makino & GINGA Team (1989), Makishima et al. (1990)). In the period between MJD51700 and MJD52200, we have sparse coverage of the Be disc. At ∼MJD51750 the radius size is just below the 4:1 r_{res} and decreases to $r \sim 1.9 \times 10^{10}$m at ∼MJD52130. During this period V0332+53 was in quiescence.

The LT monitoring of V0332+53 started when the system was undergoing a rare series of type I outbursts in 2009 (∼MJD55160 − ∼MJD55320, Fig. 4.21). The disc radius during this period displayed relatively large values (above the 3:1 r_{res}), from $r \sim 5.6 \times 10^{10}$m which declined to below the 5:1 r_{res} ($r \sim 1.3 \times 10^{10}$m) on a timescale of ∼182 days. V0332+53 has been in quiescence since the end of the 2009 type I outburst

series. The disc size has since remained below the 4:1 r_{res}, with radius values ranging from $r \sim 1.3 \times 10^{10}$m to $r \sim 3.1 \times 10^{10}$m.

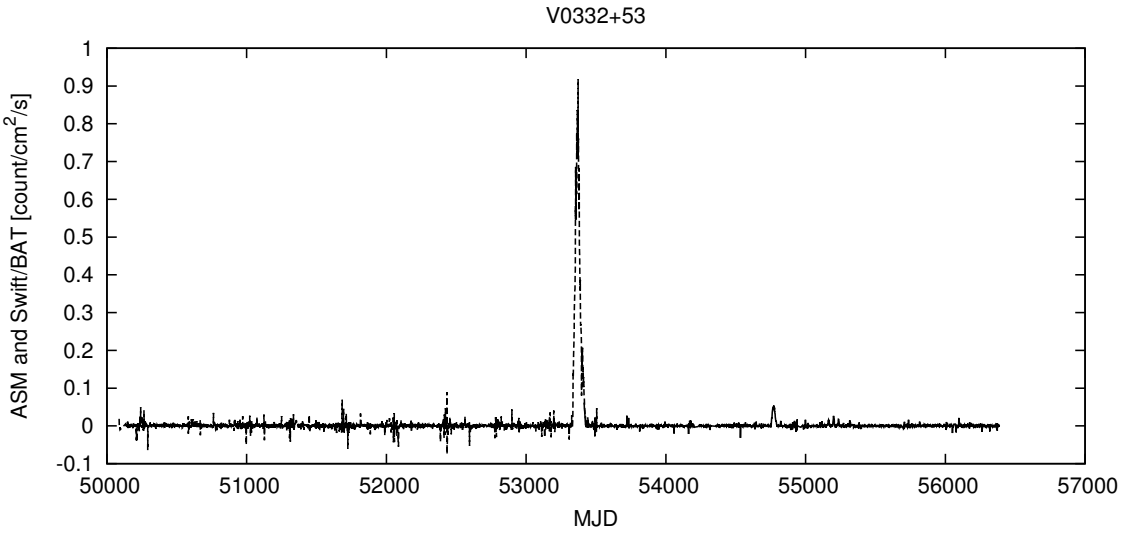

Figure 4.19: Long-term ASM (dashed line) and Swift/BAT (solid line) X-ray lightcurve of V0332+53. The ASM count rates have been scaled by a factor of 90 to account for the different energy bands of the two instruments.

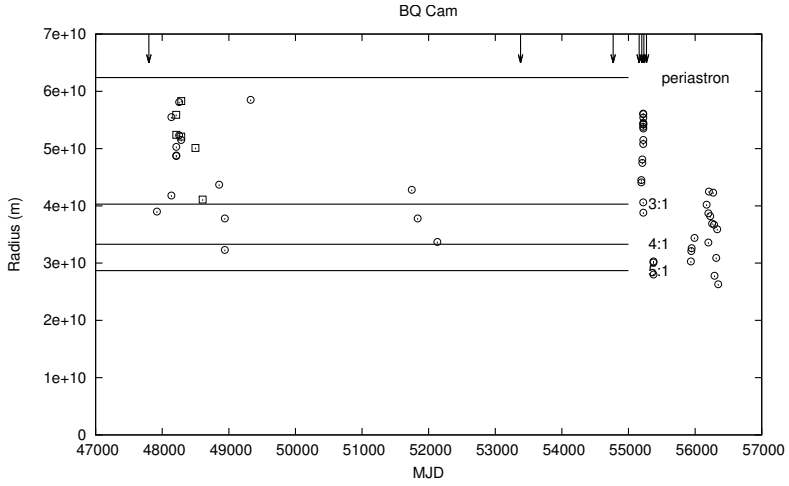

(a) BQ Cam data.

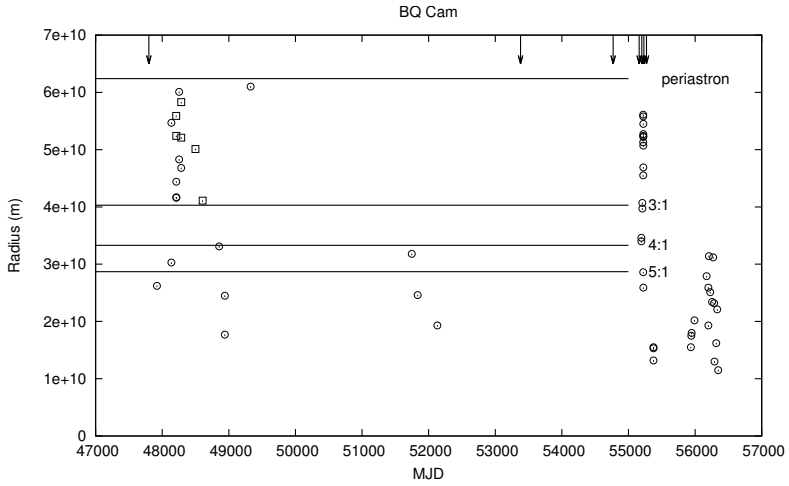

(b) Average.

Figure 4.20: H_α radius versus MJD; (a) includes the radius calculations from a and b parameters obtained using V 0332+53 data alone for the single peak H_α emission profiles, while (b) includes those from a and b parameters obtained using the averaging of the combined data (A 0535+262, 4U 0115+634 and V 0332+53). The 3:1 r_{res}, 4:1 r_{res}, 5:1 r_{res} and the periastron passage of the NS star are indicated in the plots. The square symbols indicate the radius calculations from double-peaked profiles of H_α and circles represent single-peaked profiles. The arrows indicate the times of X-ray outbursts

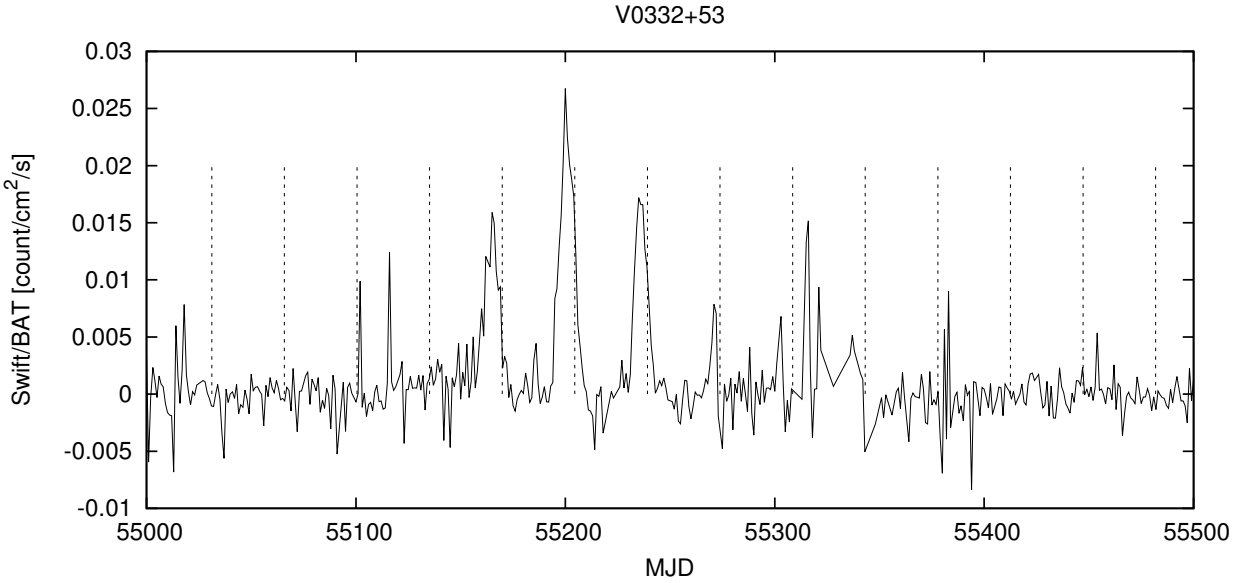

Figure 4.21: The series of type I outbursts observed with Swift/BAT. The vertical lines indicate the times of periastron passage.

4.2.4 EXO2030+375

Overview

EXO 2030+375 is an X-ray transient pulsar which was discovered with the *European X-ray Observatory Satellite* (EXOSAT) during a giant outburst in 1985 (Parmar et al. 1989). The system is located at a distance of 5.3 kpc (Parmar et al. 1989). Optical and IR studies of the system revealed the optical companion to be an early-type main-sequence star (B0Ve), with properties similar to those of V0332+53 (Motch & Janot-Pacheco 1987, Coe et al. 1988). In the analysis of long-term RXTE data, Wilson et al. (2005) obtained orbital parameters: P_{orb} = 46.0202(2) days, e = 0.416(1), $a_X sini$ = 238(2) lt-s, T_{peri} = JD2451099.93(2). The pulse period of the pulsar is 41.4106(1) s (Naik et al. 2013).

Okazaki & Negueruela (2001) show that for viscosities in the range $0.098 \leq \alpha \leq 0.37$, the disc of a B0III or O9III is expected to be truncated at the 4:1 r_{res}. For a lower range of values of the viscosity parameter ($0.03 \leq \alpha \leq 0.098$), truncation is expected at the 5:1 r_{res}. Since there was a large uncertainty in the distance to the optical companion to EXO 2030+375, the possibility of a B0IV star being the primary of the system was considered. The results for the B0IV spectral type are: truncation at the 4:1 r_{res} for $0.12 \leq \alpha \leq 0.44$, and at the 5:1 r_{res} for $0.036 \leq \alpha \leq 0.12$. However the X-ray history of EXO2030+375 (with long series of type I outbursts) favors a B0III or O9III primary with $\alpha \geq 0.1$ and/or $T_d \geq 0.5\, T_{eff}$ and truncation at 4:1 r_{res}, since these earlier spectral types have a larger truncation radius as a result of a higher disc temperature. Fig. 4.22 shows that the 4:1 r_{res} is close to the critical lobe radius at periastron passage.

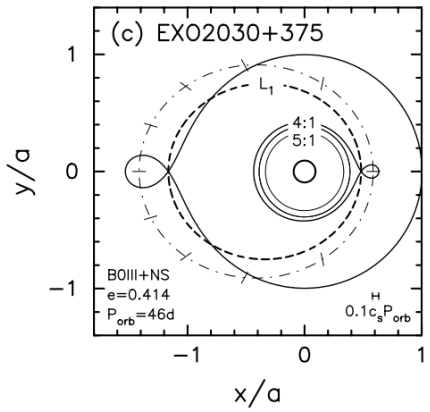

Figure 4.22: Illustration of the orbital model for EXO 2030+375. The Be star is placed at the origin, represented by the small circle. Surrounding the Be star are the 5:1 and 4:1 resonance radii. The dash-dotted line represents the orbit of the neutron star and thick, dashed line represents the position of the first Lagrangian point (L1 point) as the neutron star orbits the Be star. Credit: Okazaki & Negueruela (2001).

Results

The radius calculations of EXO 2030+375 from the earliest observations (MJD48899 − MJD49170) show a range of values of the size of the circumstellar disc, from $r \sim 2.7 \times 10^{10}$m to just below the 3:1 r_{res} at $r \sim 4.7 \times 10^{10}$m (Fig. 4.23). The disc radius had declined to values around $r \sim 1 \times 10^{10}$m. During this period EXO 2030+375 was displaying low intensity type I outbursts (Fig. 4.24).

The LT observations of EXO 2030+375 display larger disc radius sizes (above the 3:1 r_{res}) ranging from $r \sim 6.1 \times 10^{10}$m (close to periastron passage) to $r \sim 7.5 \times 10^{10}$m. The system has been undergoing a long series of type I outbursts associated with the periastron passage of the NS (Fig. 4.24). EXO 2030+375 underwent a rare type II outburst in 2006 which peaked at ∼MJD53950 with luminosity values of $L \sim 1.2 \times 10^{38}$erg s^{-1} in the energy range 1-20 keV. Unfortunately there was no optical coverage of the system directly before, during and after the giant outburst event. Following that, the system displayed type I outbursts of relatively high intensity which gradually decreased to intensities similar to those observed before the giant outburst event (Fig. 4.24).

Only the combined data (4U 0115+634, A 0535+262 & V0332+53) were used to produce the radius plot since EXO 2030+375 does not show any double peaked H_α emission lines in its spectra.

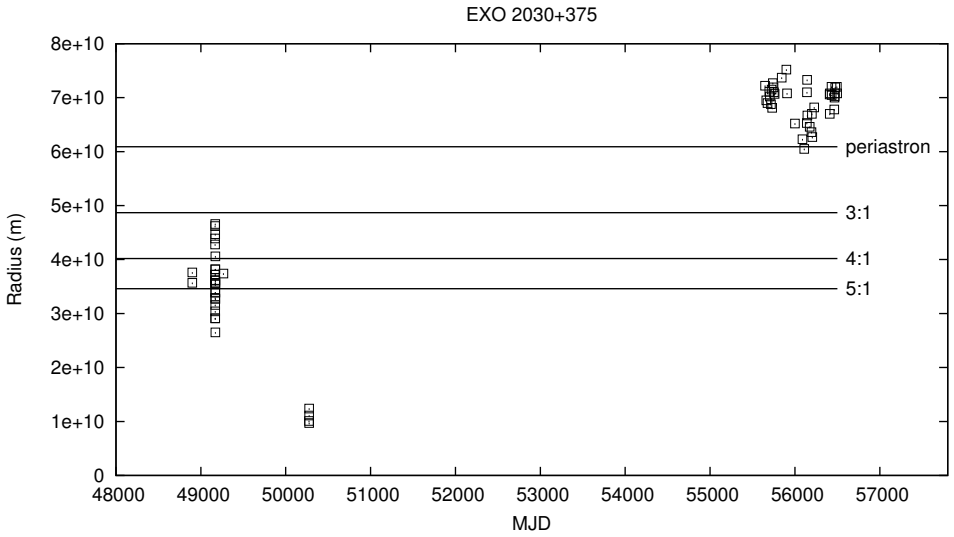

Figure 4.23: H_α radius versus MJD using combined data (A0535, V0332 and 4U0115). The 5:1, 4:1, 3:1 and periastron passage are indicated in the plot.

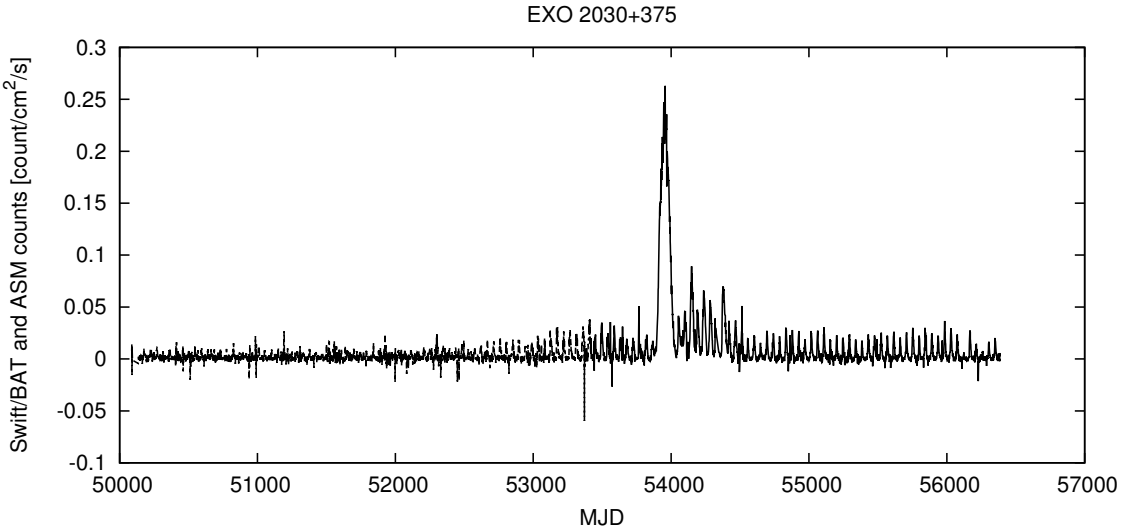

Figure 4.24: Long-term ASM (dashed line) and Swift/BAT (solid line) X-ray lightcurve of EXO 2030+375. The ASM count rates have been scaled by a factor of 165 to account for the different energy bands of the two instruments.

4.2.5 A1118-617

Overview

A1118-617 is an X-ray transient which was discovered by the *Ariel-5* satellite in 1974 during a type II outburst (Rosenberg et al. 1975). The optical companion in the BeXB is an O9.5IV-Ve star at a distance 5 ± 2kpc (Janot-Pacheco et al. 1981). In the analysis of data obtained with *RXTE/PCA*, Staubert et al. (2011) derived the orbital parameters: $P_{orb} = 24.0 \pm 0.4$ days, $a_X sini = 54.85 \pm 1.4$ lt-s, $e = 0.0$, $P_{spin} = 407.6546 \pm 0.0011$ s.

Results

Between MJD49000 and MJD51200 the radius calculations display a decreasing then increasing trend (Fig. 4.25), having a minimum at $r \sim 4.7 \times 10^{10}$m and peaking at $r \sim 6.3 \times 10^{10}$m. The two data points at MJD53447 and MJD53865 show an increasing trend with values of $r \sim 5.8 \times 10^{10}$m and $r \sim 6.3 \times 10^{10}$m respectively. The two SALT data points are at $r \sim 5 \times 10^{10}$m, below the orbital radius of the NS. The X-ray lightcurve (Fig. 4.26) of A1118-617 is characterised by long periods of quiescence and rare type II outburst events. Prior to the outburst observed in 2009 (peak at ∼MJD54845) the system displayed one other outburst in January 1992 (Coe et al. 1994) since its discovery in 1974.

The relatively large disc radius sizes (strong H_α emission), circular orbit and low X-ray activity is consistent with the large orbit of the NS, as was expected by Okazaki & Negueruela (2001).

Only the combined data (4U 0115+634, A 0535+262 & V0332+53) were used to produce the radius plot since A1118-617 does not show any double peak H_α emission lines in its spectra.

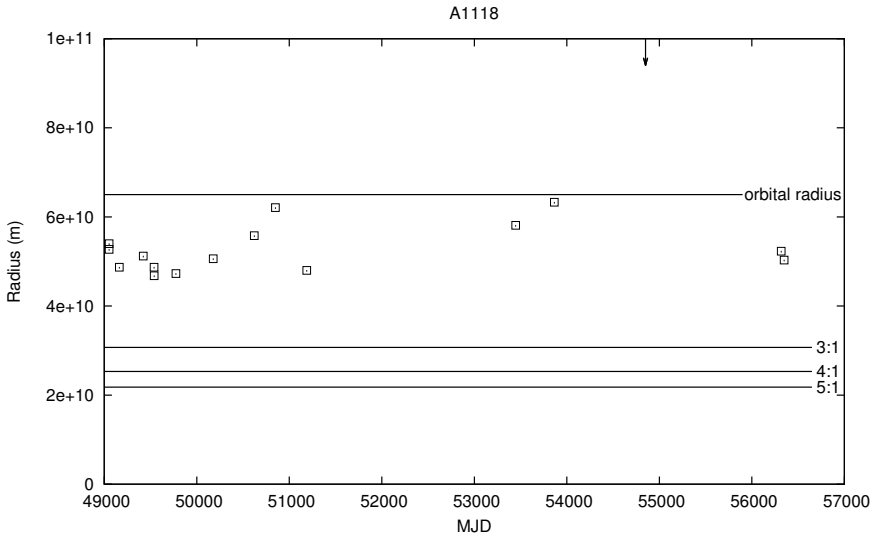

Figure 4.25: H_α radius versus MJD using combined data (A0535, V0332 and 4U0115). The 5:1, 4:1, 3:1 and the orbital radius of the NS are indicated.

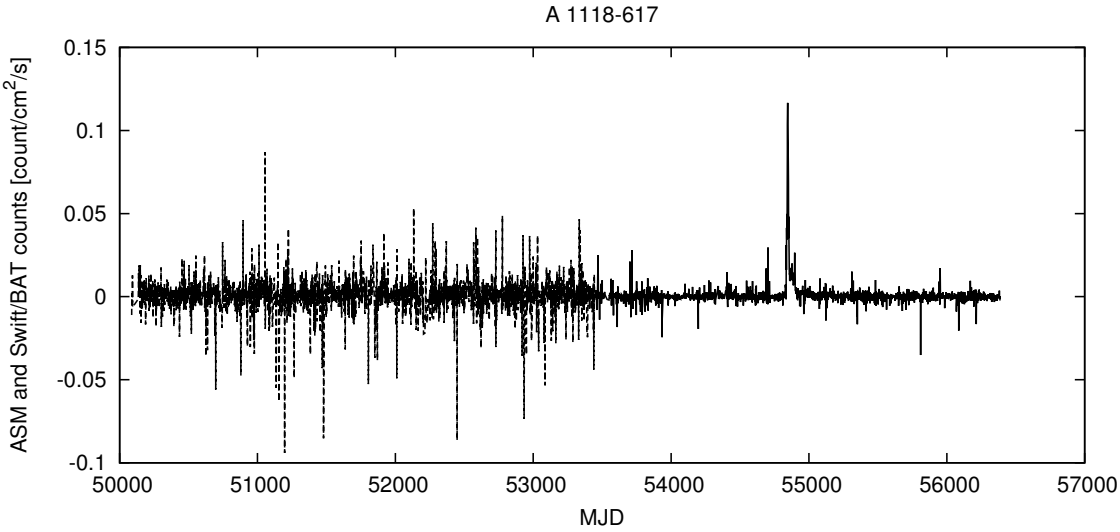

Figure 4.26: Long-term ASM (dashed line) and Swift/BAT (solid line) X-ray lightcurve of A 1118-617. The ASM count rates have been scaled by a factor of 90 to account for the different energy bands of the two instruments.

Chapter 5

Results, Analysis and Discussion II: LS I +61 303

As part of the long term monitoring programme of the circumstellar discs of Be stars in HMXBs, we have obtained 16 red optical spectra of LSI with the LT (FRODOSpec) between 2009 November and 2010 July. Fig. 5.1 shows the evolution of the H_α emission line from the spectra obtained. The spectra are normalised and are plotted with the same offset sequentially in time. The modified Julian dates (MJD) are given on the left hand side, as well as the corresponding orbital phases folded on the 26.496 day orbital period (Gregory 2002). The H_α emission line shows a double-peaked profile, typical of the circumstellar discs of Be stars. The emission line is asymmetric (class II), where although we see variability on a timescale of days, the red peak is generally dominant over the blue peak.

To look at the changes in the peak strengths more quantitively, we made a plot of the peak ratio (V/R) as a function of orbital phase (Fig. 5.2). From Fig. 5.2, we see that the value of V/R remains below one for a majority of the orbit, and has a maximum between phase 0.75 and 0.85 (around apastron passage). Similar behaviour in the peak ratio was reported by Liu et al. (2000), where around orbital phase 0.8 the red peak is not dominant as it is at other phases. In a photometric and spectroscopic study of LSI, Paredes et al. (1994) noticed a maximum in V/R between orbital phases 0.7 and 0.8. The spectra presented by Zamanov et al. (1999), however, show two maxima in V/R: one at phase 0.25 (near periastron passage) and another at phase 0.8. The V/R ratio was again seen to peak near periastron, at phase 0.30, by Grundstrom et al. (2007).

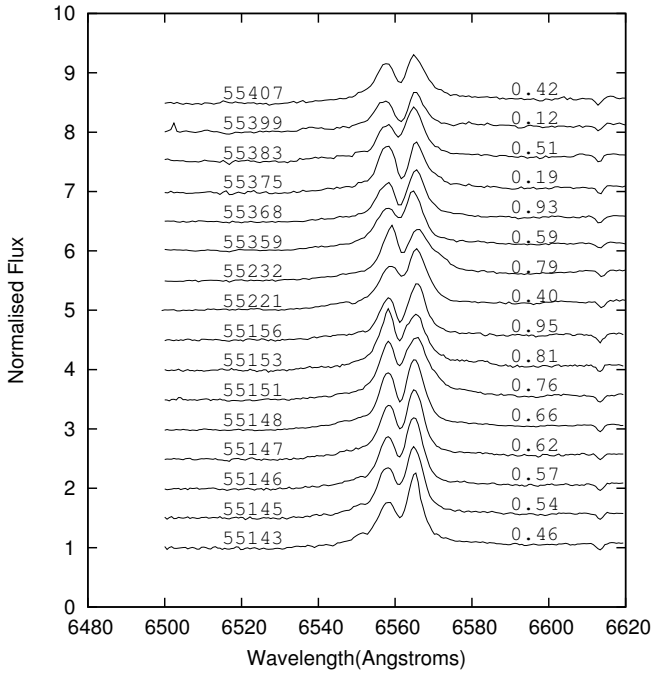

Figure 5.1: The evolution of the H_α line profile from LT spectra. The MJD are shown on the left hand side with corresponding orbital phase values on the right hand side.

Further dramatic changes were seen in the H_α line profile near apastron by Liu & Yan (2005), when it was seen that the blue peak displayed rapid variability while the red peak hardly changes.

Fig. 5.3 is a plot of the H_α equivalent width [EW(H_α)] as a function of time. The measurements are given in Table 1. The data from our programme is combined with published measurements from Paredes et al. (1994), Zamanov et al. (1999), Liu et al. (2000), Liu and Yan (2005), Grundstrom et al. (2007), McSwain et al. (2010), as well as unpublished spectra obtained with the Skinakas telescope*. The vertical lines in the plot show the radio ephemeris given by $t_{\rm po} = t_0 + k \times P_0$; where $t_0 = 2443366.775$, k is the outburst number, and P_0 is the superorbital period (1667 days). The EW(H_α) measurements for the dataset vary between -6 and -20. Three peaks are visible, with the time interval between the first two peaks on the order of the superorbital period obtained from radio analysis. The time interval between the second and third peak is

*in private communication with Pablo Reig.

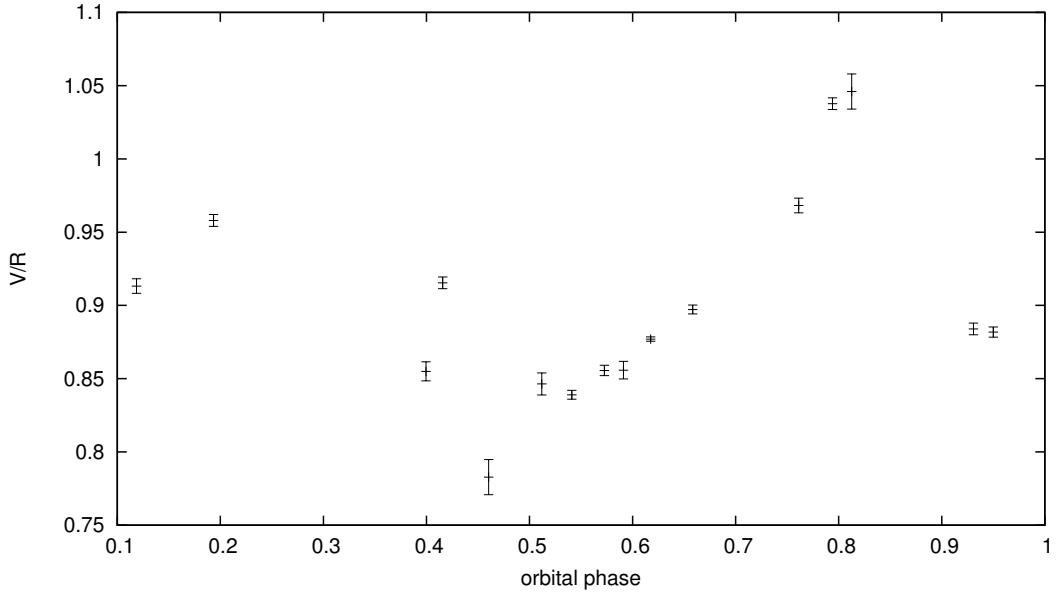

Figure 5.2: V/R ratio as a function of orbital phase folded on the 26.496 day orbital period.

$\sim$4800 days, owing to lack of data between the peaks. As can be seen from the plot, the peaks in the EW(H_α) are shifted with respect to the radio outbursts by a superorrbital phase of $\sim$0.2 (similar to the shift between radio and X-ray outbursts).

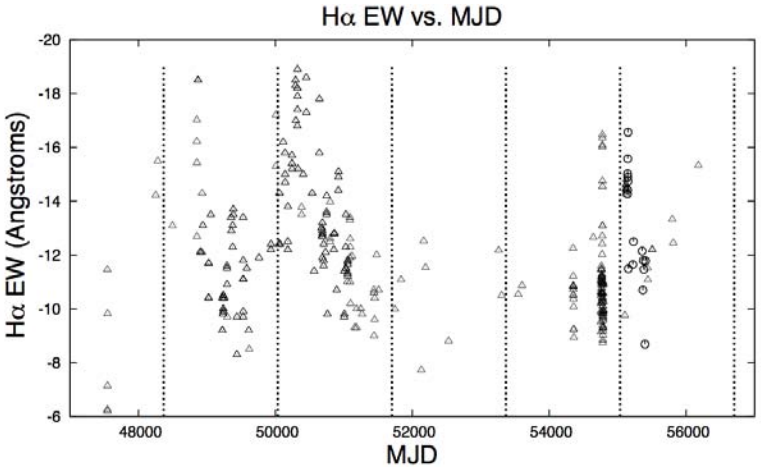

Figure 5.3: EW(H_α) as a function of MJD covering 23 years (January 1989 - August 2012). The vertical lines are times of radio outbursts. The triangles represent data from Paredes et al. (1994), Zamanov et al. (1999), Liu et al. (2000), Liu and Yan (2005), Grundstrom et al. (2007) and McSwain et al. (2010), while the circles represent data from LT.

Table 5.1: EW(H_α) measurements from the spectra obtained with LT.

MJD	EW(H_α) (Å)	error [EW(H_α)] (Å)	ϕ, orbital phase (folded on P_{orb} = 26.496 d)
55143	-14.27	0.10	0.46
55145	-15.02	0.08	0.54
55146	-14.42	0.08	0.57
55147	-14.90	0.17	0.62
55148	-15.58	0.24	0.66
55153	-16.56	0.06	0.76
55154	-14.75	0.11	0.81
55221	-11.27	0.09	0.40
55231	-12.50	0.11	0.79
55358	-12.15	0.09	0.59
55367	-10.67	0.05	0.93
55368	-11.49	0.21	0.95
55375	-11.80	0.16	0.19
55383	-11.47	0.28	0.51
55399	-8.69	0.13	0.12
55407	-11.79	0.07	0.42

5.1 Timing analysis

Fig. 5.4 is the resulting Lomb-Scargle (Lomb 1976, Scargle 1982) periodogram of the EW(H_α) light curve in Fig. 5.3. The Lomb-Scargle method is used for period searches of random, unevenly sampled data and is based on a least-squares fit of sinusoids (Press & Rybicki 1989). For a dataset with values h observed at time t (i.e. $h(t_i)$, for $i = 1, 2, ..., N$), the mean of the time series is given by (Press & Rybicki 1989):

$$\bar{h} = \frac{1}{N}\sum_{i}^{n} h_i$$

and the variance:

$$\sigma^2 = \frac{1}{N-1}\sum_{i}^{n}(h_i - \bar{h})^2$$

Press & Rybicki (1989) demonstrated that for each angular frequency $\omega = 2\pi f$ the Lomb-Scargle normalised periodogram is given by:

$$P_N(\omega) = \frac{1}{2\sigma^2}\left\{\frac{[\sum_j (h_j - \bar{h})\cos\omega(t_j - \tau)]^2}{\sum_j \cos^2\omega(t_i - \tau)} + \frac{[\sum_j (h_j - \bar{h})\sin\omega(t_j - \tau)]^2}{\sum_j \sin^2\omega(t_i - \tau)}\right\}$$

The parameter τ is given by:

$$\tan(2\omega\tau) = \frac{\sum_j \sin 2\omega t_j}{\sum_j \cos 2\omega t_j}$$

Two peaks are detected from the Lomb-Scargle analysis: one at a frequency 0.0373 cycles/day (P =26.81±0.044 days) with a power of 20.03, and another at frequency 0.000589 cycles/day (P = 1696.35±19.6 days)* with a power of 25.45. To determine the significance of the detected peaks, Monte Carlo simulations with white noise light curves were performed. A random number generator was used to scramble the original EW(H_α) light curve to create 10 000 "fake" light curves with the same time structure. We then performed Lomb-Scargle analysis, and from the periodograms produced, the highest powers were recorded. These were then sorted and the powers at 90%, 99% and 99.9% were obtained. The 99.9% level was found to be at a power of 16.658, and thus

*Our detection of the superorbital period in EW(H_α) was recently confirmed by Zamanov et al. (2013) in a long term spectroscopic study of LSI.

this suggests that the two peaks found have a >99.9% significance. We also checked the significance by producing 10 000 light curves with a random number generator but using the standard deviation and average EW(H_α) of the original light curve. The values of the significance levels obtained are very similar to those obtained using the method explained above.

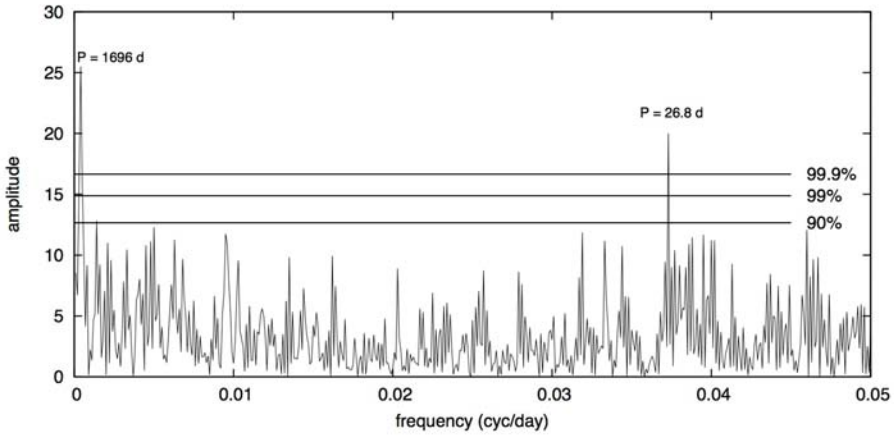

Figure 5.4: Lomb-Scargle periodogram of the EW(H_α) light curve of LSI, with 90%, 99% and 99.9% significance level lines shown.

Chapter 6

Conclusions

6.1 Galactic BeXBs

H_α spectra of five Galactic BeXBs were analysed in this thesis. The optical data were combined with publicly available X-ray data obtained with the *Swift/BAT* and *ASM* instruments. The H_α emission line was used to estimate the size of the circumstellar disc and study how its variability affects mass accretion in the context of the viscous decretion disc model.

6.1.1 A 0535+262

The results obtained generally agree with predictions made by Okazaki & Negueruela (2001). At truncation radii below the 4:1 r_{res} we see no type I outbursts, except for the period ∼MJD51000 − MJD54000 where type I outbursts separated by ∼300 days are observed (while the disc was recovering from a disc-loss phase). The outbursts had already begun occurring when the disc was still below the 7:1 r_{res}. Perhaps these were the result of an elongated disc precessing every ∼300 days in the direction of the NS at periastron passage.

6.1.2 4U 0115 +63

The disc variability agrees with model predictions made by Okazaki & Negueruela (2001); for the most part the disc is truncated at the 3:1 and 4:1 r_{res} with no regular type I outbursts observed. An apparent rapid disc-growth is seen at ∼MJD50000 and as the disc was on the decline (but still above the 3:1 r_{res}) after that, low intensity temporary

type I outbursts were observed, in agreement with the proposed orbital model for the system.

6.1.3 V 0332+53

The early measurements (∼MJD48000 − MJD49500) show sizes larger than the 3:1 and 4:1 r_{res} at which the disc is predicted to be truncated. The disc sizes disagree with the model predictions, as the sizes are significantly larger than the 3:1 r_{res} (which is comparable to the mean critical lobe radius at periastron passage of the NS) accompanied with no X-ray outbursts. The LT measurements, however, agree with model predictions. At the start of the monitoring campaign with the LT the disc sizes were significantly larger than the 3:1 r_{res} accompanied with type I outbursts. Once the matter in the disc was accreted the disc size went below the 3:1 r_{res} and the system has since been in quiescence.

6.1.4 EXO 2030+375

The early measurements (∼MJD48900 − MJD50300) agree with model predictions, where disc sizes ranging from just below the 3:1 r_{res} to sizes significantly smaller than the 5:1 r_{res} are seen, accompanied with small flaring in the X-ray lightcurve, as well as low intensity type I outbursts. The LT measurements display disc sizes above the predicted 4:1 r_{res} truncation (which is close to the critical lobe radius at periastron passage of the NS) and just larger than the periastron passage of the NS accompanied by regular type I outbursts.

6.1.5 A 1118-67

The disc size remains below the orbital radius of the NS for a large majority of the circular orbit, consistent with the low X-ray activity, as matter is not accreted.

Summary

The type I outbursts are generally seen to occur when the disc is close to/larger than the mean critical lobe radius at periastron passage of the NS, in agreement to the models presented by Okazaki & Negueruela. Type II outbursts, however, are more difficult to predict solely based on disc size information, as they do not necessarily show any depen-

dence on the extent of the disc. They are sometimes seen to occur at relatively small disc sizes, significantly below the the mean critical lobe radius at periastron passage (e.g. for the early measurements of A 0535+262 and 4U 0115+63) and at other times they are seen to occur at large disc sizes (during the LT coverage of A 0535+262 and 4U 0115+63). Extra information on the H_α profile variability around the period of type II outbursts is needed to study events taking place in the disc in more detail to check the effects of warping, as well as the orientation of the disc with respect to the NS (the manner in which the NS passes the circumstellar disc at periastron passage).

6.2 LS I +61 303

H_α spectra of LSI were analysed in this thesis to study the variation of the circumstellar disc around the Be star. The variability of the H_α line profile was studied, where it was noted that the red peak is generally less variable compared to the blue peak. The red peak is dominant for a large majority of the orbit, with V/R seen to peak at orbital phase range $0.7-0.8$, behaviour in the peak variations that has been reported previously. Long term periodic variability in the H_α equivalent width over a 23 year period is seen from the plot of EW(H_α) vs. time. Timing analysis of the EW(H_α) was performed and the resulting Lomb-Scargle periodogram revealed the 26-day and 4.5-year periods which have been reported at other wavelengths. Thus the periodic behaviour in LSI is likely to be attributed to the variability in the circumstellar disc. The four year modulation of the H_α emission line strengths can be explained by the following proposed models for the origin of the superorbital period:

- quasi-cyclic Be star envelope variations (Gregory et al. 1989)
- precession of the Be star (Lipunov & Nazin 1994)
- outward-moving density enhancement in the disc (Gregory & Neish 2002)
- variability of mass loss from the Be star.

Simultaneous long term multiwavelength monitoring programmes on LSI could provide an understanding of the puzzling issues presented from the different studies of the system.

6.3 Future Prospects

With the High Resolution Spectrograph (HRS) undergoing science commission on SALT it will be possible in the near future to obtain high resolution spectra in the follow-up of southern BeXBs. Observational evidence of a precessed warped Be disc resulting in giant outbursts (as well as bright normal outbursts) in A 0535+262 was investigated by Moritani et al. (2013). The results were inferred from a detailed analysis of the H_α line profile variability from high-dispersion spectroscopic monitoring. A similar study of long-term monitoring of a sample of BeXBs can shed light on the processes that lead to these outburst events and help test the theory proposed by Okazaki et al. (2013) for the origin of the outburst events in BeXBs and possibly help make robust predictions of them based on the behaviour of the line profile.

The method used for disc radius calculation can be re-evaluated and modified, as it makes very simple assumptions. As noted by Grundstrom et al. (2007) when comparing their radius estimates to those of Coe et al. (2006), the method used in this thesis considers only the brightest parts of the disc (the optically thin regions are not taken into consideration). Radius estimates of A 0535+262 obtained from data taken in August 2005 by Coe et al. (2006) are larger (about ∼80% larger) than those obtained by Grundstrom et al. (2007). It was suggested that this discrepancy could arise from ΔV being underestimated from the fit of $\log(\frac{\Delta V}{2vsini})$ vs $\log(-EW)$ for strong emission, resulting in overestimates of radius sizes.
The slope and intercept in the plot of $\log(\Delta V/2v\sin i)$ vs. $\log(-EW)$ could have changed significantly with the inclusion of the relatively large EW(H_α) measurements of A 1118-616, resulting in a change of radii estimates due to different a and b parameters (the cluster of points around the large $\log(-EW)$ values would drive the slope to steeper or more gradual values, depending on the corresponding values of $\log(\Delta V/2v\sin i)$, as the x-range covered for the mean data would be wider.

A multiwavelength project for the study of gamma-ray binaries (GRBs) will be undertaken to investigate various properties of the systems to understand the physical processes taking place. From the known GRB sources, the nature of the compact object is still unknown for a majority of these - a component of the project will be to reveal the nature of the compact objects through pulsation search techniques in order to distinguish between the competing microquasar and pulsar wind models. Another major

component of the project is to initiate radio observations with the Australia Telescope Compact Array (ATCA) to detect radio flux of candidate GRBs in the SMC. Cross-correlation of very high energy (VHE) from Fermi/Large Area Telescope (LAT) with radio, IR, optical and X-ray catalogues will constrain the large error circle of the Fermi LAT 2-year Source Catalog (2FGL) of GRB sources. With sensitive instruments such as the Cherenkov Telescope Array (CTA), MeerKAT and ASKAP operational in the near future the number of GRBs is expected to increase and the physical processes taking place in these systems will be understood better.

Appendix A

Data

The following are the H_α emission line parameters of the BeXBs in study. Columns 1 and 2 list the dates and modified Julian dates, respectively, of the observations. The measured EW(H_α) and ΔV are given in columns 3 and 4, respectively. The EW(H_α) are given in units of Å and ΔV in m/s. Only the ΔV measurements obtained directly (from double-peaked line profiles) are displayed. The telescopes used to obtain the spectra are listed in column 5 (*Programme 1*): Jacobus Kapetyn Telescope (JKT), R1299Y grating; Isaac Newton Telescope (INT), R1200R grating; Skinakas Telescope (Ski), 1301 l/mm grating; South African Astronomical Observatory 1.9-m telescope (SAAO), 1200 l/mm grating. Two tables are displayed for each object listing parameters obtained from data obtained from *Programme 1* and LT/SALT.

Table A.1: **EW(H_α) and ΔV measurements for A 0535+262 from *Programme 1*.**

Date (yyyy - mm - dd)	MJD	EW(H_α) (Å)	ΔV (m/s)	Telescope
1987 - 03 - 10	46867.54	-13.45		INT
1987 - 12 - 14	47145.47	-9.18		INT
1987 - 12 - 14	47145.47	-9.29		INT
1987 - 12 - 24	47155.47	-8.93		INT
1987 - 12 - 31	47162.47	-8.24		INT
1988 - 03 - 10	47232.78	-10.75		INT
1990 - 11 - 14	48211.26	-8.80	1.96×10^5	INT
1990 - 11 - 14	48211.26	-8.78	1.98×10^5	INT

Continued on next page

Table A.1 – continued from previous page

Date (yyyy - mm - dd)	MJD	EW(H_α) (Å)	ΔV (m/s)	Telescope
1990 - 11 - 14	48211.26	-8.80	1.95×10^5	INT
1990 - 12 - 27	48254.70	-9.85	2.0×10^5	INT
1990 - 12 - 27	48254.70	-9.81	2.02×10^5	INT
1990 - 12 - 27	48254.70	-10.01	2.07×10^5	INT
1991 - 01 - 27	48285.14	-8.15	2.03×10^5	INT
1991 - 01 - 27	48285.14	-8.36	2.05×10^5	INT
1991 - 04 - 16	48365.45	-6.12	2.25×10^5	WHT
1991 - 08 - 28	48499.20	-7.95	2.26×10^5	INT
1991 - 12 - 13	48605.94	-10.21	2.32×10^5	INT
1992 - 08 - 17	48852.94	-6.01		INT
1993 - 03 - 08	49057.00	-11.65		INT
1994 - 03 - 25	49439.24	-8.51		JKT
1994 - 03 - 25	49439.24	-8.47		JKT
1994 - 03 - 26	49440.24	-8.52		JKT
1994 - 03 - 27	49441.24	-8.67		JKT
1994 - 09 - 16	49613.36	-9.63	2.41×10^5	JKT
1994 - 11 - 10	49668.23	-10.48	2.39×10^5	SAAO
1995 - 02 - 12	49761.54	-8.68	2.4×10^5	JKT
1995 - 02 - 26	49775.54	-8.93	2.28×10^5	SAAO
1995 - 02 - 28	49777.54	-8.09	2.47×10^5	JKT
1995 - 08 - 06	49938.17	-8.69	2.36×10^5	JKT
1995 - 11 - 18	50041.48	-7.34	2.46×10^5	SAAO
1995 - 11 - 19	50042.48	-7.14	2.48×10^5	SAAO
1995 - 11 - 20	50043.48	-7.12	2.43×10^5	SAAO
1995 - 11 - 20	50043.48	-6.93	2.26×10^5	SAAO
1995 - 11 - 29	50052.48	-7.82	2.44×10^5	JKT
1996 - 04 - 04	50179.66	-7.92	2.48×10^5	SAAO
1997 - 10 - 26	50749.53	-7.36	2.52×10^5	JKT
1997 - 10 - 27	50750.53	-7.75	2.52×10^5	JKT
1997 - 10 - 28	50751.53	-7.88	2.52×10^5	JKT
1998 - 02 - 06	50851.27	-5.25	2.63×10^5	SAAO

Continued on next page

Table A.1 – continued from previous page

Date (yyyy - mm - dd)	MJD	EW(H_α) (Å)	ΔV (m/s)	Telescope
1998 - 11 - 26	51145.20	-0.99	4.81×10^5	INT
1998 - 11 - 26	51145.20	-0.92	4.75×10^5	INT
1998 - 12 - 24	51173.64	-0.73	4.66×10^5	WHT
1999 - 02 - 04	51214.51	-0.65	4.46×10^5	INT
1999 - 02 - 22	51232.51	-0.93	4.50×10^5	INT
1999 - 02 - 22	51232.51	-0.92	4.52×10^5	INT
1999 - 03 - 04	51244.95	-0.85	4.46×10^5	INT
1999 - 03 - 04	51244.95	-0.78	4.48×10^5	INT
1999 - 03 - 07	51247.95	-0.67	4.45×10^5	INT
1999 - 10 - 20	51474.01	-3.14	3.07×10^5	INT
2000 - 01 - 16	51560.82	-7.10		Ski
2001 - 09 - 12	52165.56	-7.96		Ski
2001 - 10 - 8	52192.50	-11.38	1.81×10^5	Ski
2002 - 09 - 11	52529.80	-11.66		Ski
2002 - 12 - 13	52623.61	-11.29	2.34×10^5	Ski
2003 - 10 - 06	52920.98	-24.49	1.76×10^5	Ski
2004 - 10 - 24	53303.72	-11.91		Ski
2005 - 08 - 16	53600.09	-11.54		Ski
2005 - 08 - 16	53600.09	-11.36		Ski
2005 - 08 - 16	53600.09	-11.53		Ski
2005 - 08 - 17	53601.09	-11.55		Ski
2005 - 08 - 17	53601.09	-12.03		Ski
2005 - 03 - 19	53450.91	-12.75		Ski

Table A.2: **EW(H_α) and ΔV measurements for A 0535+262 for observations performed with LT.**

Date (yyyy - mm - dd)	MJD	EW(H_α) (Å)	ΔV (m/s)	Telescope
2009 - 12 - 01	55167.81	-20.06		LT
2009 - 12 - 03	55169.81	-19.44		LT

Continued on next page

Table A.2 – continued from previous page

Date (yyyy - mm - dd)	MJD	EW(H_α) (Å)	ΔV (m/s)	Telescope
2009 - 12 - 06	55172.81	-19.09		LT
2009 - 12 - 10	55176.81	-18.56		LT
2009 - 12 - 26	55192.81	-19.47		LT
2009 - 12 - 31	55197.81	-19.49		LT
2010 - 01 - 03	55200.25	-20.27		LT
2010 - 01 - 07	55204.25	-19.40		LT
2010 - 01 - 12	55209.25	-19.67		LT
2010 - 01 - 15	55212.25	-18.45		LT
2010 - 01 - 17	55214.25	-17.54		LT
2010 - 01 - 22	55219.25	-17.97		LT
2010 - 01 - 24	55221.25	-17.62		LT
2010 - 01 - 27	55224.25	-16.00		LT
2010 - 10 - 25	55496.18	-9.90		LT
2010 - 10 - 26	55497.18	-10.14		LT
2010 - 10 - 29	55500.18	-9.64		LT
2010 - 11 - 01	55502.61	-8.86		LT
2010 - 11 - 04	55505.61	-8.89		LT
2010 - 11 - 07	55508.61	-8.65		LT
2010 - 11 - 12	55513.61	-9.19		LT
2010 - 11 - 15	55516.61	-9.90		LT
2010 - 11 - 16	55517.61	-9.71		LT
2010 - 11 - 19	55520.61	-9.88		LT
2010 - 11 - 22	55523.61	-9.15		LT
2010 - 11 - 14	55515.61	-9.34		LT
2010 - 12 - 23	55555.05	-9.51		LT
2011 - 02 - 16	55609.43	-8.78	2.17×10^5	LT
2011 - 02 - 18	55611.43	-8.72	2.22×10^5	LT
2011 - 02 - 20	55613.43	-9.47	2.14×10^5	LT
2011 - 02 - 22	55615.43	-9.64	2.15×10^5	LT
2011 - 02 - 24	55617.43	-9.01	2.27×10^5	LT
2011 - 02 - 26	55619.43	-8.34	2.15×10^5	LT

Continued on next page

Table A.2 – continued from previous page

Date (yyyy - mm - dd)	MJD	EW(H_α) (Å)	ΔV (m/s)	Telescope
2011 - 02 - 28	55621.43	-8.71	2.4×10^5	LT
2011 - 03 - 2	55625.86	-9.35	2.3×10^5	LT
2011 - 04 - 5	55659.30	-7.82	2.23×10^5	LT
2011 - 04 - 7	55661.30	-8.07	2.2×10^5	LT
2011 - 04 - 13	55667.30	-8.13	2.36×10^5	LT
2011 - 09 - 30	55836.48	-7.12	2.28×10^5	LT
2011 - 10 - 02	55838.92	-7.86	2.35×10^5	LT
2011 - 10 - 12	55848.92	-8.07	2.33×10^5	LT
2011 - 10 - 14	55850.92	-7.87	2.42×10^5	LT
2011 - 10 - 28	55864.92	-7.40	2.28×10^5	LT
2011 - 11 - 01	55868.36	-5.85	2.3×10^5	LT
2011 - 11 - 29	55896.36	-5.87	2.36×10^5	LT
2011 - 12 - 01	55898.79	-5.96	2.32×10^5	LT
2011 - 12 - 03	55900.79	-5.94	2.22×10^5	LT
2011 - 12 - 05	55902.79	-5.93	2.43×10^5	LT
2011 - 12 - 05	55902.79	-5.87	2.3×10^5	LT
2011 - 12 - 07	55904.79	-5.94	2.28×10^5	LT
2011 - 12 - 09	55906.79	-6.06	2.33×10^5	LT
2011 - 12 - 17	55914.79	-6.73	2.35×10^5	LT
2011 - 12 - 27	55924.79	-7.81	2.44×10^5	LT
2011 - 12 - 29	55926.79	-7.08	2.27×10^5	LT
2011 - 12 - 31	55928.79	-7.94	2.34×10^5	LT
2012 - 01 - 04	55932.23	-9.31	2.43×10^5	LT
2012 - 01 - 8	55936.23	-9.58	2.38×10^5	LT
2012 - 01 - 12	55940.23	-9.75	2.37×10^5	LT
2012 - 01 - 16	55944.23	-10.53	2.18×10^5	LT
2012 - 01 - 18	55946.23	-10.36	2.38×10^5	LT
2012 - 02 - 09	55967.67	-8.98	2.47×10^5	LT
2012 - 03 - 04	55993.10	-7.96	2.38×10^5	LT
2012 - 03 - 06	55995.10	-7.63	2.46×10^5	LT
2012 - 03 - 08	55997.10	-7.99	2.43×10^5	LT

Continued on next page

Table A.2 – continued from previous page

Date (yyyy - mm - dd)	MJD	EW(H_α) (Å)	ΔV (m/s)	Telescope
2012 - 09 - 02	56173.73	-8.60	2.41× 10^5	LT
2012 - 09 - 06	56177.73	-8.93	2.17× 10^5	LT
2012 - 09 - 28	56199.73	-8.91	2.18× 10^5	LT
2012 - 10 - 24	56226.16	-8.76	2.22× 10^5	LT
2012 - 10 - 26	56227.66	-6.86		LT
2012 - 11 - 23	56255.10	-7.42		LT
2012 - 12 - 07	56269.54	-8.58		LT
2012 - 12 - 23	56285.54	-8.46		LT
2012 - 12 - 29	56291.54	-8.43		LT
2012 - 12 - 31	56293.54	-8.50		LT
2013 - 01 - 02	56294.97	-8.43		LT
2013 - 01 - 08	56301.47	-11.00	1.98× 10^5	LT
2013 - 01 - 16	56308.97	-9.13		LT
2013 - 01 - 30	56322.97	-8.62		LT
2013 - 02 - 09	56332.41	-9.17		LT
2013 - 02 - 09	56332.41	-9.05		LT
2013 - 02 - 11	56334.41	-9.35		LT
2013 - 02 - 13	56336.41	-9.47		LT
2013 - 02 - 17	56340.41	-9.80		LT
2013 - 02 - 23	56346.91	-11.53	2.48× 10^5	LT
2013 - 02 - 25	56348.41	-10.17		LT

Table A.3: **EW(H_α) and ΔV measurements for 4U 0115+63 from *Programme 1*.**

Date (yyyy - mm - dd)	MJD	EW(H_α) (Å)	ΔV (m/s)	Telescope
1990 - 12 - 27	48254.70	-6.41	4.25× 10^5	INT
1990 - 12 - 27	48254.70	-6.37	4.19× 10^5	INT
1990 - 02 - 14	47936.83	-6.02		INT
1990 - 02 - 14	47936.83	-5.94		INT

Continued on next page

Table A.3 – continued from previous page

Date (yyyy - mm - dd)	MJD	EW(H_α) (Å)	ΔV (m/s)	Telescope
1991 - 01 - 27	48284.64	-8.45		INT
1991 - 01 - 27	48284.64	-6.64		INT
1991 - 01 - 27	48284.64	-6.25		INT
1991 - 08 - 28	48499.20	-6.38	4.6×10^5	INT
1991 - 12 - 14	48606.94	-6.62	4.86×10^5	INT
1991 - 12 - 14	48606.94	-6.59	4.79×10^5	INT
1992 - 08 - 05	48841.44	-5.36	4.05×10^5	INT
1992 - 08 - 05	48841.44	-5.10	4.3×10^5	INT
1993 - 11 - 18	49310.99		4.33×10^5	WHT
1993 - 12 - 17	49340.43	-6.32	4.0×10^5	WHT
1993 - 12 - 17	49340.43	-6.81	3.8×10^5	WHT
1993 - 12 - 17	49340.43	-7.21	3.93×10^5	WHT
1993 - 12 - 19	49342.43	-6.55	3.97×10^5	WHT
1993 - 12 - 19	49342.43	-6.35	3.9×10^5	WHT
1995 - 01 - 09	49727.61	-7.66		INT
1995 - 07 - 03	49904.73	-6.61	4.52×10^5	INT
1995 - 07 - 03	49904.73		4.43×10^5	INT
1995 - 09 - 12	49974.60	-6.82	4.12×10^5	INT
1995 - 09 - 12	49974.60	-3.66	4.09×10^5	INT
1996 - 01 - 12	50096.35	-13.02	2.45×10^5	INT
1996 - 01 - 12	50096.35	-12.58	2.44×10^5	INT
1996 - 01 - 12	50096.35	-11.81	2.5×10^5	INT
1996 - 01 - 31	50115.35	-9.67	3.07×10^5	INT
1996 - 01 - 31	50115.35	-8.86	3.16×10^5	INT
1996 - 06 - 20	50256.54	-8.73	3.2×10^5	INT
1996 - 07 - 09	50275.97	-6.92	4.2×10^5	INT
1996 - 07 - 09	50275.97	-7.30	4.11×10^5	INT
1997 - 02 - 01	50481.03	-5.12	4.58×10^5	INT
1998 - 09 - 10	51068.33	-7.08	3.53×10^5	INT
1998 - 08 - 01	51028.89	-7.52	3.58×10^5	INT
1998 - 09 - 28	51086.33	-7.92	2.74×10^5	INT

Continued on next page

Table A.3 – continued from previous page

Date (yyyy - mm - dd)	MJD	EW(H_α) (Å)	ΔV (m/s)	Telescope
2000 - 10 - 05	51824.25	-20.82	2.33× 10^5	Ski
2000 - 10 - 16	51835.25	-19.25	2.79× 10^5	Ski

Table A.4: **EW(H_α) and ΔV measurements for 4U 0115+63 for observations performed with LT.**

Date (yyyy - mm - dd)	MJD	EW(H_α) (Å)	ΔV (m/s)	Telescope
2010 - 01 - 24	55221.75	-3.93	5.2× 10^5	LT
2010 - 01 - 24	55221.75	-2.42	5.72× 10^5	LT
2010 - 06 - 13	55362.93	-3.76	3.98× 10^5	LT
2010 - 06 - 27	55376.93	-3.47	4.25× 10^5	LT
2010 - 06 - 27	55376.43	-4.32		LT
2010 - 06 - 27	55376.43	-4.14		LT
2010 - 07 - 25	55405.37	-5.16	4.75× 10^5	LT
2011 - 01 - 15	55577.49	-10.04		LT
2011 - 01 - 20	55582.49	-6.20		LT
2011 - 06 - 18	55732.67	-4.73		LT
2011 - 06 - 25	55739.67	-7.63		LT
2011 - 06 - 25	55739.67	-7.40		LT
2011 - 07 - 08	55753.61	-7.33	3.62× 10^5	LT
2011 - 07 - 15	55760.61	-6.95	5.14× 10^5	LT
2011 - 09 - 30	55835.98	-11.07		LT
2011 - 10 - 07	55843.42	-10.47		LT
2011 - 12 - 02	55899.29	-7.19		LT
2011 - 12 - 09	55906.29	-2.92		LT
2011 - 12 - 30	55927.29	-6.41		LT
2012 - 01 - 15	55942.73	-7.94		LT
2012 - 01 - 20	55947.73	-6.07		LT
2013 - 06 - 22	56467.16	-3.27		LT
2013 - 06 - 28	56473.16	-3.85		LT
2013 - 07 - 20	56496.09	-3.99	4.75× 10^5	LT

Table A.5: **EW(H_α) and ΔV measurements for V 0332+53 from *Programme 1*.**

Date (yyyy - mm - dd)	MJD	EW(H_α) (Å)	ΔV (m/s)	Telescope
1990 - 01 - 28	47920.40	-4.07		INT
1990 - 09 - 02	48137.89	-7.68		INT
1990 - 09 - 02	48137.89	-4.62		INT
1990 - 11 - 13	48210.26	-7.66	1.41e+05	INT
1990 - 11 - 14	48210.76	-6.42		INT
1990 - 11 - 14	48210.76	-6.09		INT
1990 - 11 - 14	48210.76	-6.07		INT
1990 - 12 - 27	48254.20	-8.34		INT
1990 - 12 - 27	48254.20	-6.90		INT
1991 - 01 - 27	48284.64	-6.72		INT
1991 - 01 - 27	48285.14	-7.68	1.38e+05	INT
1991 - 01 - 27	48285.14	-7.18	1.46e+05	INT
1991 - 08 - 28	48499.20	-5.36	1.49e+05	INT
1991 - 12 - 14	48606.94	-5.28	1.65e+05	INT
1992 - 08 - 18	48853.94	-4.99		INT
1992 - 11 - 13	48940.25	-3.84		INT
1992 - 11 - 13	48940.25	-2.91		INT
1993 - 12 - 5	49327.93	-8.45		INT
2000 - 10 - 16	51834.75	-3.85		Ski
2001 - 08 - 07	52130.12	-3.13		Ski
2000 - 07 - 19	51746.94	-5.21	1.28e+05	Ski
2000 - 10 - 16	51835.25		1.39e+05	Ski

Table A.6: **EW(H_α) and ΔV measurements for V 0332+53 for observations performed with LT.**

Date (yyyy - mm - dd)	MJD	EW(H_α) (Å)	ΔV (m/s)	Telescope
2009 - 12 - 26	55192.81	-5.09		LT
2009 - 12 - 26	55192.81	-5.18		LT

Continued on next page

Table A.6 – continued from previous page

Date (yyyy - mm - dd)	MJD	EW(H_α) (Å)	ΔV (m/s)	Telescope
2010 - 01 - 11	55208.25	-5.83		LT
2010 - 01 - 11	55208.25	-5.95		LT
2010 - 01 - 24	55221.25	-4.39		LT
2010 - 01 - 24	55221.25	-6.56		LT
2010 - 01 - 24	55221.25	-7.28		LT
2010 - 01 - 24	55221.25	-7.82		LT
2010 - 01 - 24	55221.25	-7.85		LT
2010 - 01 - 25	55222.25	-6.73		LT
2010 - 01 - 25	55222.25	-7.41		LT
2010 - 01 - 25	55222.25	-4.04		LT
2010 - 01 - 25	55222.25	-7.20		LT
2010 - 01 - 25	55222.25	-7.44		LT
2010 - 01 - 25	55222.25	-7.66		LT
2010 - 01 - 25	55222.25	-7.38		LT
2010 - 06 - 26	55375.43	-2.56		LT
2010 - 06 - 26	55375.43	-2.60		LT
2010 - 06 - 26	55375.43	-2.25		LT
2012 - 01 - 08	55935.73	-2.59		LT
2012 - 01 - 15	55942.73	-2.88		LT
2012 - 01 - 20	55947.73	-2.95		LT
2012 - 03 - 02	55990.60	-3.26		LT
2012 - 09 - 02	56173.23	-4.30		LT
2012 - 09 - 28	56199.23	-4.03		LT
2012 - 09 - 28	56199.23	-3.12		LT
2012 - 10 - 05	56206.66	-4.76		LT
2012 - 10 - 26	56227.66	-3.93		LT
2012 - 11 - 23	56255.10	-3.69		LT
2012 - 12 - 09	56271.54	-4.73		LT
2012 - 12 - 22	56284.54	-3.67		LT
2012 - 12 - 28	56290.54	-2.22		LT
2013 - 01 - 25	56317.97	-2.69		LT

Continued on next page

Table A.6 – continued from previous page

Date (yyyy - mm - dd)	MJD	EW(H_α) (Å)	ΔV (m/s)	Telescope
2013 - 02 - 09	56332.41	-3.51		LT
2013 - 02 - 23	56346.41	-2.00		LT

Table A.7: **EW(H_α) and ΔV measurements for EXO 2030+375 from *Programme 1.***

Date (yyyy - mm - dd)	MJD	EW(H_α) (Å)	ΔV (m/s)	Telescope
1992 - 10 - 02	48898.81	-13.51		WHT
1992 - 10 - 03	48899.81	-14.15		WHT
1993 - 10 - 03	49265.06	-14.07		WHT
1993 - 06 - 28	49168.31	-16.20		WHT
1993 - 06 - 28	49168.31	-15.84		WHT
1993 - 06 - 28	49168.31	-16.92		WHT
1993 - 06 - 29	49169.31	-17.06		WHT
1993 - 06 - 29	49169.31	-11.27		WHT
1993 - 06 - 29	49169.31	-16.45		WHT
1993 - 06 - 29	49169.31	-13.99		WHT
1993 - 06 - 29	49169.31	-14.33		WHT
1993 - 06 - 29	49169.31	-14.01		WHT
1993 - 06 - 29	49169.31	-13.51		WHT
1993 - 06 - 29	49169.31	-12.91		WHT
1993 - 06 - 29	49169.31	-13.42		WHT
1993 - 06 - 29	49169.31	-13.66		WHT
1993 - 06 - 29	49169.31	-11.72		WHT
1993 - 06 - 29	49169.31	-12.12		WHT
1993 - 06 - 29	49169.31	-12.56		WHT
1993 - 06 - 29	49169.31	-11.27		WHT
1993 - 06 - 30	49170.31	-14.32		WHT
1993 - 06 - 30	49170.31	-13.64		WHT
1993 - 06 - 30	49170.31	-13.42		WHT
1993 - 06 - 30	49170.31	-13.49		WHT
1993 - 06 - 30	49170.31	-12.50		WHT
1993 - 06 - 30	49170.31	-15.13		WHT
1993 - 06 - 30	49170.31	-10.38		WHT
1993 - 06 - 30	49170.31	-12.89		WHT
1996 - 07 - 08	50274.47	-4.38		WHT
1996 - 07 - 09	50275.47	-5.28		WHT

Continued on next page

Table A.7 – continued from previous page

Date (yyyy - mm - dd)	MJD	EW(H_α) (Å)	ΔV (m/s)	Telescope
1996 - 07 - 09	50275.47	-4.24		WHT
1996 - 07 - 09	50275.47	-4.78		WHT

Table A.8: **EW(H_α) and ΔV measurements for EXO 2030+375 for observations performed with LT.**

Date (yyyy - mm - dd)	MJD	EW(H_α) (Å)	ΔV (m/s)	Telescope
2011 - 03 - 25	55648.36	-24.99		LT
2011 - 04 - 08	55661.80	-24.18		LT
2011 - 04 - 23	55676.80	-24.02		LT
2011 - 05 - 13	55697.24	-24.66		LT
2011 - 05 - 20	55704.24	-24.39		LT
2011 - 06 - 03	55717.67	-23.95		LT
2011 - 06 - 11	55725.67	-24.78		LT
2011 - 06 - 17	55731.67	-23.76		LT
2011 - 06 - 25	55739.67	-25.15		LT
2011 - 07 - 02	55747.11	-24.90		LT
2011 - 07 - 08	55753.11	-24.61		LT
2011 - 07 - 15	55760.11	-24.54		LT
2011 - 10 - 07	55843.42	-25.44		LT
2011 - 12 - 02	55899.29	-25.90		LT
2011 - 12 - 10	55907.29	-24.57		LT
2012 - 03 - 11	55999.60	-22.87		LT
2012 - 06 - 08	56087.92	-21.97		LT
2012 - 06 - 30	56109.92	-21.43		LT
2012 - 07 - 30	56140.35	-22.90		LT
2012 - 08 - 01	56141.79	-24.63		LT
2012 - 08 - 03	56143.79	-25.31		LT
2012 - 08 - 05	56145.79	-23.31		LT
2012 - 09 - 02	56173.23	-22.68		LT

Continued on next page

Table A.8 – continued from previous page

Date (yyyy - mm - dd)	MJD	EW(H_α) (Å)	ΔV (m/s)	Telescope
2012 - 09 - 24	56195.23	-22.38		LT
2012 - 09 - 28	56199.23	-23.42		LT
2012 - 10 - 02	56203.66	-22.09		LT
2012 - 10 - 26	56227.66	-23.77		LT
2013 - 04 - 24	56408.28	-24.51		LT
2013 - 04 - 26	56410.28	-23.41		LT
2013 - 04 - 28	56412.28	-24.57		LT
2013 - 05 - 16	56430.72	-24.92		LT
2013 - 05 - 18	56432.72	-24.46		LT
2013 - 06 - 19	56464.16	-23.67		LT
2013 - 06 - 21	56466.16	-24.33		LT
2013 - 06 - 23	56468.16	-24.41		LT
2013 - 06 - 25	56470.16	-24.56		LT
2013 - 06 - 29	56474.16	-24.91		LT
2013 - 07 - 19	56494.59	-24.92		LT
2013 - 07 - 21	56496.59	-24.57		LT

Table A.9: **EW(H_α) and ΔV measurements for A 1118-617 from *Programme 1*.**

Date (yyyy - mm - dd)	MJD	EW(H_α) (Å)	ΔV (m/s)	Telescope
1993 - 03 - 03	49052.00	-45.62		SAAO
1993 - 03 - 04	49053.00	-44.68		SAAO
1993 - 06 - 23	49163.31	-41.72		SAAO
1994 - 03 - 07	49421.24	-43.59		SAAO
1994 - 07 - 02	49537.99	-41.68		SAAO
1994 - 07 - 03	49538.99	-40.34		SAAO
1995 - 02 - 25	49774.04	-40.68		SAAO
1996 - 04 - 03	50178.16	-43.15		SAAO
1997 - 06 - 20	50621.28	-46.89		SAAO
1998 - 02 - 05	50849.77	-51.47		SAAO
1999 - 01 - 09	51188.58	-41.21		SAAO
2005 - 03 - 15	53446.91	-48.56		SAAO
2006 - 05 - 07	53865.02	-52.29		SAAO

Table A.10: **EW(H_α) and ΔV measurements for A 1118-617 for observations performed with SALT.**

Date (yyyy - mm - dd)	MJD	EW(H_α) (Å)	ΔV (m/s)	Telescope
2013 - 02 - 26	56349.41	-42.88		SALT
2013 - 01 - 24	56316.97	-44.38		SALT

Appendix B

H_α line profiles

B.1 A selection of H_α line profiles obtained with the Liverpool Telescope and SALT.

B.1.1 A 0535+262

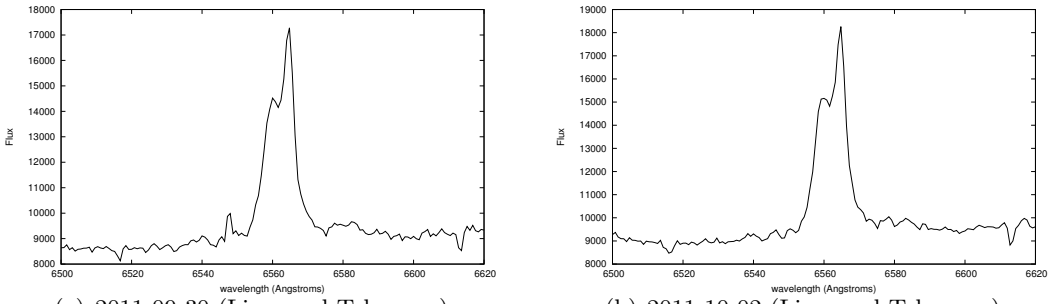

(a) 2011-09-30 (Liverpool Telescope) (b) 2011-10-02 (Liverpool Telescope)

Figure B.1

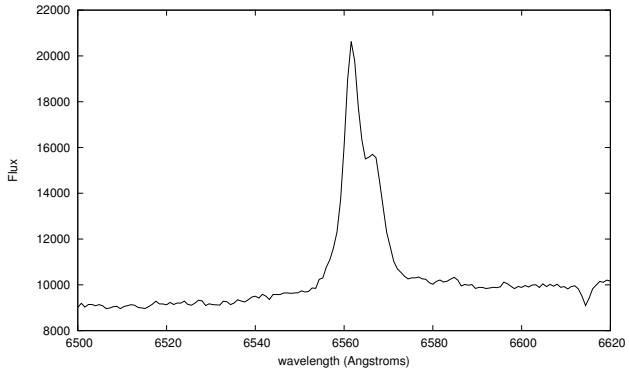

Figure B.2: 2011-04-13 (Liverpool Telescope)

B.1.2 4U 0115+63

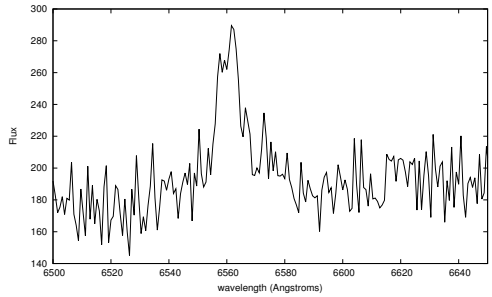

(a) 2011-06-18 (Liverpool Telescope)

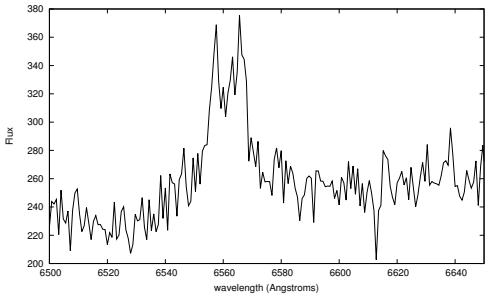

(b) 2011-07-08 (Liverpool Telescope)

Figure B.3

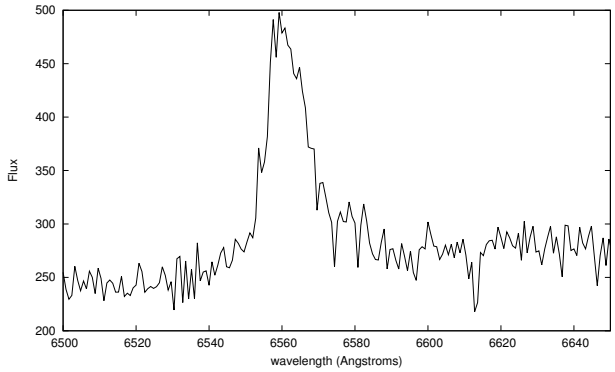

Figure B.4: 2011-09-30 (Liverpool Telescope)

B.1.3 V 0332+53

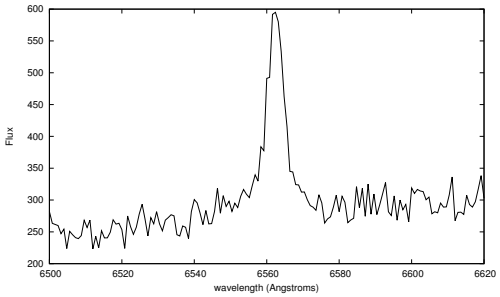

(a) 2010-01-24 (Liverpool Telescope)

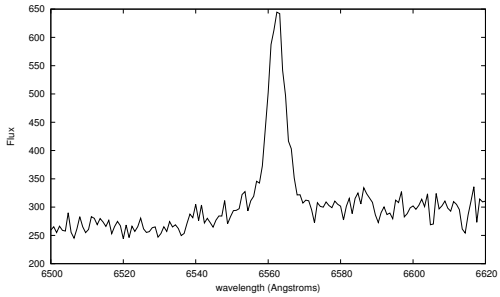

(b) 2010-01-25 (Liverpool Telescope)

Figure B.5

B.1.4 EXO 2030+375

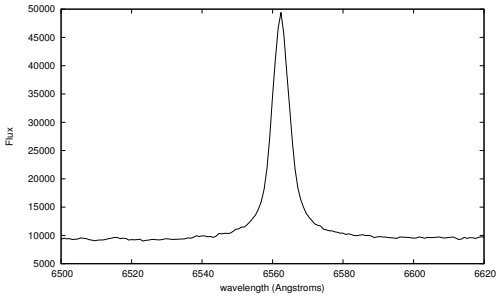

(a) 2013-04-26 (Liverpool Telescope)

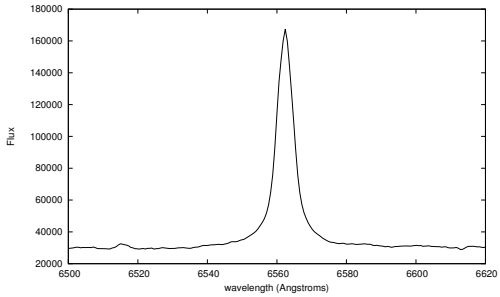

(b) 2013-07-19 (Liverpool Telescope)

Figure B.6

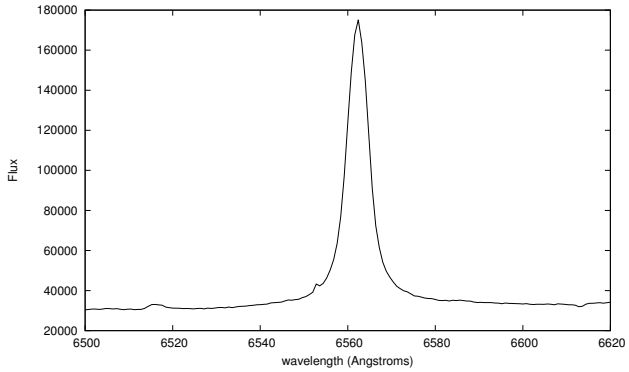

Figure B.7: 2011-04-08 (Liverpool Telescope)

B.1.5 A 1118-617

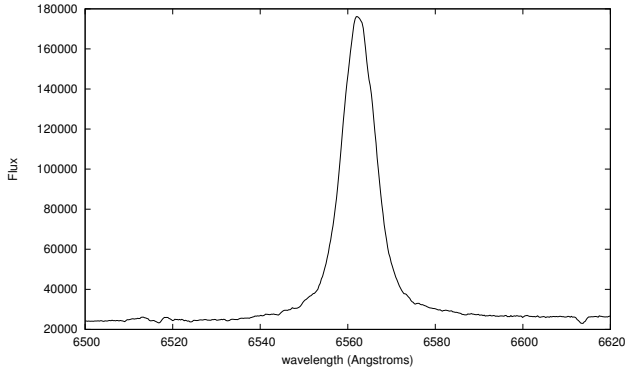

Figure B.8: 2013-02-26 (SALT)

Bibliography

Albert, J., Aliu, E., Anderhub, H., et al. 2008, ApJ, 684, 1351

Aragona, C., McSwain, M. V., Grundstrom, E. D., et al. 2009, ApJ, 698, 514

Barnes, S. I., Cottrell, P. L., Albrow, M. D., et al. 2008, in Society of Photo-Optical Instrumentation Engineers (SPIE) Conference Series, Vol. 7014, Society of Photo-Optical Instrumentation Engineers (SPIE) Conference Series

Barnsley, R. M., Smith, R. J., & Steele, I. A. 2012, Astronomische Nachrichten, 333, 101

Belczynski, K., & Ziolkowski, J. 2009, ApJ, 707, 870

Bildsten, L., Chakrabarty, D., Chiu, J., et al. 1997, ApJS, 113, 367

Bird, A. J., Coe, M. J., McBride, V. A., & Udalski, A. 2012, MNRAS, 423, 3663

Bjorkman, J. E., & Cassinelli, J. P. 1993, ApJ, 409, 429

Blandford, R. D., & Znajek, R. L. 1977, MNRAS, 179, 433

Boldin, P. A., Tsygankov, S. S., & Lutovinov, A. A. 2013, Astronomy Letters, 39, 375

Bosch-Ramon, V., Paredes, J. M., Romero, G. E., & Ribó, M. 2006, A&A, 459, L25

Buckley, D. A. H. 2001, in Astronomical Society of the Pacific Conference Series, Vol. 232, The New Era of Wide Field Astronomy, ed. R. Clowes, A. Adamson, & G. Bromage, 386

Buckley, D. A. H. 2005, in Astronomical Society of the Pacific Conference Series, Vol. 329, Nearby Large-Scale Structures and the Zone of Avoidance, ed. A. P. Fairall & P. A. Woudt, 273

Buckley, D. A. H. 2013, Selecting, Scheduling and Carrying Out Observing Programmes at SALT, 275–304

Buckley, D. A. H., Charles, P. A., Nordsieck, K. H., & O'Donoghue, D. 2006, in IAU Symposium, Vol. 232, The Scientific Requirements for Extremely Large Telescopes, ed. P. Whitelock, M. Dennefeld, & B. Leibundgut, 1–12

Caballero, I., Kretschmar, P., Santangelo, A., et al. 2007, in ESA Special Publication, Vol. 622, ESA Special Publication, 471

Caballero, I., Kretschmar, P., Pottschmidt, K., et al. 2010, X-ray Astronomy 2009; Present Status, Multi-Wavelength Approach and Future Perspectives, 1248, 147

Camero-Arranz, A., Finger, M. H., Wilson-Hodge, C. A., et al. 2012, ApJ, 754, 20

Carroll, B. W., & Ostlie, D. A. 2006, An introduction to modern astrophysics and cosmology

Casares, J., Negueruela, I., Ribó, M., et al. 2014, Nature, 505, 378

Casares, J., Ribas, I., Paredes, J. M., Martí, J., & Allende Prieto, C. 2005, MNRAS, 360, 1105

Cassinelli, J. P., Brown, J. C., Maheswaran, M., Miller, N. A., & Telfer, D. C. 2002, ApJ, 578, 951

Charles, P. A., & Wagner, R. M. 1996, S&T, 91, 38

Chauville, J., Zorec, J., Ballereau, D., et al. 2001, A&A, 378, 861

Chernyakova, M., Neronov, A., Molkov, S., et al. 2012, ApJ, 747, L29

Clark, J. S., Steele, I. A., Coe, M. J., & Roche, P. 1998, MNRAS, 297, 657

Coe, M. J., Edge, W. R. T., Galache, J. L., & McBride, V. A. 2005, MNRAS, 356, 502

Coe, M. J., Payne, B. J., Hanson, C. G., & Longmore, A. J. 1987, MNRAS, 226, 455

Coe, M. J., Payne, B. J., Longmore, A., & Hanson, C. G. 1988, MNRAS, 232, 865

Coe, M. J., Reig, P., McBride, V. A., Galache, J. L., & Fabregat, J. 2006, MNRAS, 368, 447

Collins, II, G. W. 1987, in IAU Colloq. 92: Physics of Be Stars, ed. A. Slettebak & T. P. Snow, 3–19

Corbet, R. H. D. 1984, A&A, 141, 91

—. 1986, MNRAS, 220, 1047

Cranmer, S. R. 2005, ApJ, 634, 585

—. 2009, ApJ, 701, 396

Crawford, S. M., Still, M., Schellart, P., et al. 2012, PySALT: SALT science pipeline, astrophysics Source Code Library

Dachs, J., Hanuschik, R., Kaiser, D., & Rohe, D. 1986, A&A, 159, 276

Dachs, J., Kiehling, R., & Engels, D. 1988, A&A, 194, 167

Dachs, J., & Wamsteker, W. 1982, A&A, 107, 240

Dhawan, V., Mioduszewski, A., & Rupen, M. 2006, in VI Microquasar Workshop: Microquasars and Beyond

Dubus, G. 2006, A&A, 456, 801

Espinosa Lara, F., & Rieutord, M. 2012, A&A, 547, A32

Fender, R. P. 2003, MNRAS, 340, 1353

Finger, M. H., Camero-Arranz, A., Kretschmar, P., Wilson, C., & Patel, S. 2006, in Bulletin of the American Astronomical Society, Vol. 38, AAS/High Energy Astrophysics Division #9, 359

Finger, M. H., Cominsky, L. R., Wilson, R. B., Harmon, B. A., & Fishman, G. J. 1994, in American Institute of Physics Conference Series, Vol. 308, The Evolution of X-ray Binariese, ed. S. Holt & C. S. Day, 459

Finger, M. H., Wilson, R. B., & Harmon, B. A. 1996, ApJ, 459, 288

Forman, W., Jones, C., Cominsky, L., et al. 1978, ApJS, 38, 357

Frail, D. A., & Hjellming, R. M. 1991, AJ, 101, 2126

Frank, J., King, A., & Raine, D. J. 2002, Accretion Power in Astrophysics: Third Edition

Gehrz, R. D., Hackwell, J. A., & Jones, T. W. 1974, ApJ, 191, 675

Giacconi, R., Murray, S., Gursky, H., et al. 1972, ApJ, 178, 281

Gies, D. R., Bagnuolo, Jr., W. G., Baines, E. K., et al. 2007, ApJ, 654, 527

Giovannelli, F., & Graziati, L. S. 1992, Space Sci. Rev., 59, 1

Gomboc, A., Bode, M. F., Carter, D., et al. 2003, ArXiv Astrophysics e-prints

Gregory, P. C. 1999, ApJ, 520, 361

—. 2002, ApJ, 575, 427

Gregory, P. C., & Loredo, T. J. 1992, ApJ, 398, 146

Gregory, P. C., & Taylor, R. 1978, IAU Circ., 3164, 1

Gregory, P. C., Xu, H.-J., Backhouse, C. J., & Reid, A. 1989, ApJ, 339, 1054

Grundstrom, E. D., & Gies, D. R. 2006, ApJ, 651, L53

Grundstrom, E. D., Boyajian, T. S., Finch, C., et al. 2007, ApJ, 660, 1398

Haigh, N. J., Coe, M. J., & Fabregat, J. 2004, MNRAS, 350, 1457

Hanuschik, R. W. 1988, A&A, 190, 187

—. 1989, Ap&SS, 161, 61

Hanuschik, R. W., Kozok, J. R., & Kaiser, D. 1988, A&A, 189, 147

Hellier, C. 2001, Cataclysmic Variable Stars

Horne, K., & Marsh, T. R. 1986, MNRAS, 218, 761

Huang, S.-S. 1972, ApJ, 171, 549

Hummel, W., & Hanuschik, R. W. 1997, in Astronomische Gesellschaft Abstract Series, Vol. 13, Astronomische Gesellschaft Abstract Series, ed. R. E. Schielicke, 192

Hummel, W., & Vrancken, M. 1995a, in Astronomical Society of the Pacific Conference Series, Vol. 81, Laboratory and Astronomical High Resolution Spectra, ed. A. J. Sauval, R. Blomme, & N. Grevesse, 544

Hummel, W., & Vrancken, M. 1995b, A&A, 302, 751

Hummel, W., & Vrancken, M. 1997, in Astronomische Gesellschaft Abstract Series, Vol. 13, Astronomische Gesellschaft Abstract Series, ed. R. E. Schielicke, 193

Hutchings, J. B., & Crampton, D. 1981, PASP, 93, 486

Janot-Pacheco, E., Ilovaisky, S. A., & Chevalier, C. 1981, A&A, 99, 274

Janot-Pacheco, E., Motch, C., & Pakull, M. W. 1988, A&A, 202, 81

Jones, T. J. 1979, ApJ, 228, 787

King, A. R. 1996, Ap&SS, 237, 169

Klein-Wolt, M., Fender, R. P., Pooley, G. G., et al. 2002, MNRAS, 331, 745

Kogure, T. 1975, PASJ, 27, 165

Lee, U., Osaki, Y., & Saio, H. 1991, MNRAS, 250, 432

Lipunov, V. M., & Nazin, S. N. 1994, A&A, 289, 822

Liu, Q. Z., & Yan, J. Z. 2005, , 11, 130

Lomb, N. R. 1976, Ap&SS, 39, 447

Makino, F., & GINGA Team. 1989, IAU Circ., 4858, 1

Makishima, K., Ohashi, T., Kawai, N., et al. 1990, PASJ, 42, 295

Maraschi, L., & Treves, A. 1981, MNRAS, 194, 1P

Marti, J., & Paredes, J. M. 1995, A&A, 298, 151

Martin, R. G., Pringle, J. E., Tout, C. A., & Lubow, S. H. 2011, in Astronomical Society of the Pacific Conference Series, Vol. 447, Evolution of Compact Binaries, ed. L. Schmidtobreick, M. R. Schreiber, & C. Tappert, 251

Massi, M. 2004, A&A, 422, 267

—. 2005, ArXiv Astrophysics e-prints

Massi, M., Ribó, M., Paredes, J. M., Peracaula, M., & Estalella, R. 2001, A&A, 376, 217

McNally, D. 1994, in Astrophysics and Space Science Library, Vol. 187, Frontiers of Space and Ground-Based Astronomy, ed. W. Wamsteker, M. S. Longair, & Y. Kondo, 165

McSwain, M. V., Grundstrom, E. D., Gies, D. R., & Ray, P. S. 2010, ApJ, 724, 379

Meier, D. L., & Koide, S. 2000, in Astrophysical Phenomena Revealed by Space VLBI, ed. H. Hirabayashi, P. G. Edwards, & D. W. Murphy, 31–38

Meier, D. L., Koide, S., & Uchida, Y. 2001, Science, 291, 84

Mennickent, R. E., Pietrzyński, G., Gieren, W., & Szewczyk, O. 2002, A&A, 393, 887

Mirabel, F. 2006, in IAU Symposium, Vol. 230, Populations of High Energy Sources in Galaxies, ed. E. J. A. Meurs & G. Fabbiano, 85–85

Mirabel, I. F., & Rodríguez, L. F. 1999, ARA&A, 37, 409

Morales-Rueda, L., Carter, D., Steele, I. A., Charles, P. A., & Worswick, S. 2004, Astronomische Nachrichten, 325, 215

Moritani, Y., Nogami, D., Okazaki, A. T., et al. 2011, PASJ, 63, L25

—. 2013, PASJ, 65, 83

Motch, C., & Janot-Pacheco, E. 1987, A&A, 182, L55

Motch, C., Pakull, M. W., Janot-Pacheco, E., & Mouchet, M. 1988, A&A, 201, 63

Nagase, F., Dotani, T., Tanaka, Y., et al. 1991, ApJ, 375, L49

Naik, S., Maitra, C., Jaisawal, G. K., & Paul, B. 2013, ApJ, 764, 158

Negueruela, I., Okazaki, A. T., Fabregat, J., et al. 2001, A&A, 369, 117

Negueruela, I., Reig, P., Coe, M. J., & Fabregat, J. 1998, A&A, 336, 251

Negueruela, I., Roche, P., Fabregat, J., & Coe, M. J. 1999, MNRAS, 307, 695

Negueruela, I., Grove, J. E., Coe, M. J., et al. 1997, MNRAS, 284, 859

Neronov, A., & Chernyakova, M. 2007, ArXiv Astrophysics e-prints

Neto, A. D., & de Freitas-Pacheco, J. A. 1982, MNRAS, 198, 659

O'Donoghue, D., Buckley, D. A. H., Balona, L. A., et al. 2006, MNRAS, 372, 151

Okazaki, A. T. 1991, PASJ, 43, 75

Okazaki, A. T., Hayasaki, K., & Moritani, Y. 2013, PASJ, 65, 41

Okazaki, A. T., & Negueruela, I. 2001, A&A, 377, 161

Orellana, M., & Romero, G. E. 2007, Ap&SS, 309, 333

Owocki, S., & Ud-Doula, A. 2003, in Astronomical Society of the Pacific Conference Series, Vol. 305, Magnetic Fields in O, B and A Stars: Origin and Connection to Pulsation, Rotation and Mass Loss, ed. L. A. Balona, H. F. Henrichs, & R. Medupe, 350

Owocki, S. P., Cranmer, S. R., & Gayley, K. G. 1996, ApJ, 472, L115

Papaloizou, J. C., Savonije, G. J., & Henrichs, H. F. 1992, A&A, 265, L45

Paredes, J. M., Estalella, R., & Rius, A. 1990, Ap&SS, 169, 203

Paredes, J. M., Marti, J., Peracaula, M., & Ribo, M. 1997, A&A, 320, L25

Paredes, J. M., Marziani, P., Marti, J., et al. 1994, A&A, 288, 519

Parmar, A. N., White, N. E., & Stella, L. 1989, ApJ, 338, 373

Paul, B., & Naik, S. 2011, Bulletin of the Astronomical Society of India, 39, 429

Pedani, M. 2004, , 9, 641

Porter, J. M. 1996, MNRAS, 280, L31

—. 1997, A&A, 324, 597

—. 1998, A&A, 336, 966

Porter, J. M., & Rivinius, T. 2003, PASP, 115, 1153

Press, W. H., & Rybicki, G. B. 1989, ApJ, 338, 277

Punsly, B. 1999, ApJ, 519, 336

Punsly, B., & Coroniti, F. V. 1990, ApJ, 350, 518

Quirrenbach, A., Bjorkman, K. S., Bjorkman, J. E., et al. 1997, ApJ, 479, 477

Rajoelimanana, A. F., Charles, P. A., & Udalski, A. 2011, MNRAS, 413, 1600

Reig, P. 2011, Ap&SS, 332, 1

Reig, P., Fabregat, J., & Coe, M. J. 1997, A&A, 322, 193

Reig, P., Larionov, V., Negueruela, I., Arkharov, A. A., & Kudryavtseva, N. A. 2007, A&A, 462, 1081

Reig, P., Negueruela, I., Coe, M. J., et al. 2000, MNRAS, 317, 205

Reig, P., & Roche, P. 1999, MNRAS, 306, 100

Reig, P., Stevens, J. B., Coe, M. J., & Fabregat, J. 1998, MNRAS, 301, 42

Romero, G. E., Christiansen, H. R., & Orellana, M. 2005, ApJ, 632, 1093

Romero-Colmenero, E., Buckley, D., Kniazev, A., et al. 2007, in Astronomical Society of the Pacific Conference Series, Vol. 373, The Central Engine of Active Galactic Nuclei, ed. L. C. Ho & J.-W. Wang, 717

Rosenberg, F. D., Eyles, C. J., Skinner, G. K., & Willmore, A. P. 1975, Nature, 256, 628

Rothschild, R., Markowitz, A., Hemphill, P., et al. 2013, ApJ, 770, 19

Sadowski, A., Ziółkowski, J., Belczyński, K., & Bulik, T. 2008, in IAU Symposium, Vol. 252, IAU Symposium, ed. L. Deng & K. L. Chan, 399–403

Savonije, G. J., & Heemskerk, M. H. M. 1993, A&A, 276, 409

Sazonov, S., & Sunyaev, R. 1995, IAU Circ., 6272, 2

Scargle, J. D. 1982, ApJ, 263, 835

Shakura, N. I., & Sunyaev, R. A. 1973, in IAU Symposium, Vol. 55, X- and Gamma-Ray Astronomy, ed. H. Bradt & R. Giacconi, 155

Silaj, J., Jones, C. E., Tycner, C., Sigut, T. A. A., & Smith, A. D. 2010, ApJS, 187, 228

Slettebak, A. 1982, ApJS, 50, 55

Staubert, R., Pottschmidt, K., Doroshenko, V., et al. 2011, A&A, 527, A7

Steele, I. A. 2001, Astronomische Nachrichten, 322, 307

—. 2004, Astronomische Nachrichten, 325, 519

Steele, I. A., Negueruela, I., Coe, M. J., & Roche, P. 1998, MNRAS, 297, L5

Stella, L., White, N. E., & Rosner, R. 1986, ApJ, 308, 669

Stobie, R., Meiring, J., & Buckley, D. A. 2000, in Society of Photo-Optical Instrumentation Engineers (SPIE) Conference Series, Vol. 4003, Society of Photo-Optical Instrumentation Engineers (SPIE) Conference Series, ed. P. Dierickx, 355–362

Takahashi, M., Nitta, S., Tatematsu, Y., & Tomimatsu, A. 1990, ApJ, 363, 206

Tamura, K., Tsunemi, H., Kitamoto, S., Hayashida, K., & Nagase, F. 1992, ApJ, 389, 676

Tavani, M., & Arons, J. 1997, ApJ, 477, 439

Tavani, M., Arons, J., & Kaspi, V. M. 1994, ApJ, 433, L37

Taylor, A. R., & Gregory, P. C. 1982, ApJ, 255, 210

Taylor, A. R., Kenny, H. T., Spencer, R. E., & Tzioumis, A. 1992, ApJ, 395, 268

Telting, J. H., Heemskerk, M. H. M., Henrichs, H. F., & Savonije, G. J. 1994, A&A, 288, 558

Terrell, J., & Priedhorsky, W. C. 1984, ApJ, 285, L15

Townsend, L. J., Coe, M. J., Corbet, R. H. D., & Hill, A. B. 2011, MNRAS, 416, 1556

Townsend, R. H. D., Owocki, S. P., & Howarth, I. D. 2004, MNRAS, 350, 189

Tycner, C., Lester, J. B., Hajian, A. R., et al. 2005, ApJ, 624, 359

van Dokkum, P. G. 2001, PASP, 113, 1420

Waters, L. B. F. M., & van Kerkwijk, M. H. 1989, A&A, 223, 196

Whitlock, L., Roussel-Dupre, D., & Priedhorsky, W. 1989, ApJ, 338, 381

Wilson, C. A., Fabregat, J., & Coburn, W. 2005, ApJ, 620, L99

Woolf, N. J., Stein, W. A., & Strittmatter, P. A. 1970, A&A, 9, 252

Wright, G. 2005, The Observatory, 125, 338

Yudin, R. V. 2001, A&A, 368, 912

Zamanov, R., Paredes, J. M., Martí, J., & Markova, N. 1996, Ap&SS, 243, 269

Zamanov, R., Stoyanov, K., Marti, J., et al. 2013, ArXiv e-prints

Zamanov, R. K., Martí, J., Paredes, J. M., et al. 1999, A&A, 351, 543

Zhang, S., Qu, J.-L., Song, L.-M., & Torres, D. F. 2005, ApJ, 630, L65